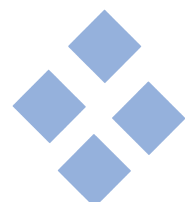


Yulong Gao

**Investigation on the Dynamic Behavior
of Paintings During Transport:
Experimentation, Simulation
and Modeling**



**SHAKER
VERLAG**

Band 86 (2024)

Investigation on the Dynamic Behavior of Paintings During Transport: Experimentation, Simulation and Modeling

Von der Fakultät Konstruktions-, Produktions- und Fahrzeugtechnik
der Universität Stuttgart
zur Erlangung der Würde eines Doktor-Ingenieurs (Dr.-Ing.)
genehmigte Abhandlung

Vorgelegt von
Yulong Gao
aus Hefei, V.R. China

Hauptberichter: Prof. Dr.-Ing. Prof. E.h. Peter Eberhard
Mitberichter: Prof. Dr.-Ing. habil. Kai Willner

Tag der mündlichen Prüfung: 18. September 2024

Institut für Technische und Numerische Mechanik
der Universität Stuttgart

2024

Schriften aus dem Institut für Technische und Numerische
Mechanik der Universität Stuttgart

Herausgeber: Prof. Dr.-Ing. Prof. E.h. Peter Eberhard

Band 86/2024

Yulong Gao

**Investigation on the Dynamic Behavior
of Paintings During Transport:
Experimentation, Simulation and Modeling**

D 93 (Diss. Universität Stuttgart)

Shaker Verlag
Düren 2024

Bibliographic information published by the Deutsche Nationalbibliothek

The Deutsche Nationalbibliothek lists this publication in the Deutsche Nationalbibliografie; detailed bibliographic data are available in the Internet at <http://dnb.d-nb.de>.

Zugl.: Stuttgart, Univ., Diss., 2024

Copyright Shaker Verlag 2024

All rights reserved. No part of this publication may be reproduced, stored in a retrieval system, or transmitted, in any form or by any means, electronic, mechanical, photocopying, recording or otherwise, without the prior permission of the publishers.

Printed in Germany.

ISBN 978-3-8440-9683-5

ISSN 1861-1651

Shaker Verlag GmbH • Am Langen Graben 15a • 52353 Düren

Phone: 0049/2421/99011-0 • Telefax: 0049/2421/99011-9

Internet: www.shaker.de • e-mail: info@shaker.de

Preface

This dissertation marks the culmination of five transformative years spent as a dedicated researcher at the Institute of Engineering and Computational Mechanics (ITM) at the University of Stuttgart. During this time, I have had the profound honor of immersing myself in the study of the dynamic characteristics of paintings, an endeavor that has not only expanded my intellectual horizons but also enriched my life in countless ways.

Reflecting on these years, I am filled with deep gratitude for the incredible atmosphere at ITM. The collaborative spirit and the serene environment here have allowed me to grow, not just as a researcher, but as a person. My journey has been one of continuous learning, marked by moments of profound insight and personal growth. To everyone who has crossed my path during this period, offering wisdom and support, I extend my heartfelt thanks.

First and foremost, I am deeply indebted to my doctoral advisor, Prof. Peter Eberhard. From our very first conversation, I felt a sense of destiny guiding me to Germany and to his esteemed tutelage. His unwavering support, insightful guidance, and boundless patience have been the bedrock of my research. Prof. Eberhard, your encouragement and understanding, especially during times of error and doubt, have been invaluable. Your trust in granting me the freedom to explore has allowed me to flourish as a researcher. I am profoundly grateful for the opportunity to be a part of your research group and for the myriad ways you have influenced my scientific and personal journey.

I would also like to extend my sincere gratitude to Prof. Jörg Fehr, whose enthusiasm and guidance have been instrumental in steering my research in fruitful directions. Prof. Michael Hanss, thank you for the enriching discussions about cultural nuances and the dynamic exchange of ideas that broadened my perspective on art and research. Your efforts in publicizing our work on social media have added a vibrant dimension to our academic endeavors.

Special thanks are due to my secondary supervisor, Dr.-Ing. Pascal Ziegler. Our numerous discussions, both rigorous and enjoyable, have been a cornerstone of my academic development. Your expertise and enthusiasm have been crucial in overcoming research challenges, and your friendship has made the journey all the more rewarding. I am deeply appreciative of your support and the exciting moments we shared in the lab.

I would also like to express my heartfelt thanks to Peter Schöler, whose generosity and technical prowess with lab equipment have been indispensable. Peter, your meticulous modifications and insightful suggestions made the experimental aspects of this dissertation possible. To my colleague, Eva Hartlieb, thank you for sharing your extensive knowledge of art. Your contributions have enriched my understanding and appreciation of the artistic

IV

aspects of our research.

To my colleagues and friends at ITM, thank you for creating a nurturing and inclusive environment. Your advice and camaraderie have been sources of inspiration and joy, making this journey a collective achievement. I am also grateful to the students I have supervised over the years. Our interactions have sparked many eureka moments and deepened my own understanding of our work. To Prof. Peter and my co-examiners, I appreciate your commitment and thoroughness in reviewing my research, which has elevated the quality of this dissertation.

My deepest thanks go to my family in China. Your unwavering support and understanding have been my anchor throughout this journey. Without your encouragement, this work would not have been possible.

Lastly, I want to acknowledge myself. Navigating five years in a foreign land, amidst challenges and uncertainties, has been a testament to my resilience and inner strength. Despite the occasional cloudy skies, I have emerged more emotionally grounded and determined. As I look ahead to the unknown, I am confident in my ability to face future challenges with the same resolve and inner fortitude.

Stuttgart, July 2024

Yulong Gao

Contents

| | |
|---|-----------|
| Zusammenfassung | IX |
| Abstract | XI |
| 1 Introduction | 1 |
| 2 Investigated Paintings | 7 |
| 2.1 Dummy Paintings | 7 |
| 2.1.1 Unprimed Dummy Paintings | 7 |
| 2.1.2 Primed Dummy Paintings | 10 |
| 2.1.3 A Painted Dummy Painting | 10 |
| 2.2 Real Paintings | 12 |
| 2.3 Orientation of Paintings | 13 |
| 3 Modal Characteristics of Paintings | 15 |
| 3.1 Theoretical Background of Experimental Modal Analysis | 17 |
| 3.1.1 Frequency Response Function | 17 |
| 3.1.2 Modal Parameter Identification Based on SVD | 20 |
| 3.2 Simplified Mechanical Model of Paintings | 22 |
| 3.2.1 Mathematical Model | 23 |
| 3.2.2 Finite Element Model | 25 |
| 3.3 Experimental and Numerical Analysis of Paintings | 28 |
| 3.3.1 Experimental Setup | 28 |
| 3.3.2 Modal Parameter Identification | 31 |
| 3.4 Climate Influence on Paintings | 43 |
| 3.4.1 Experimental Setup and Measurements | 44 |

| | | |
|----------|---|------------|
| 3.4.2 | Linearization and Eigenfrequency Compensation | 49 |
| 4 | Simulation of Transport-induced Vibration | 53 |
| 4.1 | Theoretical Background of LMS Algorithm | 55 |
| 4.1.1 | Least Mean Square Algorithm | 56 |
| 4.1.2 | Single Channel Filtered- x LMS Algorithm | 59 |
| 4.2 | A Real Transport Experiment | 62 |
| 4.2.1 | Experimental Procedure | 62 |
| 4.2.2 | Simplified Vibration of a Painting During Transport | 64 |
| 4.3 | Reproduction of Transport-induced Vibration | 65 |
| 4.3.1 | Experimental Setup | 65 |
| 4.3.2 | Multi-Channel Vibration Tracking Controller | 67 |
| 4.3.3 | Vibration Reproduction on the Strainer | 72 |
| 4.3.4 | Vibration Reproduction on the Canvas | 80 |
| 4.4 | Reconstruction of Transport-induced Vibration | 85 |
| 4.4.1 | Numerical Model | 86 |
| 4.4.2 | Methodology for Numerical Modeling | 89 |
| 4.4.3 | Experimental Setup and Measurements | 93 |
| 4.4.4 | Numerical Analysis and Model Optimization | 95 |
| 4.4.5 | Vibration Reconstruction Results | 101 |
| 5 | Nonlinear Dynamic Behavior of Paintings | 105 |
| 5.1 | Experimental Setup and Measurements | 107 |
| 5.2 | Identification of Nonlinear Dynamic Behavior | 111 |
| 5.2.1 | Hammer Experiment with Excitation on the Strainer | 112 |
| 5.2.2 | Sweep Experiment with Excitation on the Strainer | 113 |
| 5.2.3 | Hammer Experiment with Excitation on the Canvas | 116 |
| 5.2.4 | Nonlinear Output Frequency Response Functions | 118 |
| 5.3 | Modal Nonlinearities During Vibration | 121 |
| 5.3.1 | Analysis of Nonlinear Characteristics | 122 |
| 5.3.2 | Discussion on the Consequences for Transport | 124 |

| | |
|--|------------|
| 5.4 Nonlinear Behavior Identification Methods | 129 |
| 5.4.1 Sweep Experiment with Loudspeaker | 129 |
| 5.4.2 Evaluation of Different Identification Methods | 130 |
| 6 Conclusion and Outlook | 133 |
| Appendix | 137 |
| A.1 Experimental Modal Analysis on Unprimed Dummy Painting B | 137 |
| A.2 Experimental Modal Analysis on Unprimed Dummy Painting C | 139 |
| A.3 Experimental Modal Analysis on Primed Dummy Painting B | 142 |
| A.4 Experimental Modal Analysis on Primed Dummy Painting C | 144 |
| A.5 Experimental Modal Analysis on Paining Landscape | 147 |
| Abbreviations, Symbols, and Notation | 149 |
| Bibliography | 151 |

Zusammenfassung

Da der Kunstverleih zwischen Museum häufiger wird, sind Kunstreparatoren zunehmend besorgt über das Schwingungsverhalten von Gemälden während des Transports. Die Anregung der Eigenmoden der Gemälde kann zu großen Verschiebungen auf der Leinwand führen, was potenziell irreversible Schäden an ihrer komplexen Materialität verursacht und die natürliche Alterung des Werks beschleunigt. Allerdings basieren die meisten derzeitigen Entscheidungen und Vorsichtsmaßnahmen zur Minderung der Schwingungseffekte oder zur Bestimmung tolerierbarer Schwingungsniveaus auf begrenztem Wissen über die dynamischen Eigenschaften von Gemälden. Darüber hinaus erschwert die Unfähigkeit, die Schwingungsreaktionen während des Transports zu überwachen, die Forschung.

Moderne Ingenieurmethoden, einschließlich Modaltests, Echtzeitsimulationen und numerische Modellierung, könnten Kunstreparatoren systematischere Ansätze bieten, um die oben genannten Herausforderungen zu bewältigen. Diese Arbeit, die sich auf das Verhalten von Gemälden während des Transports konzentriert, präsentiert deren allgemeine dynamische Eigenschaften und Methoden zur Simulation transportinduzierter Schwingungen, die helfen können, das Schwingungsverhalten von Gemälden während des Transports zu verstehen und den Restauratoren zu ermöglichen, die Transportbedingungen zu verbessern.

Die Forschung beginnt mit einer experimentellen Modal-Analyse von sorgfältig gefertigten und ausgewählten Dummy-Gemälden und echten Gemälden. Durch das Extrahieren und Vergleichen der Modalparameter fasst die Studie die allgemeinen dynamischen Eigenschaften von Gemälden mithilfe vereinfachter mechanischer Modelle und Finite-Elemente-Methoden zusammen. Darüber hinaus untersucht sie den Einfluss des Klimas auf die Modaleigenschaften und schlägt eine lineare Anpassung der Eigenfrequenz von Gemälden basierend auf Veränderungen der Temperatur und Luftfeuchtigkeit vor, um klimabedingte Variationen auszugleichen.

Ein großer Teil in dieser Arbeit widmet sich der Simulation der transportinduzierten Schwingungen, die in Echtzeit während des Transports nicht praktikabel zu messen sind. Zwei Ansätze werden vorgeschlagen, wobei ein reales Transportexperiment als Originalreferenz dient. Der erste Ansatz beinhaltet die Wiedergabe der während des Transports gemessenen Schwingungen am Keilrahmen des Gemäldes und reproduziert somit die transportinduzierten Schwingungen auf der Leinwand. Eine Schwingungsreproduktions-Simulationsplattform, die einen mehrkanaligen aktiven Schwingungsregelungsalgorithmus implementiert, wird entwickelt, um dies zu erreichen. Diese Methode demonstriert ihre Wirksamkeit, indem die Reproduktionsergebnisse eng mit der Originalreferenz übereinstimmen und eine stabile Reproduzierbarkeit gewährleistet wird.

Der zweite Ansatz etabliert ein numerisches Modell, das die Schwingungen am Keilrahmen des Gemäldes mit den Schwingungen an einem beliebigen Punkt auf der Leinwand

verknüpft. Ein optimales numerisches Modell, basierend auf Modaltests, wird entwickelt, um transportinduzierte Schwingungen auf der Leinwand zu rekonstruieren, was eine starke Übereinstimmung mit den reproduzierten Ergebnissen zeigt. Diese beiden Simulationsmethoden liefern zuverlässige Referenzen für unbekannte Leinwandreaktionen während des Transports und erleichtern fortschrittliche Forschungen für Kunstreparatoren.

Der letzte Beitrag dieser Arbeit untersucht das nichtlineare dynamische Verhalten von Gemälden. Mechanische Lasten unterschiedlicher Intensitäten werden auf Dummy-Gemälde und echte Gemälde angewendet, um die lineare Hypothese während des Transports zu testen. Die experimentellen Ergebnisse stellen die weit verbreitete Auffassung in Frage, dass Gemälde während des Transports als lineare Systeme modelliert werden können, und zeigen, dass sie ein nichtlineares Verhalten aufweisen. Die nichtlinearen dynamischen Eigenschaften von Gemälden und ihre möglichen Folgen für den Transport werden diskutiert. Darüber hinaus werden verschiedene Testmethoden analysiert, um Kunstreparatoren methodische Anleitungen zur Identifizierung des nichtlinearen dynamischen Verhaltens von Gemälden zu bieten.

Abstract

As inter-museum loans of artworks become more frequent, art conservators are increasingly concerned about the vibration behavior of paintings in their care during transport. The excitation of the paintings' eigenmodes can lead to large displacements on the canvas, which potentially causes irreversible damage to their complex material composition and accelerates their natural aging process. However, most current decisions and precautions to mitigate vibration effects or determine tolerable vibration levels are based on limited knowledge of the dynamic characteristics of paintings. Furthermore, the inability to monitor vibration responses during transport hampers advanced research.

However, state-of-the-art engineering methods, including modal testing, real-time simulation, and numerical modeling, might provide art conservators some more systematic approaches to overcome the challenges mentioned above. This thesis, focusing on the painting during transport, presents their general dynamic characteristics and transport-induced vibration simulation methods, which can help to understand the vibration behavior of paintings during transport and help art conservators to improve transport conditions.

The research begins with an experimental modal analysis of carefully crafted and selected dummy paintings and real paintings. By extracting and comparing modal parameters, the study summarizes the general dynamic characteristics of paintings with the aid of a simplified mechanical model and finite element methods. Additionally, it investigates the influence of climate on modal characteristics, proposing a linear fit between the eigenfrequency of paintings and changes in temperature and humidity to compensate for the climate-induced variations.

A large part of the thesis is then devoted to simulating the transport-induced vibration, which is impractical to measure in real-time during transport. Two approaches are proposed, using a real transport experiment as an original reference. The first approach involves replaying the vibration on the painting strainer (colloquially called the 'frame') measured during transport, and thereby reproducing the transport-induced vibration on the canvas. A vibration reproduction simulation platform, implementing a multi-channel active vibration control algorithm, is developed to achieve this. This method demonstrates its efficacy by closely matching the reproduction results with the original reference, ensuring a stable reproducibility.

The second approach establishes a numerical model linking the vibration on the painting strainer to the vibration at an arbitrary point on the canvas. An optimal numerical model based on modal testing is developed to reconstruct transport-induced vibrations on the canvas, showing strong agreement with the reproduced results. These two simulation methods provide reliable references for unknown canvas responses during transport, facilitating advanced research for art conservators.

The final contribution of this thesis investigates the nonlinear dynamic behavior of paintings. Mechanical loads of varying intensities are applied to both dummy paintings and real paintings to test the linear hypothesis during transport. The experimental results challenge the inherent perception that paintings can be modeled as linear systems during transport, revealing that they are likely to exhibit nonlinear behavior. The nonlinear dynamic characteristics of paintings and their possible consequences for transport are discussed, and different test methods are analyzed to provide art conservators with guidance for identifying the nonlinear dynamic behavior in paintings.

Chapter 1

Introduction

Art serves as a universal language, allowing people to share each other's stories and emotions across cultural and linguistic barriers. Among the various forms of art, paintings hold a foundational and pivotal role, constantly promoting the evolution and transformation of artistic landscape. In contemporary times, paintings have even become a highly influential medium for social criticism, garnering widespread interest and traveling across the globe. However, the increasing frequency of interlibrary loans and traveling exhibitions has raised concerns among art conservators. They have been aware that the transport of paintings can lead to irreversible changes in their complex material composition, thus accelerating their natural aging process [HeinKrekel10, KrekelHein14, BäschlinEtAl15, KrekelHeinemann20]. Consequently, conservators have been striving to develop more appropriate procedures to minimize the risks and hazards involved in the transport. Environmental factors such as temperature, humidity, light, dust, and vibration are all possible contributors for potential damage during handling, packing or shipping a painting [MecklenburgTumosa91b, YoungAckroyd01, GiakoumisNikolaidisPitas05, PinnaGaleottiMazzeo09, Michalski13, WaentigEtAl15]. Of particular concern is the impact of vibration, which can deform the canvas, induce stress in the paint layers, and potentially cause cracking, or even paint loss from canvas. Unfortunately, it seems like the secrets between transport-induced vibration and potential damage to paintings are often concealed by technical complexities. This thesis aims to bridge the gap between understanding these vibrations and mitigating their detrimental effects on paintings during transport, aligning with the ongoing efforts of art conservators.

As early as the 1990s, the seminal work "Art in Transit" was published [Mecklenburg91], extensively discussing the dangers to which artworks may be exposed during transport. This work first suggested that, like any dynamic system, the motion in eigenfrequencies of paintings can generate large displacements and would be the potentially harmful for them. This highlighted the need to understand the dynamic characteristics of paintings in order to develop effective protective measures. Since then, substantial

research has been devoted to measuring and monitoring vibration affecting paintings during transport [Saunders98, Saunders05, Palmbach07, KambaEtAl08, LäuchliEtAl14, Sautter14, HeinemannEtAl19]. Some studies have also examined the effects of mechanical loads on test paintings [TsiranidouEtAl13, TornariTsiranidouBernikola14], although the holographic techniques used to observe changes are complex and not easily interpreted by the average person. These studies consistently recognize that while shock excitation may cause immediate damage to the art works, vibration excitation results in long-term and cumulative damage which is not always immediately apparent. An important conclusion reached is that once the eigenmodes of a painting are excited, the vibration intensity of the canvas can be significantly higher than that transferred to the painting strainer through the crate. Thus, it is increasingly important to investigate the dynamic characteristics of paintings and to improve transport conditions accordingly. The vibration behavior of paintings on textile supports was investigated in [Kracht11], explicitly as a function of aging, and two-dimensional images were used to visualize surface changes. Additionally, a finite element (FE) model was developed in [ChiribogaArroyo13] for characterizing the vibration of canvas paintings, aiming to predict their behavior under vibration loading and to obtain a fundamental understanding of the relevant parameters. These investigation have significantly contributed to the basic understanding of the dynamic behaviors of paintings, providing crucial insights into why and how these behaviors occur.

Despite the significant advances made, a key issue remains, i.e., the lack of systematic research on the dynamic characteristics of paintings. Consequently, many decisions and precautions taken to mitigate the effects of vibration or to determine tolerable levels of vibration are still based on an inadequate understanding of these characteristics. On the other hand, most previous studies have measured vibrations on everything except the painting itself. Vibration data collected from the painting strainer or packing case provide little insight into the actual behavior of the canvas. While technical constraints play a role, the insufficient understanding of the canvas's actual vibration behavior and its relationship to the damage produced in paintings has also limited advanced research. Studies on the damage mechanisms of paintings subjected to vibration, performance evaluation of packing cases, and their optimal design, etc. are still underdeveloped. This thesis aims to open the door to this advanced research by systematically investigating the dynamic characteristics of paintings and the actual vibration behavior of canvas during transport.

Transport of a Painting

This thesis is mainly concerned with the transport of paintings, and therefore, a brief description of the process is relevant. The transport of paintings to and from exhibitions typically involves three main procedures: packing, handling, and transport. This thesis specifically addresses the vibration experienced by paintings inside transport crates. Figure 1.1 depicts a typical transport process of a painting, incorporating vibration moni-

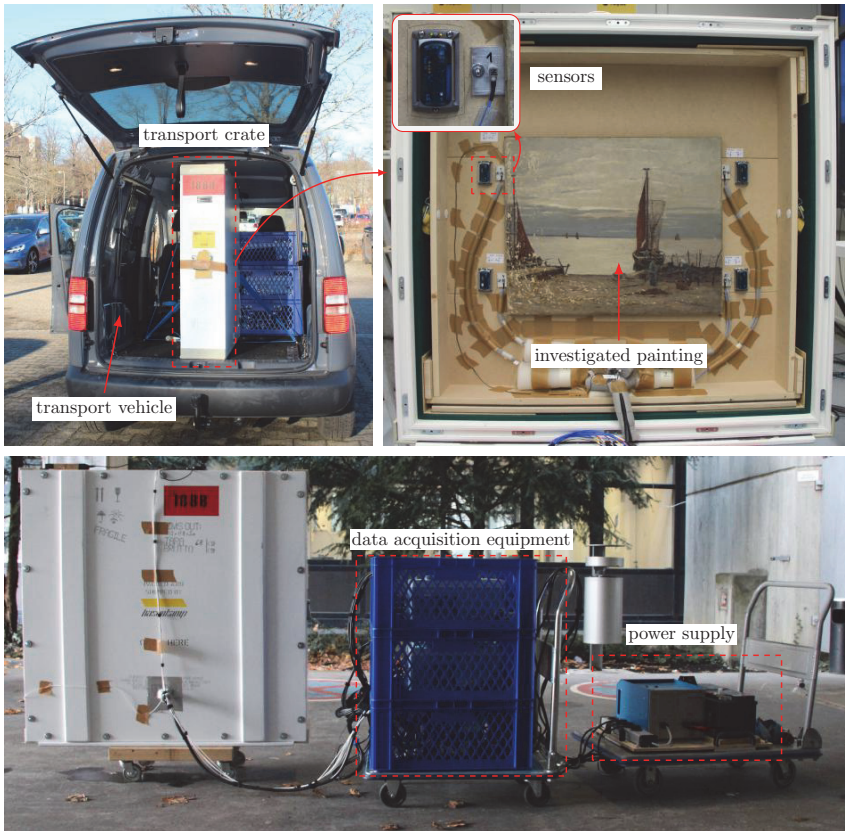


Figure 1.1: A typical handling and transport configuration of the painting with vibration monitoring on the packing case and the painting strainer.

toring on the transport crate and the painting strainer, which has been studied in depth in [HeinemannEtAl19]. The process uses a basic multi-layer climate transport crate without special vibration isolation measures. The investigated painting are carefully packaged and secured inside the interior crate by some hanging systems, without a protective backing. Once packed, the crate and painting are handled and transported by vehicle (car, ship, airplane, etc.) to the destination.

In order to monitor the vibration experienced by the painting or the transport crate from the start of handling until the destination, sensors are typically installed. Monitoring the transport crate is convenient, with sensors possible either insider or outside. However,

attaching sensors directly to the surface of a painting is prohibited from a conservatory perspective, especially for valuable artworks, and also because it could increase the local mass of the canvas and alter its dynamic behavior. While non-contact vibrometers could measure vibrations directly on the canvas, mounting these is challenging. The usual solution is to mount the sensor on the hanging systems connected to the painting, as shown in Fig. 1.1. Even then, the monitoring process is quite cumbersome, requiring significant preparation time and equipment.

This representative example provides a general impression of the painting transport process. Packing, handling, and transport procedures may vary depending on the size and construction of the painting. Moreover, there are also transport crates available that offer improved performance and vibration isolation. However, regardless of the transport method, vibration remains an inevitable issue. Conclusions drawn from studying a representative example are thus of great interest.

Aims and Contents of the Thesis

Due to the limitations of measurement techniques, it is impractical to investigate the dynamic characteristics of paintings during transport. Transferring the painting to a laboratory, where it can be tested with a known excitation in a more closely-controlled environment, is more convenient and yields more accurate and detailed information. This type of testing, which includes both the data acquisition and subsequent analysis, is known as 'modal testing' with the objective to obtain a mathematical description of the structure's dynamic behavior. Although the modal parameters obtained in the laboratory may differ from those during actual transport, this scientific quantification facilitates comparisons and the drawing of general conclusions. Furthermore, instead of being restricted to monitoring the vibration of paintings during transport, somehow simulating the transport-induced vibration in a controlled environment offers a new approach to understanding the relationship between the vibration of paintings and their potential damage. Therefore, two aims of this thesis can be formulated.

- The dynamic characteristics of paintings shall be investigated, which help to understand their vibration behavior during transport, especially the influence of modal parameters on the vibration behavior and factors that affect the modal parameters.
- This research shall simulate the transport-induced vibration of paintings in the laboratory, providing art conservators a visual and reliable reference for the unknown canvas vibration response during transport.

The author aspires to help art conservators better understand the dynamic characteristics of the painting, a complex object, to further improve transport conditions and protect

valuable art assets. Additionally, addressing the challenges of monitoring transport-induced vibration enables art conservators to conduct advanced research which cannot be done during a real transport. Consequently, the experimental, simulation, and numerical investigations in this thesis always go hand in hand and are discussed together in the relevant chapters. Although this thesis focuses on a limited number of paintings, the conclusions drawn can be generalized to other comparable structures and sizes of paintings. Moreover, the proposed methods for simulating transport-induced vibration are broadly applicable with appropriate adaptations. The thesis is composed of the following chapters.

Chapter 2 assembles the paintings investigated in this thesis, including four dummy paintings and three real paintings. Each dummy painting was carefully crafted by experienced conservators. Their production process and differences are described in detail. Although the real paintings do not possess high artistic value, they have naturally aged over a long period and suffered significant damage. All available information about the real paintings is provided. Following this, to facilitate the description of the painting's motion during transport throughout the text, a spatial coordinate system is established to define the painting's orientation, which is also standardized with the transport vehicle.

Chapter 3 presents a comprehensive investigation into the linear dynamic characteristics of both dummy paintings and real paintings. It begins with a short overview of the current state of research on the dynamic characteristics of paintings. Then, the mathematics behind experimental modal analysis and the specific methods used in the corresponding experiments are briefly introduced. A vibrating rectangular membrane is examined as a simplified mechanical model for paintings. The finite element method (FEM) is employed to study the influence of inhomogeneities on the eigenmodes of paintings. Following this, a detailed experimental modal analysis is conducted on both, dummy paintings and real paintings, with modal parameters such as eigenfrequencies, damping ratios, and mode shapes extracted to compare their dynamic characteristics. Afterwards, the influence of climate on modal characteristics is explored, and a linear fit for the relationship between eigenfrequency, temperature, and humidity is proposed to compensate for climate-induced changes. The results of Chapter 3 provide a general understanding of the dynamic characteristics of paintings, serving as a reference for their vibration behavior during transport.

The following Chapter 4 is devoted to addressing the challenges of monitoring the vibration of paintings during transport. After a brief overview of existing monitoring approaches, the basics of the least mean square (LMS) algorithm for active vibration control are introduced. A real painting transport experiment is first conducted to provide a baseline reference. Two simulation methods are proposed for monitoring the transport-induced vibration of paintings. The first method involves replaying the vibration on the painting strainer collected during transport, thereby reproducing the transport-induced vibration on the canvas. For this purpose, a vibration reproduction simulation platform is developed, and a

multi-channel active vibration control algorithm is designed for this platform. Experimental results indicate that the reproduced vibration on both the painting strainer and canvas agree well with those from the real transport. The rainflow counting algorithm is applied to further process the reproduction results on the canvas. Another method develops a numerical model to describe the relationship between the vibration of the painting strainer and the vibration at an arbitrary point on the canvas, enabling reconstruction of transport-induced vibrations on the canvas. A methodology for obtaining the optimal numerical model based on modal testing is presented, and the numerical model's validity is experimentally demonstrated with the overall reconstruction results on the canvas matching the reproduction results. Eventually, these two methods provide a reliable reference for the transport-induced vibrations on the canvas.

Chapter 5 further explores the nonlinear dynamic characteristics of paintings. To validate the linear hypothesis during transport, two real paintings and one dummy painting are investigated. Mechanical loads such as shock excitation, sweep excitation, and narrowband noise are used to simulate the vibration during transport, and are applied to each painting at varying intensities. The vibration responses of paintings under these mechanical loads are compared with responses during a real transport to determine whether the paintings can be regarded as a linear system during transport. Then, the nonlinear dynamic characteristics of paintings are summarized along with their possible consequences to transport. In the end, test methods for identifying the nonlinear dynamic behavior in paintings are discussed.

The thesis closes with a conclusion of all the findings and contributions and an outlook on future research directions in Chapter 6.

Chapter 2

Investigated Paintings

The dynamic behavior of paintings and their transport related experiments presented in this thesis are carried out on various paintings. The investigated paintings are divided into two categories, dummy paintings as well as real paintings. The dummy paintings include paintings with various states of unprimed, primed, and painted layers. They have been carefully carried out by experienced conservators, resulting in a high degree of precision. The considered real paintings have become fragile and massively damaged after natural aging and are of negligible artistic value. For referencing the investigated paintings in different parts of this thesis, they are briefly presented here together with all relevant data.

2.1 Dummy Paintings

Paintings have a complex heterogeneous material structure. In simple terms, a painting consists basically of a canvas support, primer layers, and the paint layers that form the image, as shown schematically in Fig. 2.1. All materials are diverse depending on the artist's period, style and the techniques employed. Moreover, their properties can change significantly with age. Therefore, directly analyzing the dynamic characteristics of real paintings has to face the challenge of a large number of unknown and difficult to identify factors. The dummy paintings created by experienced conservators provide simplified prototypes of real paintings. Understanding the dynamic characteristics of paintings will be facilitated by continuously adding material layers to the dummy paintings and progressively analyzing the changes in their dynamic behavior.

2.1.1 Unprimed Dummy Paintings

In order to prepare the dummy painting, the first step is to pre-treat the canvas. The linen canvas with plain weaves, which is widely used by artists, was chosen to create the

dummy painting. It was cut into manageable sizes, soaked in a warm water bath (about 15°C - 20°C) for three hours, kneaded repeatedly and then washed in water in a washing machine to remove foreign matter. After air-drying, the canvas was also decatized by wetting, drying, stretching and tensioning several times to reduce the sensitivity of the fabric to moisture fluctuations, stabilize the dimensions and mechanical properties, and reduce the relaxation of the canvas after stretching [Hartlieb21].

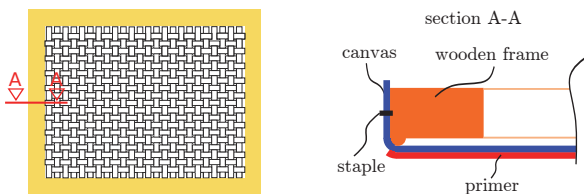


Figure 2.1: The simplified structure of a typical painting.

The pre-treated canvas was then stretched across a wooden strainer, colloquially called the 'frame', which measures 50 cm × 60 cm × 6.5 cm. This process utilized the traditional methods. The canvas was first laid on a stretcher with the threads of the canvas parallel to the strainer. One side of the canvas was tacked to the middle part of one of the stretchers. The opposite side was stretched and tacked again with canvas pliers. The canvas pliers have flat grips that will not tear the thread. Repeat the same process for the other pair of sides working out from the center toward the corners. Then, fold and tack the corners to the strainer. Finally, in order to further stretch or tighten the slack canvas, eight wedges were driven into the corners of the strainer [Lamb54]. The finished unprimed dummy painting was produced as shown in Fig. 2.2. An array consisting of reflective stickers affixed to the back of the dummy painting to facilitate vibration measurements of the canvas using a Laser Doppler Vibrometer. Reflective stickers cannot be applied to the front of the dummy painting as it will be primed later.



Figure 2.2: The front (left) and back (right) of the finished unprimed dummy painting.

A total of three unprimed dummy paintings were produced for this thesis. The first painting, named dummy painting A, was made exactly according to the standard process described above. Its canvas, made of linen plain cloth, was uniformly stretched and stapled to the wooden strainer. The weaving orientation of the canvas is oriented in a regular way, i.e., parallel to the strainer. Due to aging, the canvas of a real painting will warp and distort slightly. This will affect its vibration characteristics. However, it is difficult to produce such an aged dummy painting. As a simplification, it is assumed that the distribution of distortion has little influence on the vibration characteristics and in this case the dummy painting with a tilted canvas is used to approximate it. This second painting is named dummy painting B and its canvas is oriented with a 10° tilt angle to strainer. Figure 2.3 shows the difference between the canvases of dummy painting A and B.

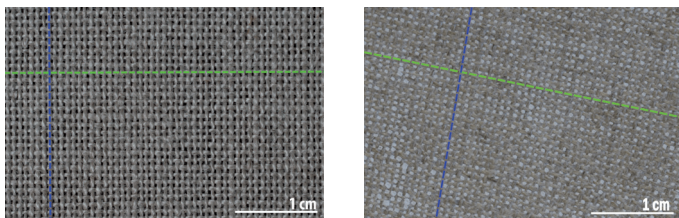


Figure 2.3: The canvases with regular (left) and slightly tilted orientation (right).

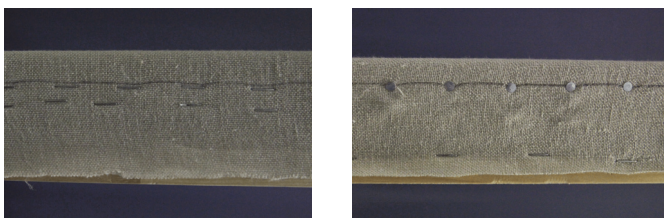


Figure 2.4: The canvas for dummy painting A secured with staples (left) and the canvas for dummy painting C secured with nails (right).

Throughout history, the materials and methods used to attach the canvas to its stretcher or strainer have evolved from lacing, wooden pegs, glue, tacks, and nails to more modern staples and splines. The dummy paintings produced for this thesis are of the common type in which the canvas supports are stretched around the sides of the stretcher, and usually secured to the stretcher with nails or staples along the tacking margin. The dummy painting A and B above were secured with staples. In order to compare the influence of different securing methods on the vibration characteristics of the paintings, a third painting

using nails to secure the canvas was produced, named dummy painting C. A comparison of the securing method for the dummy painting A and C is shown in Fig. 2.4. In addition, the differences between the three dummy paintings are summarized in Table 2.1.

Table 2.1: Differences between the three dummy paintings.

| | dummy painting A | dummy painting B | dummy painting C |
|---------------------|------------------|------------------|------------------|
| weaving orientation | regular | tilted | regular |
| securing method | staple | staple | nail |

2.1.2 Primed Dummy Paintings

After completing the experimental study on the dynamic characteristics of the unprimed dummy paintings, they were primed to further investigate the changes in their dynamic characteristics. A mixture of Champagne and Bologna chalk, as well as gelatine as a binder was prepared as a primer by experienced conservators. The dry and sieved chalk mixture was dumped into the gelatine solution and heated. For uniform mixing, the warm chalk base was subsequently passed twice through a polishing sieve. Before primer application, a pre-gluing was applied to the unstretched canvas. The pre-gluing consisting of a heated gelatine solution (gelatine dissolved in demineralized water), was applied generously to the canvas with a brush and dried for one day. Finally, liquid form of the heated primer compound was applied on one side of the canvas surface in several layers with a brush. Following a period of drying, the primed dummy paintings can be used for testing. The details of applying primer as described above is referred to [Hartlieb21]. Taking the dummy painting B as an example, the finished painting after the application of primer is shown in Fig. 2.5. It can be seen that the warm primer penetrated the other side of the canvas in some places during application.

2.1.3 A Painted Dummy Painting

The three aforementioned dummy paintings with unprimed and primed canvases are sufficient to compare with real paintings in order to summarize the general modal characteristics of paintings. However, an intentionally simplified painted dummy model of real paintings is still necessary to assess whether some of the observed properties change with those simplification. Therefore, as shown in Fig. 2.6, a painted dummy painting D with the logo of the authors' institute was produced, which measures 60 cm × 70 cm × 4 cm. The dummy painting D does not have the same structure as the other three dummy paintings. Its production process is similar to that in [Hartlieb21]. Its canvas was similarly decatised

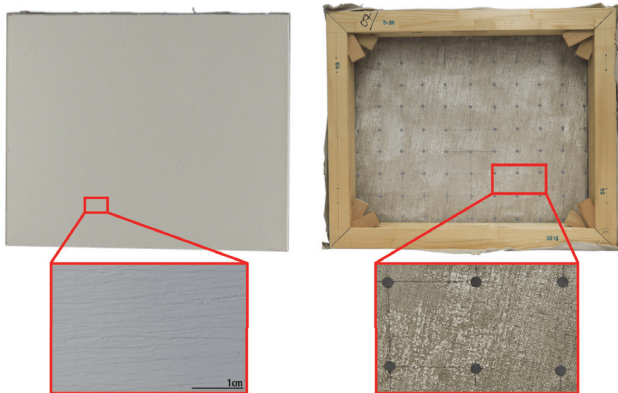


Figure 2.5: The primed dummy painting B: Primer layer on the front (left); Primer penetrated to the backside (right).

and then uniformly tensioned on a biaxial stretcher. Next, the stretched canvas was treated with a pre-gluing to prevent the primer from permeating into the canvas in the next step. The primer was heated and then applied on the canvas in three layers with a brush from different directions. The blue oil paint layer and the white paint layer were also applied sequentially on the primer layer with a brush. Lastly, the canvas was sandwiched between two wooden interchangeable stretchers. In contrast to the conventional clamping methods described in section 2.1.1, the use of an interchangeable stretcher ensures a homogeneous distribution of tension in the canvas. The interchangeable stretcher consists of a front and a back, which are screwed together so that the canvas is sandwiched. This enables a consistent and even tension.

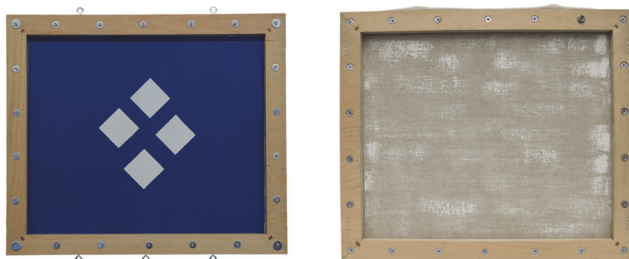


Figure 2.6: The front (left) and back (right) of the finished painted dummy painting.

2.2 Real Paintings

Besides the dummy paintings mentioned above, three real paintings are also investigated to compare their modal characteristics with those of the dummy paintings or to use them in transport experiments. These real paintings, though of negligible artistic value, have become fragile and massively damaged after natural aging. They would not have been transported in this condition as part of the museum loan system without consolidation measures. A knowledge about their material composition of paint layers and the canvas is not relevant to this thesis, so they will not be provided here. According to the signature, the first real painting shows a seascape by J. Metzler (undated) with the dimensions 50 cm × 60.7 cm × 2 cm, see Fig. 2.7. This painting is probably painted with oil paint on the textile, linen-bound support. It is a naturally aged object with loose, roof-shaped, protruding paint layers. The back of the strainer is equipped with four perforated metal plates to facilitate hanging the painting during experiments.



Figure 2.7: The front (left) and back (right) of the seascape.



Figure 2.8: The front (left) and back (right) of the still life.

The next real painting is a depiction of a floral still life with dimensions 57 cm × 46 cm × 2 cm, as shown in Fig. 2.8. It was created by J. Bummed, but the specific creation time is

unknown. The paint layer is applied comparatively thickly in this painting. There is a pronounced relief in the area of the petals. The painting's layered structure is characterized by craquelure. In addition, the damage pattern 'bowl formation' can be attested. Restoration measures are evident in the marginal area in the form of an indented edge. Tensioners are mounted on the four corners of the back of the strainer to prevent further damage. The strainer of this painting is also fitted with four perforated metal plates.

The last real painting on canvas shows a landscape and has outer dimensions 49 cm × 65 cm × 1.8 cm, see Fig. 2.9. The artist who created this painting is unknown, but art conservators estimate that it was painted in the early 20th century. The painting has also been severely aged, with the paint layer peeling off in many places and the strainer has become a little distorted. Its strainer is different from the previous two paintings, with an extra wooden beam in the middle. Four specially designed hanging systems are mounted on the strainer.



Figure 2.9: The front (left) and back (right) of the landscape.

2.3 Orientation of Paintings

The motion of a painting in space consists of six degrees of freedom. In order to conveniently describe the motion of the individual degrees of freedom later on, it is essential to establish a generalized definition of the painting's orientation. In this thesis, a right-handed spatial Cartesian coordinate system is used to construct the orientation of the painting. When the painting is at rest, the surface of the painting is defined as the xy -plane by ignoring the unevenness of the primer or paint layer. In this case, the center of the painting surface is always taken as the origin O . The width of the painting corresponds to the longitudinal axis (x -axis), with its positive direction to the right when facing the front of the painting. Simultaneously, the height of the painting represents the vertical axis (y -axis), and its positive direction is upwards when facing the front of the painting. Consequently, by definition of the right-handed coordinate system, the direction perpendicular to the surface

of the painting, extending outward, is designated as the positive direction of the transverse axis (z -axis). Moreover, during the transport experiment, the painting is placed inside the packing case, securely positioned within the transport vehicle. The securing process ensures that the x -axis of the painting remains parallel to the forward direction, while the y -axis remains perpendicular to the ground. An example of the above painting orientation is shown in Fig. 2.10. This coordinated framework provides a systematic and standardized basis for articulating the spatial orientation of the painting throughout the analysis.

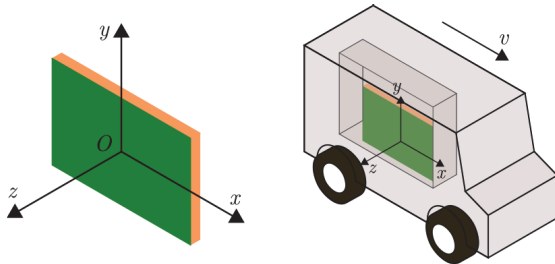


Figure 2.10: Coordinate system of a painting at rest (left) and its orientation during transport (right).

Chapter 3

Modal Characteristics of Paintings

Art conservators have long recognized the importance of studying the inherent properties of paintings to protect them from shock and vibration during transport. In the beginning, they focused on the mechanical properties of paintings, such as the stress-strain curves of different canvases and paint layers under static loads and different degrees of aging, see [Mecklenburg82, MecklenburgTumosa91a, DePoloEtAl21]. However, this is not enough to guide how to improve the transport environment, because the paintings during transport are subjected to dynamic loads. Although it has been recognized in [Marcon91a, Marcon91b] that, in a dynamic vehicle environment, when the frequency of the forced vibration is near the eigenfrequency of paintings, it leads to a condition known as resonance, where the vibration of the painting will exceed the input vibration level and dangerously large oscillations may occur, the dynamics of the painting itself have not yet been revealed due to limitations in measurement techniques.

With the help of modern measurement techniques, including accelerometers and contactless measurement methods, art conservators have made more progress in the study of the dynamic characteristics of paintings. They recorded the vibration signals of transport crates or strainers on different vehicles during transport, which showed that the influence of vibration on paintings is not negligible during transport [Saunders98, Gmach10, Braun13, TveitGonenErduran22]. Further, art conservators evaluated the transport conditions based on collected data [CerkanowiczEtAl17] and simulated the transport damage to the paintings [TsiranidouEtAl13, TornariTsiranidouBernikola14]. In particular, the frequency response functions (FRFs) of several points on the canvas were measured by real transport experiments or transport simulations in [Palmbach07, HeinemannEtAl19], shedding light for the first time on some of the dynamic characteristics of paintings, such as the distribution of eigenfrequencies. Unfortunately, the confined transport environment does not allow for a more comprehensive observation of the dynamic characteristics of paintings.

For this reason, art conservators have chosen to investigate the dynamic characteristics of paintings within controlled laboratory settings. In an interesting study, Kracht conducted

a comprehensive examination of these dynamic characteristics [Kracht11]. She crafted several dummy paintings, each with a distinct layer structure, and aged them to varying degrees in a controlled drying oven. Her experimental setup employed an electrodynamical shaker to apply mechanical loads to the tested dummy paintings. A force sensor was used to capture the excitation, while a Laser Doppler Vibrometer recorded the response of the lattice on the canvas. Using the data gathered, a modal analysis was conducted to identify variations in the dynamic characteristics of the dummy paintings at different stages of aging. These variations included differences in eigenfrequencies and eigenmodes. Similarly, in [Hartlieb21], it was measured and analyzed for the influence of different fiber types, primer layer thicknesses, fabric weave formats, different fabric pretreatment, clamping forces, and ambient humidity on the eigenfrequencies of the paintings on textile supports. In contrast to experimental studies, the vibration of canvas paintings was characterized by establishing a finite element (FE) model [ChiribogaArroyo13], which treated paintings as orthotropic laminated plates under biaxial tension. This FE model was capable of predicting the first two eigenfrequencies of paintings with differences within 5% compared to the experimental results. The non-uniform biaxial tension applied during the tests and the simplified linear elastic material model adopted for canvas textiles limited the performance of the FE model. As for such inhomogeneities, which include tension and material properties, their influence on the dynamic characteristics of paintings has been thoroughly investigated in [MayLlorens21] also by means of finite element method.

As a result of the above studies, a preliminary knowledge of the dynamic characteristics of paintings has been gained. Building on these efforts, this chapter further investigates the dynamic characteristics of paintings through experimental modal analysis. The eigenfrequencies, damping, and eigenmodes of different dummy paintings before and after the application of primer, as well as of the real paintings, are extracted from the experimental data. Accordingly, the modal characteristics of these paintings in different states are discussed and their modal models are reconstructed. Moreover, a large number of studies have shown that the material properties of paintings are affected by climate, see, e.g. [Mecklenburg82, Michalski91, MecklenburgTumosa91b]. It is also mentioned in [Hartlieb21] that the eigenfrequencies of paintings are affected by humidity. Therefore, the relationship between the modal characteristics of paintings and climate is also addressed in this chapter.

The chapter starts by introducing the theoretical background of the frequently used experimental modal analysis method. Furthermore, the mathematical and finite element models of the membrane used as the most simplified mechanical model of paintings is introduced. The subsequent Section 4.3 focuses on the process of the experimental modal analysis of paintings, the modal characteristics of paintings and the comparison with the most simplified model. Subsequently, the influence of climate on the modal characteristics of paintings and their relationship are investigated in Section 4.4. Throughout the thesis, the study of modal characteristics of paintings is the basis and reference for Chapters 4

and 5. This chapter follows the findings published in [GaoEtAl23b] while adding a discussion about the modal characteristics of real paintings.

3.1 Theoretical Background of Experimental Modal Analysis

As described in Chapter 2, the painting itself is a composite structure composed of layers of different materials. Moreover, the materials in each layer are not uniformly distributed and their properties are not homogeneous. This makes it extremely difficult to analyze the dynamic characteristics of the painting through numerical modeling techniques. Therefore, experimental modal analysis becomes the simplest and most effective way. During experimental modal analysis, the transient system response is first measured and processed. Then, the modal parameters are identified from system response, and the commonalities in painting dynamics can be analyzed accordingly. The identified modal parameters can also be used to construct a structural model of the painting. Besides the general methodology of experimental modal analysis, the related methodology of this thesis based on singular value decomposition (SVD) is described in more detail.

3.1.1 Frequency Response Function

A complete experimental modal analysis can usually be divided into the following components: theoretical basis of vibration, measurement of vibration, data analysis and parameter identification. First, as a theoretical basis it is described here as succinctly as possible. For a comprehensive review of the theory, the reader is referred to existing textbooks, e.g. [Ewins09, MaiaEtAl97]. In this thesis, the painting is described as a linear time-invariant multi-degree-of-freedom (MDOF) system containing viscous damping. For a damped MDOF system with N degrees of freedom, the governing equations of motion can be written in matrix form as

$$\mathbf{M}\ddot{\mathbf{x}}(t) + \mathbf{C}\dot{\mathbf{x}}(t) + \mathbf{K}\mathbf{x}(t) = \mathbf{f}(t), \quad (3.1)$$

where $\mathbf{M} \in \mathbb{R}^{N \times N}$, $\mathbf{C} \in \mathbb{R}^{N \times N}$ and $\mathbf{K} \in \mathbb{R}^{N \times N}$ are mass, viscous damping and stiffness matrices, respectively, and $\mathbf{x}(t) \in \mathbb{R}^N$ and $\mathbf{f}(t) \in \mathbb{R}^N$ are time-varying displacements and forces. The frequency response function $H_{jk}(\omega)$ of this MDOF system, representing the harmonic response X_j in one degree of freedom j caused by a single harmonic force F_k applied at a different degree of freedom k , has the general form

$$H_{jk}(\omega) = \frac{X_j(\omega)}{F_k(\omega)} = \sum_{r=1}^N \frac{r A_{jk}}{\lambda_r^2 - \omega^2}, \quad (3.2)$$

where λ_r^2 is the eigenvalue of the r^{th} mode and $_rA_{jk}$ is the modal constant corresponding to that mode, the output at the j^{th} element, and the input at the k^{th} element. Usually vibration is measured in terms of displacement, velocity or acceleration, and, therefore, the corresponding FRF (3.2) may be presented in terms of receptance, mobility or acceleration. The modal constant is constructed from

$$_rA_{jk} = \phi_{jr}\phi_{kr} \quad (3.3)$$

where ϕ_{jr} is the j^{th} element of the r^{th} eigenvector ϕ_r , i.e. the relative motion at that DOF during vibration in the r^{th} mode. Each eigenvalue λ_r^2 can be expressed as

$$\lambda_r^2 = \omega_r^2 + 2i\omega_r\omega\zeta_r \quad (3.4)$$

combining the eigenfrequency ω_r and the critical damping ratio ζ_r for that mode. A direct relationship between the modal parameters (the eigenfrequencies ω_r , the eigenmodes ϕ_r , the modal damping ratios ζ_r , and the frequency response function $H_{jk}(\omega)$) is established through the expressions (3.2–3.4). It forms the cornerstone of modal analysis, because it not only shows that the response of the system can be predicted from the modal parameters, but also clearly implies the possibility of identifying the modal parameters from the frequency response function.

The second focus of the experimental modal analysis is the choice of measurement techniques which are used for modal testing, including the mechanical aspects of structure preparation, excitation of the structure, transducers, and amplifiers. The first decision which has to be taken is whether the structure is to be tested in a 'free', 'grounded' or 'loaded' condition. By 'free' is meant that the test object is, in effect, freely suspended in space using very soft springs. The opposite support is referred to as 'grounded' because it attempts to fix selected points on the structure to ground. While the 'loaded' condition is a compromise procedure between the two above, i.e. the test object is connected at certain coordinates to another simple component of known mobility, such as a specific mass. Based on the practicalities of the painting during transport, 'free' or 'loaded' conditions are usually preferred when simulating the boundary conditions of the painting [Ewins09].

Various devices are available for exciting the structure. Basically, they can be divided into two types: contacting and non-contacting. The first and most common option is to connect some form of shaker or vibrator to the structure throughout the test, regardless of whether the type of excitation is continuous (harmonic, broadband, or random, etc.) or transient (impulse, chirp). The second type consists of devices that do not make contact throughout the vibration (e.g., non-contacting electromagnet or loudspeaker), or that only make contact for a short period when the excitation is applied (e.g., manual hammers). Non-contacting excitation is particularly suitable for testing precious paintings, therefore this thesis attempts both of these excitation methods.

To date, using a piezoelectric sensor is the most common and widely used method for measuring parameters of interest in modal tests. Piezoelectric force sensor can measure the

excitation and piezoelectric acceleration sensor can measure the response of the structure. Both must be selected to ensure that the sensor interferes as little as possible with the test structure and that the operating range of the sensor should match the frequency and amplitude encountered in the system. Moreover, there is increasing use being made of optical and, in particular, of Laser Doppler Vibrometers (LDVs) which have a major advantage in the non-intrusive nature of their operation. The basic LDV transducer is a device which is capable of detecting the instantaneous velocity or displacement of the surface of a structure. Equipped with a mirroring system (scanning LDVs), it can also automatically measure multiple points, with the main disadvantage of the higher cost [Polytec12]. In principle, it is possible to identify all eigenfrequencies in the excitable and measurable frequency range with a single input/output combination, but to identify eigenmodes, measurements must be conducted at multiple input or output locations. The scanning LDV facilitates multiple output measurements, and moving the excitation position is the simplest way to obtain multiple input positions. Therefore, for modal testing in this thesis the piezoelectric force sensor is mainly used to measure the excitation and the scanning LDV is used to measure the vibration on the surface of the tested painting.

The raw data collected from the modal tests have to be processed as appropriate by filtering, windowing, and spectrum analysis. The FRF is then calculated or estimated depending on the type of excitation. For transient or periodic excitation, the discrete Fourier transform is computed of both the force and response signals and the ratio of these transforms gives the FRF, just as in Equation (3.2). For a truly random excitation or an imperfect measurement with noisy data, although Equation (3.2) can be used as well, a more accurate estimate of the FRF can be obtained by the following equations

$$H_1(\omega) = \frac{S_{xf}(\omega)}{S_{ff}(\omega)} \quad \text{and} \quad H_2(\omega) = \frac{S_{xx}(\omega)}{S_{xf}(\omega)}, \quad (3.5)$$

where $S_{xx}(\omega)$, $S_{ff}(\omega)$, $S_{xf}(\omega)$ are the auto spectra of the response and excitation signals and the cross spectrum between these two signals, respectively, and $H_1(\omega)$ and $H_2(\omega)$ are the frequency response functions linking the structure response x and excitation f . The noise in the acquired data is likely to influence the force signal near resonance, thus making $S_{ff}(\omega)$ vulnerable, whereas at antiresonance it is the response signal which will suffer, making $S_{xx}(\omega)$ prone to errors. In the first case, $H_1(\omega)$ will suffer most, hence $H_2(\omega)$ might be a better indicator near resonance while the reverse applied at antiresonance [Ewins09].

The final step in the experimental modal analysis is to extract the modal parameters of the test structure from the measured signals using the relationships in Eqs. (3.2 – 3.4). A large number of modal analysis methods, each with its own advantages and disadvantages, have been developed to address this problem. They can be classified into a series of different groups. First of all, it is appropriate to define the domain in which the analysis is performed as the frequency domain and time domain. The time domain methods work directly on transient signals, while the frequency domain methods

extract modal parameters from the frequency response function. A classical time domain method, the Ibrahim time domain method, is effective in identifying modal parameters from free oscillations, but is accurate only for the dominant modes [IbrahimMikulcik77]. The next group considers the frequency range over which each individual analysis will be performed, and this divides into two categories, also, depending upon whether a single mode is to be extracted at a time, or several, i.e. single-degree-of-freedom (SDOF) and multi-degree-of-freedom (MDOF) methods. The typical SDOF methods in the frequency domain, such as peak amplitude, circle fit and least-squares peak fitting method, all yield correct results as long as the eigenfrequency peaks are clearly separated. The MDOF methods, such as the nonlinear least squares method and the rational fractional polynomial method, determine the modal parameters of multiple modes at once, but lead to the problem of high numerical requirements. For a thorough classification and details of these methods, see [Ewins09, MaiaEtAl97]. Since many of the methods mentioned above aim to fit polynomials, they can be assembled following the unified matrix polynomial method proposed by [AllemandBrown98].

3.1.2 Modal Parameter Identification Based on SVD

In this thesis multi-reference impact tests are typically used for experimental modal analysis and the experimental data consist a relatively large number of measurement DOFs. In order to preprocess this data, an approach based on SVD called the complex mode indicator function (CMIF), combined with the enhanced frequency response functions (EFRF), is used to convert data to make it applicable for the SDOF methods. The modal parameters are then extracted using a least-squares peak fitting algorithm. In the following, the methods used above are briefly explained, while a detailed description of these methods can be referred to [AllemandBrown06].

Several FRFs have been acquired from several references after a multi-reference impact test. The Fourier transforms of the input force $f_k(t)$ and output response $x_j(t)$ are $F_k(\omega)$ and $X_j(\omega)$. The input positions are denoted $k = 1, 2, \dots, K$ and the output positions are denoted $j = 1, 2, \dots, J$. Accordingly, the set of FRFs which are used to provide a basis for the parameter identification with the modal analysis are stored in a series of vectors, $\mathbf{H}(\omega) \in \mathbb{C}^{J \times K}$, each of which contains the values for one FRF at all measured frequencies. Then, an SVD is performed on the matrix, $\mathbf{H}(\omega)$, at each considered frequency, resulting in the CMIF with possibly complex singular vectors. However, an alternate form of the SVD approach to the CMIF is often used that will generate a real singular vector, which is necessary to adopt the EFRF method. Noting that the imaginary part of the FRF matrix, for receptance or acceleration, is much more discriminating with respect to close modal frequencies, only the imaginary part of the FRF matrix is used in the computation of CMIF. While in the case of mobility, the real part of the FRF matrix should be used in

the SVD to form

$$\text{Re}(\mathbf{H}(\omega)) = \mathbf{U}(\omega)\Sigma(\omega)\mathbf{V}(\omega)^H \quad (3.6)$$

where $\mathbf{U}(\omega) \in \mathbb{C}^{J \times J}$ is the matrix of left singular vectors, $\mathbf{V}(\omega) \in \mathbb{C}^{K \times K}$ is the matrix of right singular vectors and $\Sigma(\omega) \in \mathbb{R}^{J \times K}$ is the matrix of singular values. The superscript H denotes the Hermitian of a matrix. In any event, the number of driving points associated with the inputs and outputs will be referred to as the number of references. For the purposes of this thesis, the number of inputs k is assumed to be less than the number of outputs j , and, therefore, the inputs are used as the references. For each reference one singular value can be calculated. The singular values as a function of the considered frequencies then form the CMIF

$$CMIF_k(\omega) = \Sigma_k(\omega) \quad \text{with } k = 1, 2, \dots, K, \quad (3.7)$$

which contains a vector with K items at each spectral line and indicates all modes existent in the FRF matrix. The advantage of CMIF over a single FRF is that it synthesizes all the information from the FRF matrix, resulting in distinct peaks at all eigenfrequencies in the CMIF. Even for the closely spaced modes, the CMIF can offer better discrimination in multiple curves. Consequently, the peak detected in the CMIF indicate the existence of modes, and the corresponding frequencies of these peaks give an estimate for the damped eigenfrequencies for each mode. It is also worth noting that the left singular vectors at these frequencies are usually already quite good approximations for the mode shapes of the structure.

In addition to identifying all the significant eigenfrequencies, including double or multiple modes, the CMIF can also be used to generate a set of enhanced FRFs from

$$\hat{H}_r(\omega) = \mathbf{u}_r^T \mathbf{H}(\omega) \mathbf{v}_r = \frac{r \hat{A}}{\lambda_r^2 - \omega^2}, \quad (3.8)$$

where $\mathbf{u}_r(\omega_r) \in \mathbb{R}^{J \times 1}$, $\mathbf{v}_r(\omega_r) \in \mathbb{R}^{K \times 1}$ and $r \hat{A}$ are the left singular vectors, the right singular vectors and the modal constants of the EFRFs at the identified eigenfrequencies ω_r , respectively. If the spatial resolution of measurements is sufficiently high, there is one non-trivial EFRF for each mode, the result of which is an almost SDOF characteristic response function. Then it is readily amenable to identify the modal parameters with high precision for each mode separately from the corresponding EFRF by the simplest SDOF parameter identification techniques. Since the Equation (3.8) is a complex equation, two real equations can be obtained by separating the real and imaginary parts at each frequency point. In this thesis, a least-squares peak fitting method is applied to identify

the parameters ω_r , ζ_r and ${}_r\hat{A}$ from the EFRFs in the form

$$\begin{bmatrix} \text{Re}(\hat{H}_r(\omega_1)) & -2\text{Im}(\hat{H}_r(\omega_1))\omega_1 & -1 & 0 \\ \text{Im}(\hat{H}_r(\omega_1)) & 2\text{Re}(\hat{H}_r(\omega_1))\omega_1 & 0 & -1 \\ \text{Re}(\hat{H}_r(\omega_2)) & -2\text{Im}(\hat{H}_r(\omega_2))\omega_2 & -1 & 0 \\ \text{Im}(\hat{H}_r(\omega_2)) & 2\text{Re}(\hat{H}_r(\omega_2))\omega_2 & 0 & -1 \\ \vdots & \vdots & & \\ \text{Re}(\hat{H}_r(\omega_L)) & -2\text{Im}(\hat{H}_r(\omega_L))\omega_L & -1 & 0 \\ \text{Im}(\hat{H}_r(\omega_L)) & 2\text{Re}(\hat{H}_r(\omega_L))\omega_L & 0 & -1 \end{bmatrix} \begin{bmatrix} \omega_r^2 \\ \omega_r\zeta_r \\ \text{Re}({}_r\hat{A}) \\ \text{Im}({}_r\hat{A}) \end{bmatrix} = \begin{bmatrix} \omega_1^2\text{Re}(\hat{H}_r(\omega_1)) \\ \omega_1^2\text{Im}(\hat{H}_r(\omega_1)) \\ \omega_2^2\text{Re}(\hat{H}_r(\omega_2)) \\ \omega_2^2\text{Im}(\hat{H}_r(\omega_2)) \\ \vdots \\ \omega_L^2\text{Re}(\hat{H}_r(\omega_L)) \\ \omega_L^2\text{Im}(\hat{H}_r(\omega_L)) \end{bmatrix} \quad (3.9)$$

where L is a user defined number of discrete frequency points, at least two, in the vicinity of the peak in Equation (3.8). For a complete description of this algorithm it can be found in [AllemandBrown22].

With the identified modal parameters, the EFRFs are possible to be reconstructed as a separate SDOF system

$$\hat{H}_r^{\text{rec}}(\omega) = \frac{{}_r\hat{A}}{\omega_r^2 - \omega^2 + 2i\omega_r\omega\zeta_r}. \quad (3.10)$$

All these reconstructed EFRFs are transformed back in to the physical domain and summed up, resulting in the frequency response function matrix

$$\mathbf{H}^{\text{rec}}(\omega) = \sum_{r=1}^R \mathbf{u}_r \hat{H}_r^{\text{rec}}(\omega) \mathbf{v}_r^T, \quad (3.11)$$

where R is the total number of identified eigenmodes in the considered frequency range and $\mathbf{H}^{\text{rec}}(\omega)$ has the same size as $\mathbf{H}(\omega)$. Correspondingly, the modal constants ${}_r\mathbf{A}$ of the frequency response function in the physical domain are calculated by a similar method through

$${}_r\mathbf{A} = \mathbf{u}_r {}_r\hat{A} \mathbf{v}_r^T \quad (3.12)$$

for each mode separately. The eigenmodes of the test structure can then be determined according to Equation (3.3). At this point, all the modal parameters of interest to the test structure are successfully identified.

3.2 Simplified Mechanical Model of Paintings

A painting model is useful for predicting the behavior of the structure under vibration loading and determining the frequencies and amplitudes that can be potentially harmful for the painting. However, virtually no modeling has yet been performed to describe the dynamic behavior of paintings well, because paintings are complex inhomogeneous structures composed of several materials which can change significantly with age. A

wide variety of materials and techniques have been applied depending on the artist's period or style, making it difficult to characterize a general class of paintings in either a mathematical [AubryPostleRenner99] or an FE model [ChiribogaArroyo13]. Nevertheless, in this thesis the most simplified mechanical models of the painting have been developed through mathematical and FE methods. Although the simplified model will turn out to show a somewhat different modal behavior from the investigated paintings, it can still provide some simplified idea of the modal behavior which can make it easier to understand the reason for some basic behavior. Moreover, in principle, the general tendencies for the lower order modes derived from the simplified model are still valid, such as the eigenmodes and the distribution of eigenfrequencies. Therefore, although very simplified, the mathematical and FE models are used for comparison with the modal characteristics of the investigated paintings.

3.2.1 Mathematical Model

The painting and the membrane are stretched and then fixed along their edge, and their twisting and bending moments are small enough to be considered as negligible as a first approximation. For this reason, the membrane is first used as the most simplified mechanical model of the painting. Considering a rectangular vibrating membrane with length a and width b , the governing differential equation of motion for its transverse free vibration is given by

$$c^2 \left(\frac{\partial^2 u}{\partial x^2} + \frac{\partial^2 u}{\partial y^2} \right) = \frac{\partial^2 u}{\partial t^2}. \quad (3.13)$$

By the method of separating variables, the general solution of this governing equation for obtaining the displacement $u(x, y, t)$ of a point (x, y) of the membrane from rest ($u = 0$) at time t is according to [Kreyszig09]

$$u(x, y, t) = \sum_{m=1}^{\infty} \sum_{n=1}^{\infty} u_{mn}(x, y, t) = \sum_{m=1}^{\infty} \sum_{n=1}^{\infty} F_{mn}(t) \Phi_{mn}(x, y) \quad (3.14)$$

with

$$F_{mn}(t) = B_{mn} \cos \lambda_{mn} t + B_{mn}^* \sin \lambda_{mn} t \quad (3.15)$$

and

$$\Phi_{mn}(x, y) = \sin \frac{m\pi x}{a} \sin \frac{n\pi y}{b}, \quad (3.16)$$

where

$$\lambda_{mn} = c\pi \sqrt{\frac{m^2}{a^2} + \frac{n^2}{b^2}}, \quad c^2 = T/\rho, \quad m = 1, 2, \dots, \quad n = 1, 2, \dots. \quad (3.17)$$

In Eqs. (3.13–3.17), T is the tension per unit length caused by stretching the membrane, which is the same in all points and in all directions and does not change during the motion. The homogeneous membrane density is represented by ρ . The different half sine wave

numbers m and n in the length and width directions represent the different vibration patterns.

The displacement $u(x, y, t)$ of a rectangular vibrating membrane is composed of all so called eigenfunctions u_{mn} which themselves can be decomposed into a time domain function $F_{mn}(t)$ and a spatial domain function $\Phi_{mn}(x, y)$. The functions $F_{mn}(t)$ depend on λ_{mn} , B_{mn} and B_{mn}^* . The geometrical quantities B_{mn} and B_{mn}^* can be obtained from initial conditions and the orthogonality of Fourier components. The numbers λ_{mn} are called the eigenvalues. Therefore, the eigenfrequencies of the rectangular membrane are $\lambda_{mn}/2\pi$. Obviously, the eigenfrequencies of the rectangular membrane depend on the tension T , the density ρ and its dimensions a, b . When using Equation (3.17) to estimate the eigenfrequencies of the investigated dummy paintings, it is necessary to identify the tension T and the density ρ , which are difficult to precisely measure for real paintings without disassembling and consequently destroying the paintings.

The spatial domain functions $\Phi_{mn}(x, y)$ are called eigenmodes and represent vibration patterns. The eigenmodes depend only on the dimensions of rectangular membrane a and b . Therefore, substituting $a = 50\text{ cm}$ and $b = 60\text{ cm}$ into $\Phi_{mn}(x, y)$, the first eight eigenmodes of the rectangular membrane with the same dimensions as the investigated dummy paintings can be obtained, as shown in Fig. 3.1. These eigenmodes are used for comparison with the measured eigenmodes of the investigated dummy paintings.

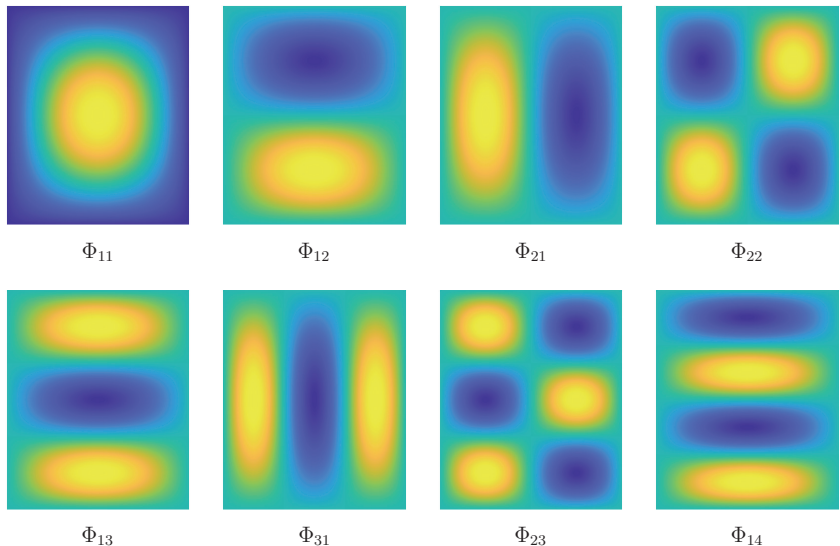


Figure 3.1: The first eight computed eigenmodes of the standard rectangular membrane.

3.2.2 Finite Element Model

The most simplified mathematical model offers foundational insights into the modal characteristics of paintings. However, due to their inherent inhomogeneity and geometric imprecision, it is challenging for mathematical models to describe their influence on modal characteristics. The Finite Element (FE) method stands out as a very powerful and versatile method for finding approximate solutions to engineering problems. In this section, the FE method is utilized to investigate how two typical inhomogeneities, density and tension, influence the modal characteristics of paintings. This analysis is intended to provide additional references to the subsequent experimental modal analysis results. For a comprehensive exploration for the influence of inhomogeneities and geometric imprecision on the modal characteristics of paintings, interested readers are referred to [MayLlorente21].

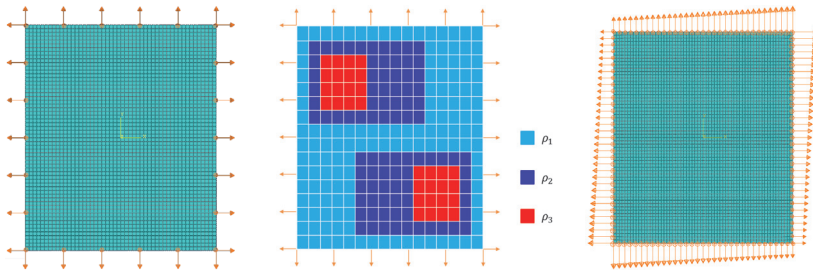


Figure 3.2: Finite element models of the painting: a completely homogeneous painting model (left), a painting model with inhomogeneous density distribution (middle) and a painting model with inhomogeneous tension distribution (right).

The model of the painting vibration was developed using the finite element analysis software package ABAQUS. In order to simplify the analysis as much as possible, the strainer was ignored and the geometry containing the canvas, primer or paint layer was described by a 2D planar shell-shaped part. Its dimensions are the same as those of the dummy paintings A, B and C, a rectangle of $50\text{ cm} \times 60\text{ cm}$. The multilayered material structure of paintings results in extremely inhomogeneous mechanical properties. Since it is a complicated and laborious task to identify the material parameters, and it is not the focus of this thesis, the isotropic material properties are used to describe the canvas. The material properties of the model are Young's modulus $E = 300\text{ MPa}$, Poisson ratio $\nu = 0.3$ and density $\rho = 728.3\text{ kg/m}^3$ [ChiribogaArroyo13]. The section of the canvas is studied using 1.5 mm as the thickness value. The loads and boundary conditions for the static step applied on the canvas are shown in the left of Fig. 3.2. The transverse displacements at all edges of the canvas are suppressed ($\delta_z = 0$). To each edge a fixed displacement constraint ($\delta_x = 0.08\text{ mm}$ or $\delta_y = 0.08\text{ mm}$) is assigned in the normal direction, which will create a uniform tension at the edges in the static step. All other degrees of freedom are

left unconstrained. The geometry is then meshed with quadratic quadrilateral elements of type S8R, and yields a total of 3000 elements, which is sufficient to obtain a converged solution. This completely homogeneous painting model after the static analysis as well as the frequency analysis step achieves eigenmodes that are identical to those of the mathematical model in Fig. 3.1.

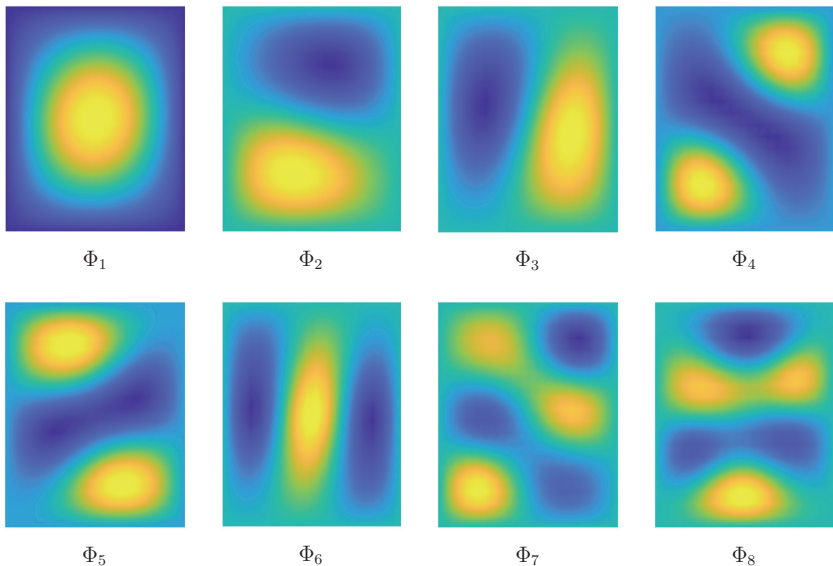


Figure 3.3: The first eight eigenmodes obtained from the FE model when the canvas has inhomogeneous density.

First to be investigated is the influence of inhomogeneous density on the modal characteristics of paintings. The inhomogeneity or specific distribution of paint on real paintings leads to an increase in density in some areas of the canvas. To simulate this situation, as shown in middle of Fig. 3.2, the canvas is divided into three different regions to which different densities are assigned. The red portions represent the lower density with $\rho = 528.3 \text{ kg/m}^3$, the blue portions have a middle density with $\rho = 628.3 \text{ kg/m}^3$, and the cyan portions have a higher density with $\rho = 728.3 \text{ kg/m}^3$. All other parameters are kept consistent with the completely homogeneous painting model. The first eight eigenmodes finally obtained are shown in Fig. 3.3. Compared to the standard eigenmodes in Fig. 3.1, it is clear that all but the first eigenmode are distorted because of the density inhomogeneity. The peaks or valleys of the eigenmode are biased towards the high density region. It is also important to note that the distortion is larger for lower density regions, which means that the absolute peaks in the lower density regions are higher than those in the higher density regions.

Unless a specialized tensioning device is used, it is difficult to ensure that the painting remains an uniform tension when it is being made. Therefore, the changes in the modal characteristics of the painting when the tension is inhomogeneous are investigated next. The most likely scenario for tension in a painting is that it is higher in some parts and lower in others. Similar to the study on inhomogeneous density, different tension distributions are assigned along the edges of the canvas, as shown in the right of Figure 3.2. The tension on each edge is replaced with a linearly varying displacement ($\delta_{\max} = 0.04 \text{ mm}$, $\delta_{\min} = 0.08 \text{ mm}$). Also keeping the other parameters consistent with the completely homogeneous painting model, the first eight eigenmodes are obtained as shown in Fig. 3.4. All the eigenmodes are also distorted due to the inhomogeneity, and the distorted eigenmodes are even similar to the eigenmodes with density inhomogeneity. The analysis also shows that the peaks or valleys of the eigenmodes are shifted towards the region of lower tension. Moreover, since the eigenfrequencies of sixth and seventh eigenmodes are close to each other, their order is exchanged under the influence of the inhomogeneity.

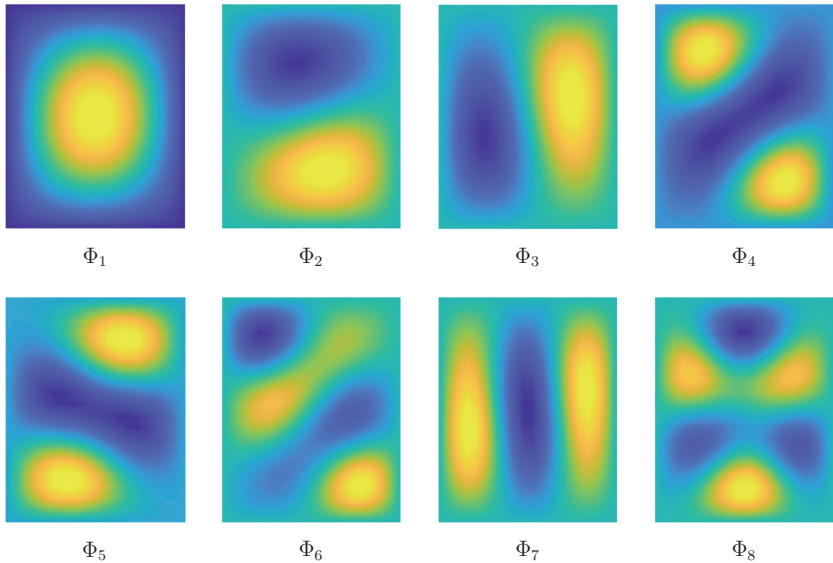


Figure 3.4: The first eight eigenmodes obtained from the FE model when the canvas has inhomogeneous density.

In summary, the inhomogeneity of the parameters in the painting distorts its eigenmodes, as well as disrupts the modal order. Predictably these phenomena will be observed in the experimental modal analysis. However, the fact that different inhomogeneities produce

similar eigenmodes makes it difficult to analyze their causes and only the possibilities can be provided. Nevertheless, the FE method still offers the possibility of establishing a digital twin that can capture the eigenfrequencies and eigenmodes of the real painting.

3.3 Experimental and Numerical Analysis of Paintings

The basic modal characteristics of paintings can be initially revealed using simplified mechanical models. Yet, to fully capture the dynamic characteristics, the investigation on actual paintings becomes imperative. This section attempts to determine the modal parameters of actual paintings through experimental modal analysis. Through this approach, it aims to describe and generalize the complex dynamic characteristics of paintings, bridging the gap between the empirical and numerical domains. Serving as a foundation, Section 3.3.1 describes an experimental setup for identifying the modal parameters of paintings in a non-invasive way, which can also be used for precious paintings. Following this, Section 3.3.2 presents the outcomes of experiment modal analysis for unprimed, primed and real paintings as well as the reconstructed modal models. Thereafter, in Section 3.3.3, a comparative analysis is conducted between the findings of experimental modal analysis and those derived from simplified mechanical models. This comparison aims to summarize the general dynamic characteristics observed in paintings.

3.3.1 Experimental Setup

A setup for conducting the experimental modal analysis is necessary to identify the modal parameters of paintings. The developed experimental setup is shown in Fig. 3.5. It consists of the investigated painting mounted with rubber bands on an aluminum support, an electrodynamical shaker of model PCB TMS-K2007E01, a Polytec PSV-500 scanning Laser Doppler Vibrometer (LDV) and a climate box measuring $2\text{ m} \times 2\text{ m} \times 2.5\text{ m}$ with a humidity controller of model Preservatech Mini One. In order to simulate the state of the painting during transport, the investigated painting is rigidly connected to a wooden plate which is used to install hooks and rubber bands, except that a part of the plate is removed to allow the LDV to physically access the canvas. Four hooks are installed on the upper and lower sides of the wooden plate. Then, rubber bands hang the entire experimental object on the aluminum support through the hooks, forming a very soft suspension which can be approximately considered as a free suspension.

During the experimental modal analysis of this thesis, the input of the system is the exciting force, and the output is the vibration velocity of the canvas. Hence, the so-called



Figure 3.5: The experimental setup for modal analysis of paintings in a climate box.

mobilities are measured. First, mainly an impulse excitation was adopted for experimental modal analysis to identify the modal parameters of the investigated painting. It was generated by an electrodynamical shaker and directly acted on the attached wooden plate of the investigated painting from the back. The electrodynamical shaker has a modified tip mechanism that generates a very short hit and avoids double hits. Essentially, the shaker plus tip mechanism composes an automatic impulse hammer. During measurements, a signal generator automatically provided the shaker with a short trigger signal which led to a single hammering motion of the shaker. The contact force between the investigated painting strainer and the shaker was measured by an integrated circuit piezoelectric (ICP) sensor of model PCB 208C01. The shaker can be moved horizontally to accomplish multiple excitation positions.

Furthermore, for the purpose of measuring the vibration velocity, 99 reflective stickers were attached to the back of the canvas of all dummy paintings, spaced 5 cm apart. Such an operation is necessary for normal LDVs, but impractical for real paintings. Therefore, an advanced PSV-500 Xtra scanning head was adopted, which allowed unprocessed surface to be measured. In this case, the measurement points were created manually in the software. An approximate 11×9 array composed of all measurement points is sufficient to robustly identify at least the first 8 eigenmodes of the investigated painting. The velocity response at predefined points on the canvas was then measured with the LDV which can automatically scan all measurement points sequentially without moving the LDV. Every measurement resulted in the number of output positions $J = 99$. In addition, the number of excitation positions was $K = 3$ at three different locations on the bottom of the wooden plate. Consequently, for the experimental modal analysis of the specific painting, a total of 297 mobilities were measured. Each measurement point took $T = 10$ s with a time resolution of $\Delta t = 5 \cdot 10^{-5}$ s, resulting in a frequency resolution of $\Delta f = 0.1$ Hz

and $N_{\text{fft}} = 200000$ discrete frequencies for their Fourier transforms. Longer measurements would result in zero padding due to signal degradation and were therefore avoided. The matrix of mobilities for all discrete frequencies was stored as a three-dimensional array with size $3 \times 297 \times 200000$.

All experiments were carried out in a self-designed and build climate box. The relative humidity adjustment range of the climate box is 35% to 80%, where $55\% \pm 0.5\%$ was used for the experiments if not separately mentioned, and the temperature was kept constant around $22^\circ\text{C} \pm 0.3^\circ\text{C}$. During the experimental modal analysis, the humidity and the temperature in the climate box were kept as stable as possible to minimize the fluctuation of the investigated painting modal parameters.

In order to assess over what frequency range a meaningful parameter identification can be made, a reference to the input force signal is required. In Fig. 3.6, the force signals for 99 consecutive impacts obtained by scanning all the measurement points of the painting at a fixed excitation reference are displayed in the time and frequency domain. First of all, the signal is well shaped without any double hits and the contact time is about 1 ms. The signal yields a very good reproducibility, with each impact producing almost the same force. From the curves in the frequency range, it can be further concluded that the excitation is good for frequencies below 1000 Hz, as the signal at that frequency has only about 3 dB of attenuation. Actually the vibration of the painting at high frequency is extremely small and their damage to the painting is weak, which means that the high frequency band is not the interested range. Therefore, the quality of the force signal is good enough to accomplish the modal parameter identification.

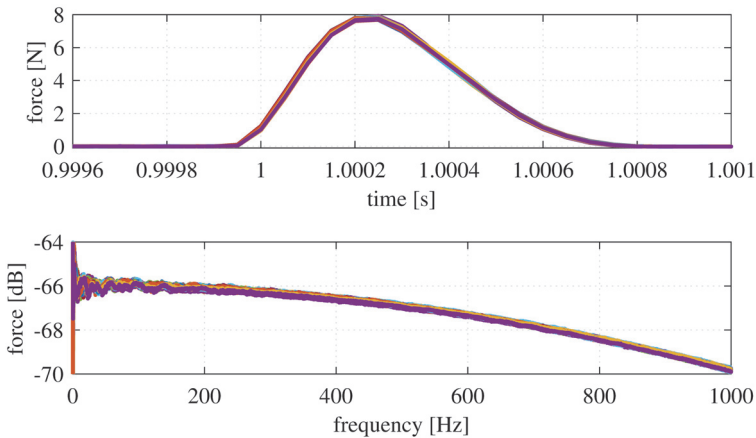


Figure 3.6: 99 consecutive hammer impact signals in the time domain (top) and the frequency domain (bottom).

3.3.2 Modal Parameter Identification

Modal parameter identification is performed using the SVD-based method described in Section 3.1. Hence, after calculating the frequency response function (FRF) from the experimentally collected data, the complex mode indicator function (CMIF) is first calculated to identify possible eigenfrequencies. Then, the enhanced frequency response function (EFRF) is calculated for each identified eigenfrequency, and the modal parameters are fitted by the linear least squares fitting on this EFRF. Based on these identified modal parameters, the modal characteristics of the individual paintings are thus summarized.

3.3.2.1 Unprimed Dummy Paintings

All three unprimed dummy paintings are subjected to experimental modal analysis. Taking the dummy painting A with regular orientation and staple boundary condition as an example, Figure 3.7 shows its CMIF calculated from the mobility matrix in the frequency range up to 120 Hz and highlight the identified eigenfrequencies. Since three different input locations are used, three curves are displayed for the first, second and third singular values at each frequency point. In the evaluated frequency range, about 22 eigenfrequencies are identified, most of which are found in the first CMIF. In the low frequency range up to 11 Hz, due to the soft suspension of the dummy painting, the eigenfrequencies related to rigid body modes are identified. Some distinct peaks are then observed near 48.8 Hz, 97.2 Hz, and 112.2 Hz, which are supposed to be influenced by the eigenmodes of the strainer. Between 11 Hz and 48 Hz, lots of very sharp peaks can be observed that are identified as measurement noise. This is because the soft linen canvas results in small velocity amplitudes, despite the fact that the canvas has been sufficiently tensioned. At the same time, due to the high sensitivity of an LDV, a small signal-to-noise ratio results. In the end, a lot of spurious noise forms these sharp peaks. They are mixed with the eigenmodes of the painting and seriously affect the modal parameter identification. Between 49 Hz and 97 Hz, although there is no effect of spurious noise, the large damping of canvas yields the flat peaks.

At each of the highlighted eigenfrequencies, an EFRF is computed and the parameter identification is carried out based on these EFRFs. In the interest of brevity, only the final results of that procedure are presented hereafter. First of all, by comparing the measured mobilities with the reconstructed mobilities from the identified modal parameters, it is possible to directly assess the results of the modal analysis, and hence, the quality of the identified modal parameters. Consequently, the measured and reconstructed mobilities of unprimed dummy painting A are confronted in Fig. 3.8 in amplitude and phase for one input-output combinations. The reproduction of the peaks mixed with noise as well as the flat peaks is not ideal due to the low signal-to-noise ratio and damping. However, the reconstructed mobilities of all distinct peaks, such as the eigenfrequencies of 48.8 Hz,

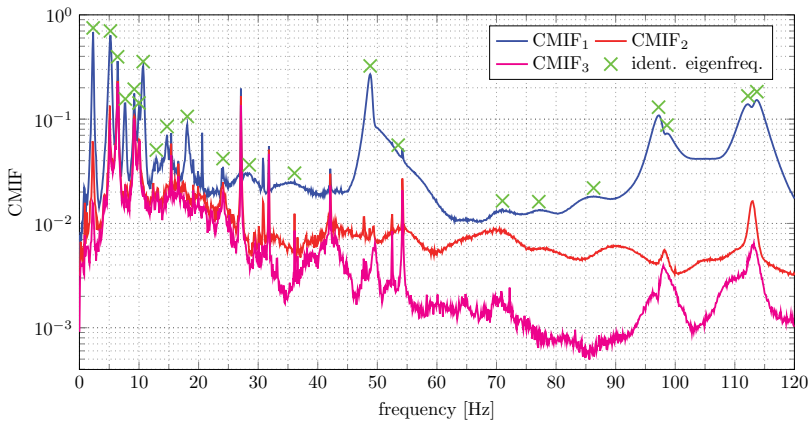


Figure 3.7: CMIF of unprimed dummy painting A with identified eigenfrequency locations.

97.2 Hz and 112.2 Hz, approximate the measurement remarkably well in amplitude and phase, suggesting that the parameter identification there is successful. All in all, the identified modal parameters are not perfect, but they are sufficient to serve as a reference for later discussions and comparisons.

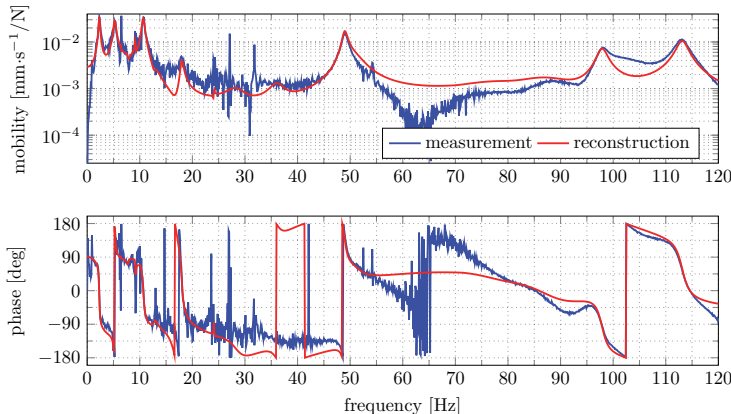


Figure 3.8: Amplitude (top) and phase (bottom) of a mobility excited in the bottom center and measured in the upper right for unprimed dummy painting A.

The next point worth discussing is the identified modal damping ratios ζ_r , which is illustrated in Fig. 3.9. Because the painting is assumed to have viscous damping, all

eigenmodes have their specific damping ratios, which is supported by the identified results. The pronounced peaks are identified with damping ratios lower than 2%, e.g., at the eigenfrequency of 48.8 Hz. Flat peaks are typically identified with higher damping ratios, e.g., up to 8% at the eigenfrequency of 77.1 Hz. Due to the low signal-to-noise ratio, the damping is not identified accurately enough when the eigenmodes and noise are mixed.

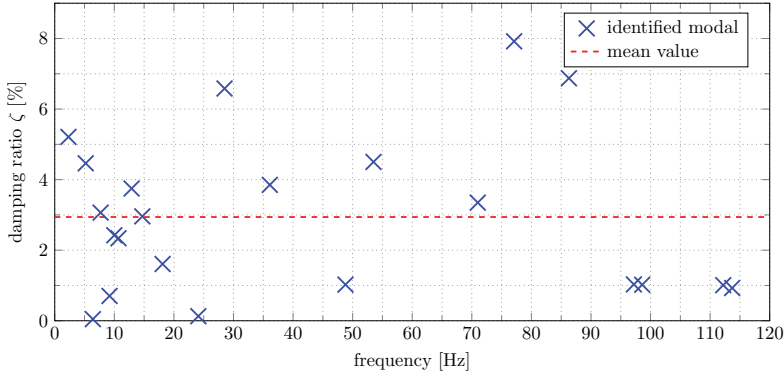


Figure 3.9: Identified modal damping ratios for the unprimed dummy painting A and their mean value.

Furthermore, the eight identified mode shapes with obvious characteristics and their corresponding eigenfrequencies are presented in Fig. 3.10. It should be noted that because it is impossible to determine whether all the eigenmodes of unprimed dummy painting A have been identified, the specific mode order is not marked in Fig. 3.10. Only the mode shapes at 14.7 Hz, 28.5 Hz and 48.8 Hz are observed to be similar to the first, third and fourth eigenmodes of the simplified mechanical model or the FE model, and the most other eigenmodes are incomparable. The higher order mode shapes are even more irregular.

By analyzing the results of the experimental modal analysis on different unprimed dummy paintings, it allows for a discussion of the similarities and differences between their modal characteristics. For the sake of brevity, the experimental modal analysis results for unprimed dummy paintings B and C are not repeated here. They are supplemented in Appendices A.1 and A.2. First of all, all three unprimed dummy paintings encounter the same situation, i.e., due to the soft canvas material, the response of the canvas is weak when being excited. Hence, in the lower frequency range, because of the low signal-to-noise ratio, most of the eigenmodes are drowned out by the noise and difficult to identify, whereas in the higher frequency range, the damping ratio is higher, and the peaks of the eigenmodes are relatively flat. This poses a challenge to the modal parameter identifications and reduces the quality of the parameter identification. Besides, at most only two identified mode shapes are found to be similar to the simplified mechanical model or the FE model

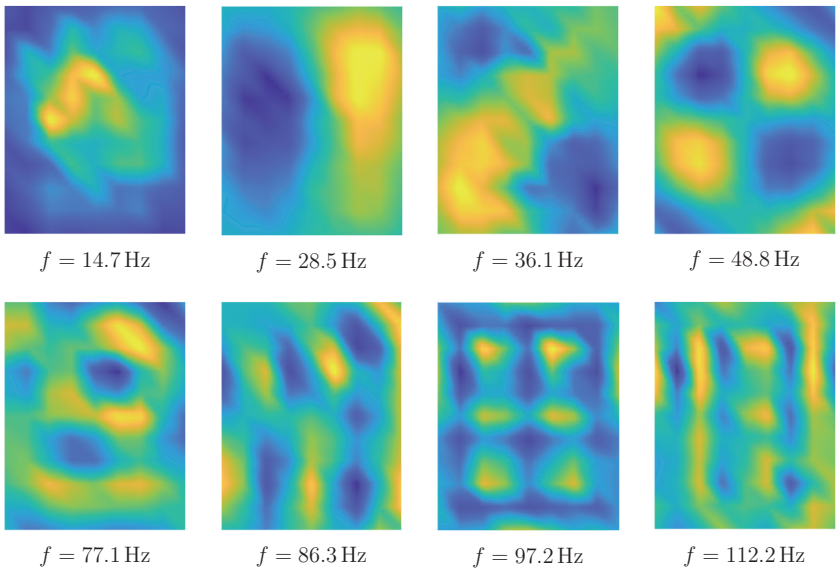


Figure 3.10: The eight identified eigenmodes obtained from the experimental modal analysis for unprimed dummy painting A.

in each painting. Moreover, they all have three pronounced eigenmodes near 49 Hz, 100 Hz, and 112 Hz. Although their mode shapes are not the same, they are considered to be related to use of the same type of strainers.

Specifically, the dummy painting B differs from dummy painting A by the use of a tilted canvas. The mode shapes of dummy painting B at 28.6 Hz, 97.9 Hz, and 112.8 Hz are similar to those of dummy painting A at 28.5 Hz, 92.2 Hz, and 112.2 Hz, but the mode shapes of dummy painting B are more distorted. Thus, the tilted canvas may exacerbate the distortion of eigenmodes. As for dummy painting C, it uses nails to secure the canvas, which leads to the different boundary conditions. However, it possesses a eigenfrequency distribution similar to that of dummy painting A, especially at 14.7 Hz and 48.8 Hz where their modal shapes are similar, corresponding to the first and fourth eigenmodes at the simplified mechanical model. Besides, the modal shapes of dummy painting B at 35.5 Hz and 115.9 Hz are also similar to those of dummy painting A at 36.1 Hz and 112.2 Hz. There are many commonalities between the two paintings. Therefore, it is reasonable to assume that the securing method used in dummy painting C does not have a significant effect on the modal characteristics of paintings, at least less than the inhomogeneity.

To sum up, the experimental modal analysis reveals valuable information about the

unprimed dummy paintings, such as the weak response over the frequency range and the possible differences in modal characteristics. In addition, the simplified mechanical model or FE model are less informative for unprimed dummy paintings. However, further experiments and analyses are necessary to validate the above assumptions.

3.3.2.2 Primed Dummy Paintings

Primer were then applied to all unprimed dummy paintings to further investigate changes in their modal characteristics. For the sake of comparison, the dummy painting A is taken as an example again. Figure 3.11 shows the CMIF of primed dummy painting A obtained from the experimental modal analysis and highlights the identified eigenfrequencies. Obviously, after applying the primer, the composite material consisting of canvas and primer becomes stiffer, which yields much more pronounced peaks with much larger absolute values. As a result, the signal-to-noise ratio is higher, and the noise becomes almost invisible, making it much easier to excite and identify the eigenfrequencies. In total, about 27 eigenfrequencies were identified in the frequency range up to 120 Hz, most of them appearing in the first CMIF. These features are similar to those of the unprimed dummy painting. It is important to note that after the application of the primer, the dummy painting becomes sensitive to changes in temperature and humidity. Even in a climate box, small fluctuations can cause significant changes in the eigenfrequencies, as will be explained in detail in Section 3.4. As a result, smaller secondary peaks are observed near some of the dominant peaks in the CMIF curve. In order to distinguish them, it is necessary to combine the mode shapes.

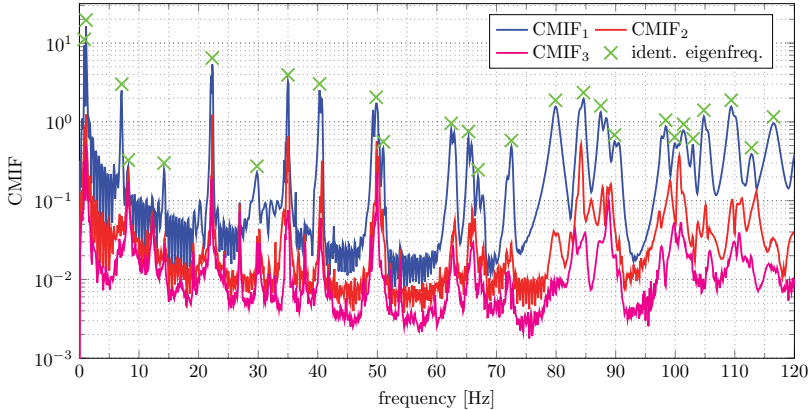


Figure 3.11: CMIF of primed dummy painting A with identified eigenfrequency locations.

Similarly to the unprimed dummy painting A, in the low frequency range up to 20 Hz, due to the soft suspension, the eigenfrequencies related to rigid body modes can also be

found. The first eigenfrequency of primed dummy painting A is identified at 22.3 Hz. It is relatively far away from the rigid body modes, which means that the suspension is soft enough for the influence of the rigid body modes to be neglected. A small residues of the rubber bands suspension can be observed by small peaks at 29.8 Hz. This peak is very small compared to the structural modal peaks of the primed canvas. Furthermore, this peak is always between the first and the second eigenmodes, hence, even though it appears, it does not affect the structural modes of the primed canvas. Nevertheless, they are still identified in the subsequent parameter identification and modal reconstruction process.

Since the structural modes become clearly distinguishable, the advantages of the SVD-based method can be emphasized here when several peaks are very close to each other, e.g., the sixth and seventh eigenfrequencies. Due to the projection of the singular vectors, these close peaks can be identified without being affected by their neighbors as long as the measurement frequency resolution is high enough. Figure 3.12 shows an example of mobility around the sixth and seventh eigenfrequencies as well as the EFRFs for these two eigenfrequencies. It is clear that the EFRFs divide the two eigenfrequencies into two curves quite nicely, which makes parameter identification using the EFRFs much easier than using the mobility directly. Consequently, a reliable and systematic parameter identification can be performed for these close eigenmodes.

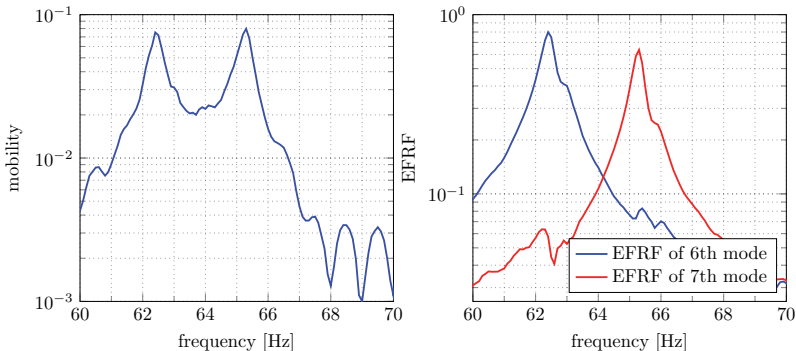


Figure 3.12: One exemplary mobility (left) and the EFRFs corresponding to the eigenmodes (right).

When detailing identified parameters, comparing the measured and reconstructed mobilities remains the first priority to assess the quality of the identified modal parameters. Thus, in Fig. 3.13, the measured and reconstructed mobilities of an input-output combination are compared to each other in magnitude and phase as an example. The quality of parameter identification is significantly improved compared to unprimed dummy paintings. The reconstructed mobilities approximate the measurements remarkably well in magnitude and

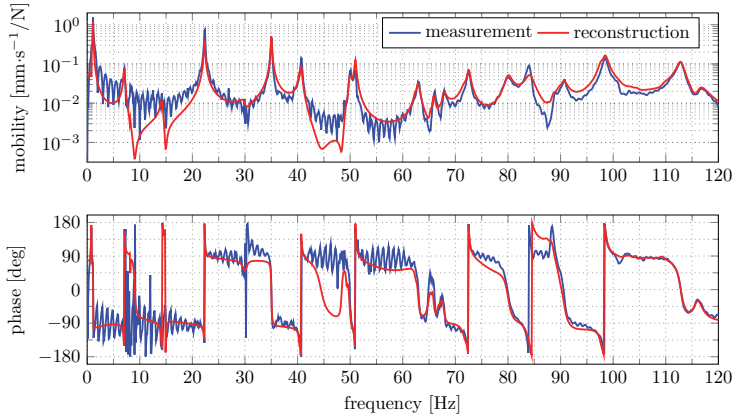


Figure 3.13: Amplitude (top) and phase (bottom) of a mobility excited in the bottom center and measured in the middle for primed dummy painting A.

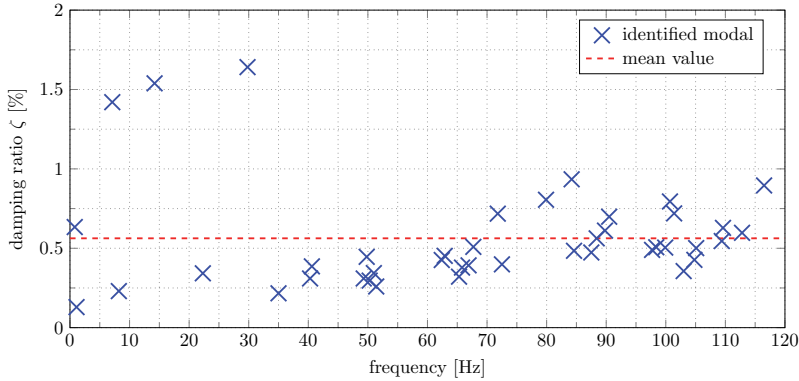


Figure 3.14: Identified modal damping ratios for primed dummy painting A and their mean value.

phase in the frequency range up to 120 Hz, indicating a successful parameter identification. Afterwards, the identified modal damping ratios ζ_r of primed dummy painting A presented in Fig. 3.14 shall be discussed. Disregarding the damping ratio associated with the rigid body modes, it can be observed that the damping ratios of the eigenmodes are all less than 1 % and the average damping ratio is around 0.56 %. They are much smaller than that of the unprimed dummy paintings, which is another reason why the modal parameters of the dummy paintings become easier to identify after the application of the primer. Moreover,

the first eight identified mode shapes of primed dummy painting A are illustrated with their corresponding eigenfrequencies in Fig. 3.15. Different from unprimed dummy paintings, and benefiting from the clearly identifiable eigenmodes, it is possible to label the order of each mode for primed dummy paintings. In general, the mode shapes of primed dummy painting A are similar to those of the simplified mechanical model. But some eigenmodes are distorted, such as the modes at 49.8 Hz, 51 Hz and 65.3 Hz. These distorted eigenmodes are probably caused by inhomogeneous distribution of tension and density, which can be supported by the FE model. In particular, compared with the simplified mechanical model, the fourth and fifth eigenmodes have been reversed. This may be because their eigenfrequencies are quite close, and slightly unevenly distributed tension or density has changed their order.

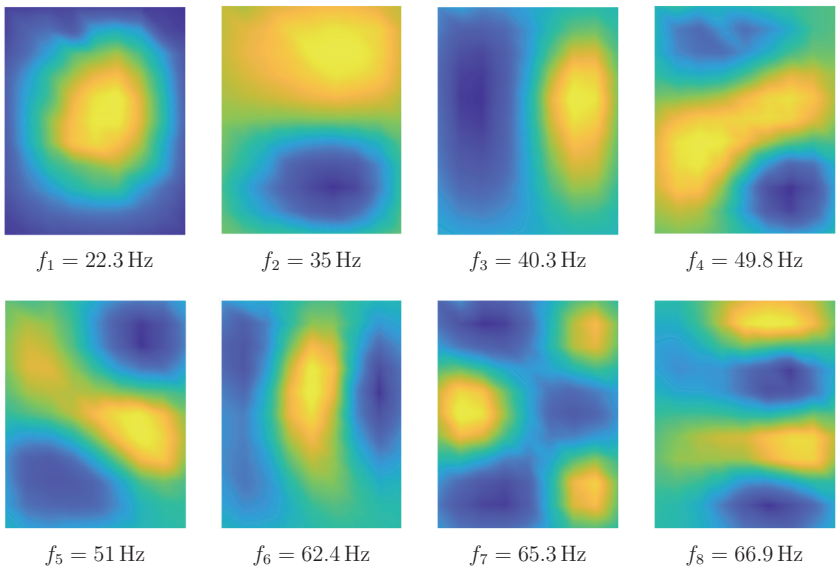


Figure 3.15: The first eight identified eigenmodes obtained from the experimental modal analysis for primed dummy painting A.

For primed dummy paintings, the most important point that shall be discussed is the similarities and differences in the modal characteristics of the investigated dummy paintings after applying the primer. To avoid redundancy, the experimental modal analysis results for primed dummy paintings B and C are attached in Appendices A.3 and A.4, respectively. All dummy paintings become stiffer after the application of the primer, and the canvas vibration produced by the excitation is enhanced, hence the signal-to-noise ratio is improved,

which leads to a much higher quality of modal parameter identification. Also, the influence of the strainer on the eigenmodes of the canvas becomes invisible. All three primed dummy paintings are densely distributed with many eigenfrequencies (21 in dummy painting A, 16 in dummy painting B and 20 in dummy painting C) in the evaluated frequency up to 120 Hz. The damping ratios of the vast majority of eigenmodes are less than 0.5 %, which also reduces the difficulty of identifying the modal parameters. Analyzing the first eight mode shapes of the three primed dummy paintings, it can be found that they are similar to those of the simplified mechanical model, but all of them are more or less distorted by the influence of inhomogeneity, and when the eigenfrequencies of two eigenmodes are close to each other, their order may be reversed due to inhomogeneity.

The primed dummy painting B possesses a tilted canvas and its eigenfrequencies are higher than those of the primed dummy painting A. This suggests that the dummy painting B either has a bigger tension or a smaller density. The former may be explained by variations in the tension during the stretching process, the later may be explained by variations in the thickness of the primer due to variations in the application process. However, both were carefully carried out by experienced conservators and thus were carried out with high precision. The differences in the dynamic behavior, i.e., the eigenfrequencies, must thus be assumed to be within the general variance. Moreover, starting from the seventh eigenmode, the mode shapes of primed dummy painting B become severely distorted, which is probably caused by the tilted canvas. On the other hand, unlike the dummy painting A, dummy painting C uses nails to secure the canvas. The experimental modal analysis of primed dummy painting C shows a slightly higher eigenfrequencies than that of primed dummy painting A. It also suffers from reversed modal orders and distorted mode shapes. Although the mode shapes of primed dummy painting C is more regular, these differences are most probably attributable to inhomogeneity. That is, no significant differences in modal characteristics are found for another securing method.

Besides, comparing the experimental modal analysis results of the primed dummy paintings with the simplified mechanical model allows the quality of the model to be assessed. The first eight eigenfrequencies identified for three primed dummy paintings are listed in Table 3.1, as well as the eigenfrequencies of the corresponding simplified mechanical model. Because the values for the tension and density are unknown, in order to solve for the eigenfrequencies, the constant c^2 in Equation (3.17) is chosen such that the first eigenfrequency of the simplified mechanical model matches the first identified eigenfrequency of the primed dummy paintings. The data indicate that the eigenfrequencies of the three primed dummy paintings are higher than what the corresponding simplified mechanical model predicts. The higher the modal order, the greater the difference, and usually the simplified mechanical models can only predict the first three eigenfrequencies accurately. This is probably caused by the small bending stiffness in the primed canvas. Although the simplified mechanical model cannot provide accurate eigenfrequencies, the distribution tendency of the eigenfrequencies for the primed dummy painting remains similar to that of

the simplified mechanical model. Moreover, the simplified mechanical model still provides the valuable reference for the most regular mode shape.

In conclusion, a large amount of valuable information, such as the distribution of eigenfrequencies and damping ratios, and the distortion of mode shapes, have been obtained from the comparative analyses on the modal characteristics of several unprimed and primed dummy paintings. As well, the simplified mechanical model is an important reference for primed dummy painting. They will help to understand the modal characteristics of real paintings.

Table 3.1: The first eight eigenfrequencies of the primed dummy paintings and the corresponding simplified mechanical model.

| mode r | 1 | 2 | 3 | 4 | 5 | 6 | 7 | 8 |
|----------------------------|----------|----------|----------|----------|----------|----------|----------|----------|
| dummy painting A [Hz] | 22.3 | 35 | 40.3 | 49.8 | 51 | 62.4 | 65.3 | 66.9 |
| membrane ¹ [Hz] | 22.3 | 33.3 | 37.1 | 44.6 | 46.1 | 53.3 | 54.8 | 58.8 |
| dummy painting B [Hz] | 29.6 | 47.7 | 51.1 | 63.3 | 71.4 | 76.8 | 81.2 | 84.3 |
| membrane ² [Hz] | 29.6 | 44.2 | 49.3 | 59.2 | 61.2 | 70.8 | 72.8 | 78.0 |
| dummy painting C [Hz] | 25.5 | 41 | 44.8 | 55.8 | 60.5 | 67.8 | 73.4 | 77.3 |
| membrane ³ [Hz] | 25.5 | 38.1 | 42.4 | 51.0 | 52.7 | 61.0 | 62.7 | 67.2 |

¹simplified mechanical model with the same first eigenfrequency as the primed dummy painting A

²simplified mechanical model with the same first eigenfrequency as the primed dummy painting B

³simplified mechanical model with the same first eigenfrequency as the primed dummy painting C

3.3.2.3 Real Paintings

Real paintings have a wide variety of structures and materials, and compared with the dummy paintings studied in the previous section, there is an additional factor of aging which is difficult to quantify. Therefore, in this thesis, only two real paintings, the painting still life and the painting landscape, are subjected to experimental modal analysis in order to summarize their general modal characteristics. The first example is the painting still life, whose CMIF curves are calculated from the FRF matrix in the frequency range up to 100 Hz as depicted in Fig. 3.16. There are 43 identified eigenfrequencies highlighted in the first CMIF curve. The first eigenfrequency for the structural modes is identified at 9.7 Hz, and the peaks below this frequency are considered to be associated with the rigid body modes. This indicates that there are 40 structural modes distributed within 100 Hz alone, which is a much denser distribution than that in the dummy paintings. There is no secondary peak for a particular eigenmode found in the CMIF curves, suggesting that real paintings are at least less sensitive to climate than primed dummy paintings.

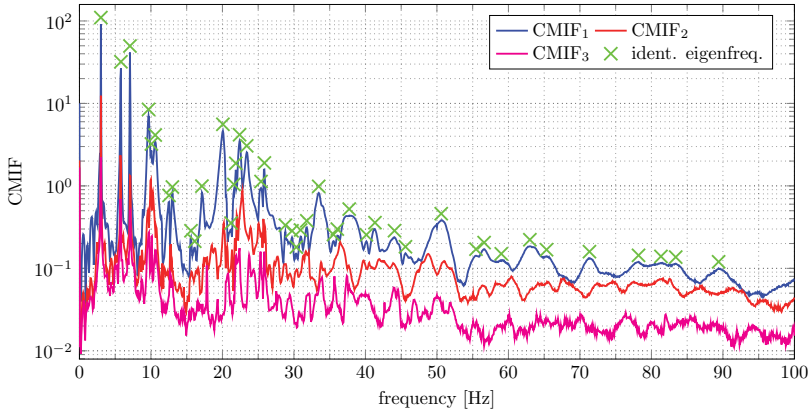


Figure 3.16: CMIF of painting still life with identified eigenfrequency locations.

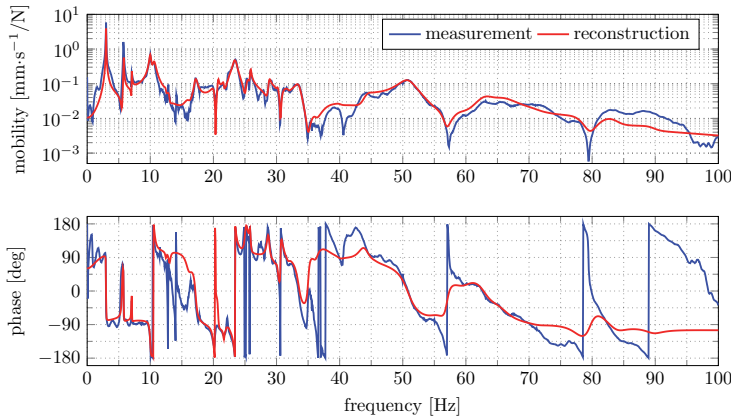


Figure 3.17: Amplitude (top) and phase (bottom) of a mobility excited in the bottom center and measured in the middle for painting still life.

Afterwards the quality of the modal parameter identification is examined. The measured and reconstructed mobilities for one input-output combination is used as an example in Fig. 3.17. Overall, the parameter identification maintains a high quality in the lower frequency band (< 50 Hz), but is not as good in the higher frequency band (> 50 Hz). It is probably due to the fact that in the lower frequency band the eigenmodes are less damped, hence the corresponding peaks are sharp and the parameter identification is less affected by noise, while the opposite is true in the higher frequency band. This assumption can be

supported by the identified modal damping ratios ζ , illustrated in Fig. 3.18. The average damping ratio of the paintings still life is lower than that of the unprimed dummy paintings, but higher than that of the primed dummy paintings, which leads to an in-between quality of the modal parameter identification. Moreover, the first eight identified mode shapes of the painting still life are shown in Fig. 3.19. It is evident, that all the mode shapes are severely distorted and probably only the standard mode shapes corresponding to the first four eigenmodes can be found in the simplified mechanical model. The higher the order of the eigenmodes, the larger the distortion of the mode shapes.

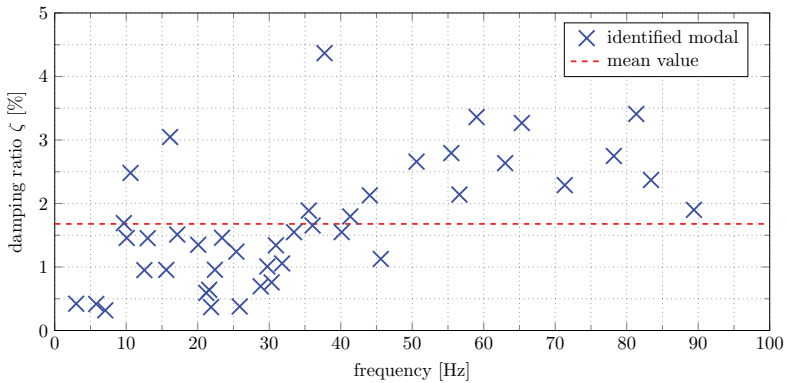


Figure 3.18: Identified modal damping ratios for painting still life and their mean value.

Furthermore, as a reference, the results of the experimental modal analysis on another real painting, i.e., the painting landscape, are attached in Appendix A.5. Combining the modal parameters of the two real paintings, their general modal characteristics can be summarized. First of all, their first eigenfrequencies are normally lower, this is because both the canvas and the paint layer are quite fragile after long term aging and art conservators do not use a larger tension to secure the canvas to the strainer to avoid further damage. Second, real paintings that are stiffer than unprimed dummy paintings but softer than primed dummy paintings respond to excitation with an intensity somewhere in between. This leads to smaller damping in the lower frequency bands and a higher quality of modal parameter identification, whereas the larger damping in the higher frequency bands and unsatisfactory modal parameter identification. At last, the various damages as well as inhomogeneities of real paintings due to aging make the distribution of eigenfrequencies very dense. The modal shapes are also distorted because of this. Usually only the first two or three mode shapes are relatively regular, i.e., they can be found corresponding standard shapes in the simplified mechanical model. Consequently, the simplified mechanical models can no longer provide any reference for real paintings in terms of the eigenfrequencies and

their distribution, as well as the mode shapes.

For short, despite the wide variety of real painting structures and materials, by drawing on the results of the study on dummy paintings, some commonalities in their modal parameters are still obtained through experimental modal analysis, which can help to understand and analyze the dynamic characteristics of paintings during transport.

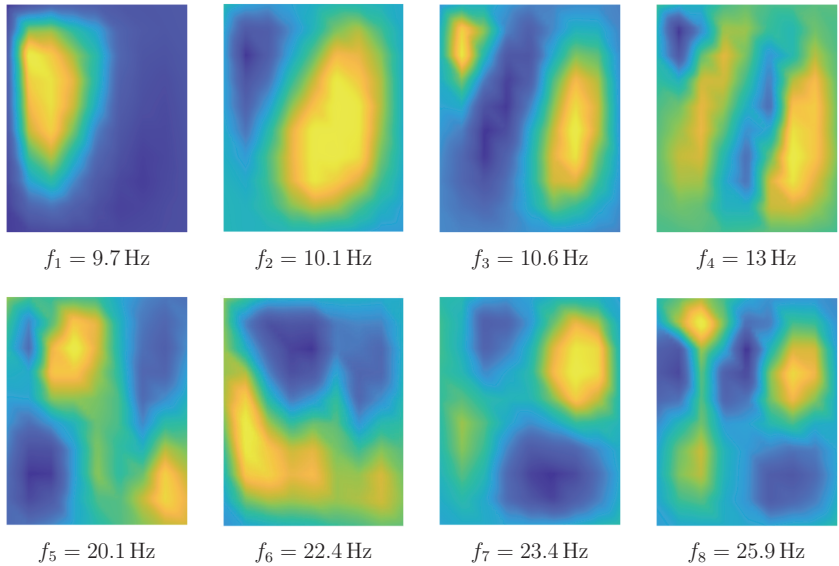


Figure 3.19: The first eight identified eigenmodes obtained from the experimental modal analysis for painting still life.

3.4 Climate Influence on Paintings

During the measurement for the experimental modal analysis, a sensitivity of the modal parameters with respect to fluctuations of humidity and temperature is observed. It is for this reason that all measurements were conducted in the climate box with highly stable climate. However, even small humidity and temperature fluctuations of only a few Kelvin or a few percent humidity can cause shifts of eigenfrequencies of several hertz. It is interesting and important to study the relationship between climate change and eigenfrequency change. If such a relationship would be known, measurements under changing climate could be compared and related. Measurements that need to be carried

out over a longer period of time, for example measurements with a sine sweep for all 99 points that take hours to complete, and where small changes in climate are unavoidable, could then be climate-compensated.

3.4.1 Experimental Setup and Measurements

In order to investigate the relationship between changing eigenfrequencies due to changing humidity and temperature, the eigenfrequencies are identified from the mobility of only one point using an automatic hammer excitation. Therefore, the experimental setup is the same as in Fig. 3.5. The excitation was performed continuously at the same reference point with the same time intervals, and the LDV always measured the response at the same point on the painting. Meanwhile, three InTemp CX450 Temp/Relative Humidity data loggers were used and placed around the investigated painting in order to record climate fluctuations inside the climate box. The desired humidity of the climate box was set to 55 %, but the temperature was left uncontrolled and was thus changing with the indoor laboratory environment. Then, the triplets consisting of humidity, temperature and eigenfrequency were interpolated to gain a relationship of climate versus eigenfrequency.

3.4.1.1 Unprimed Dummy Paintings

The influence of climate on the modal characteristics of paintings is first investigated on unprimed dummy paintings. The electromagnetic dynamic shaker excited the investigated painting with an impulse excitation every 5 minutes for more than 7 hours, resulting in 90 measurements. Taking the unprimed dummy painting B as an example, the mobilities obtained from each measurement are plotted as shown in Fig. 3.20. Considering that the eigenmodes of the unprimed dummy paintings are susceptible to noise interference, the evaluation in Fig. 3.20 is performed only in two short frequency bands with pronounced peaks. Some of the mobility curves have large deviations which tend to occur near the antiresonance point and are, therefore, considered to be due to noise. This is because the hammer signal is stable and reliable in the evaluated frequency band, whereas the response signal is usually weaker near the antiresonance point and is more affected by noise. Besides this, the mobility curves show that the results of each hammer experiment are highly reproducible. Both the peaks and the frequencies corresponding to the peaks are very stable. Therefore, if the influence of noise is taken into account, the eigenfrequencies of the unprimed dummy paintings are probably not affected by climate.

To further validate this opinion, the least-squares peak fitting method is used here again to extract the eigenfrequencies from every mobility. The identified eigenfrequencies are compared with the fluctuations in temperature and humidity. For example, the changes of the eigenfrequency around 11.4 Hz for unprimed dummy painting B and the fluctuations

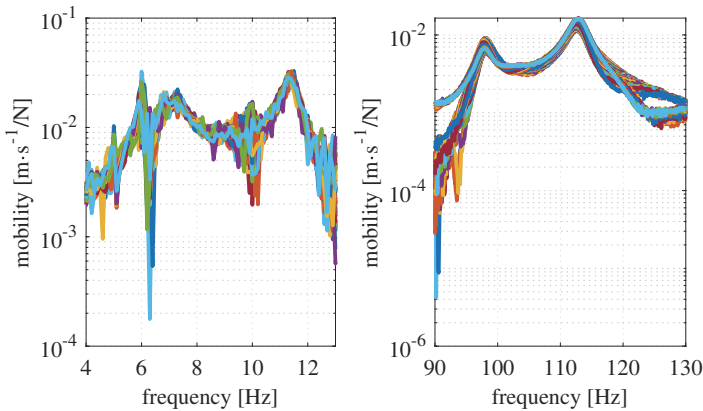


Figure 3.20: The mobilities in two different frequency bands obtained from 90 consecutive hammer experiments for unprimed dummy painting B.

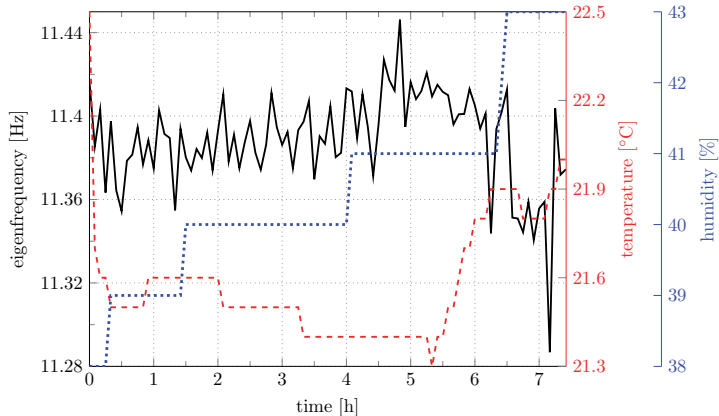


Figure 3.21: The relationship between an eigenfrequency (solid line), humidity (dotted line) and temperature (dashed line) for the unprimed dummy painting B.

of climate during the measurement are illustrated in Fig 3.21. The temperature fluctuates by 1.2°C and the relative humidity fluctuates by 5 % during the measurement, while the eigenfrequency only changes by 0.16 Hz and shows an overall stable trend. The analysis of the other eigenfrequencies as well as the analysis of the other unprimed dummy paintings present the similar results. Therefore, it is reasonable to assume that the fluctuations in climate have no influence on the modal parameters of the unprimed dummy paintings or

that their modal parameters are not sensitive to the fluctuations in climate, which will be further confirmed after the application of the primer.

3.4.1.2 Primed Dummy Paintings

The next investigation is whether the modal characteristics of primed dummy paintings are influenced by changing climate. The experiment still maintained the excitation provided by the electrodynamic shaker every 5 minutes, but the length of the experiment was extended to 14 hours. Hence, 168 measurements were obtained for each experiment. Again taking the dummy painting B as an example, after applying the primer, the mobility curves obtained from each measurement during climate fluctuations are shown in Fig. 3.22. Similarly, in order to present the results more clearly, two short frequency bands have been chosen to evaluate in Fig. 3.22. A dummy painting with primer has a higher signal-to-noise ratio and therefore do not show mobility curves with large deviations. However, it can be seen obviously from the mobility curves that eigenfrequencies of the primed dummy painting B are shifted, while the peak values of eigenfrequencies are relatively stable. For experiments on other primed dummy paintings similar phenomena have also been found. This suggests that the eigenfrequencies of primed dummy paintings must be affected by climate fluctuations.

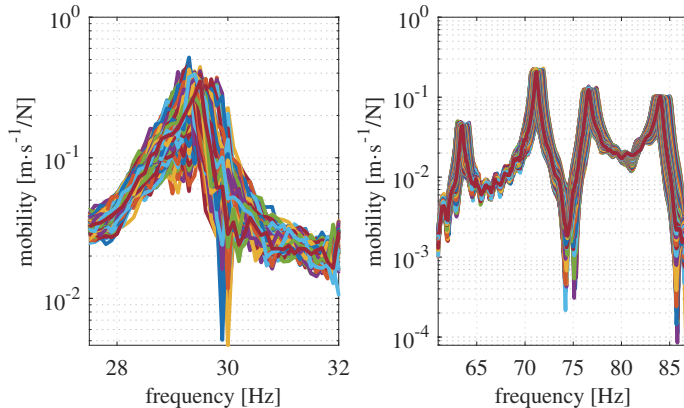


Figure 3.22: The mobilities in two different frequency bands obtained from 168 consecutive hammer experiments for primed dummy painting B.

Furthermore, the eigenfrequencies of the primed dummy painting are extracted by the modal parameter identification method. The fluctuations of its first eigenfrequencies and climate for one experiment are plotted in Fig. 3.23. During this experiment, the temperature fluctuates by 2.2°C , the relative humidity fluctuates by 1.32 %, and the

eigenfrequency fluctuates by 0.64 Hz. Climate fluctuations are smaller than when the primer is not applied, but the eigenfrequency changes are much larger. In addition, it can be inferred from Fig. 3.23 that the eigenfrequency is negatively correlated with both temperature and humidity. This may be due to fluctuations in temperature and humidity causing moisture absorption and desorption from the primer layer, which in turn causes changes in the mass of the painting. The higher the mass, the lower the eigenfrequency and vice versa. The modal characteristics of unprimed dummy paintings are insensitive to climate fluctuations. Therefore, it is the primer layer that causes the modal characteristics of primed dummy paintings to be affected by humidity and temperature.

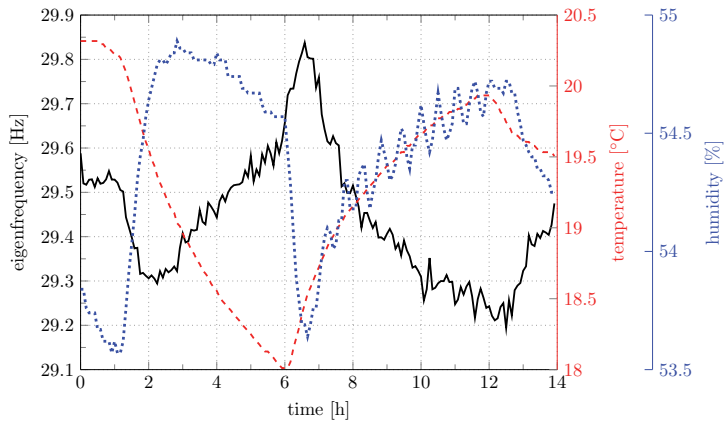


Figure 3.23: The relationship between an eigenfrequency (solid line), humidity (dotted line) and temperature (dashed line) for the primed dummy painting B.

3.4.1.3 Real Paintings

It remains to be investigated whether the modal characteristics of real paintings are also affected by climatic fluctuations. The same experimental setup was used to conduct experiments on the painting landscape, and the experiment duration is 12 hours. Consequently, the 144 mobility curves obtained from one experiment are shown in Fig. 3.24. For the sake of convenience, still only the eigenfrequencies in two short frequency bands are selected for evaluation. Despite the small climate fluctuations at the time of this experiment, shifts in each eigenfrequency are still observed. In addition, different from the primed dummy paintings, the peaks of the eigenfrequencies are also affected by changing climate. This may be an additional effect of long-term aging. However, the variation of the peak values varies with different eigenfrequencies, which is not investigated in depth in this thesis.

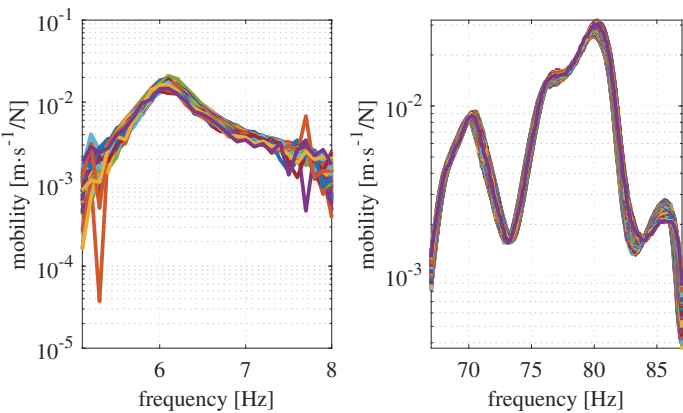


Figure 3.24: The mobilities in two different frequency bands obtained from 144 consecutive hammer experiments for painting landscape.

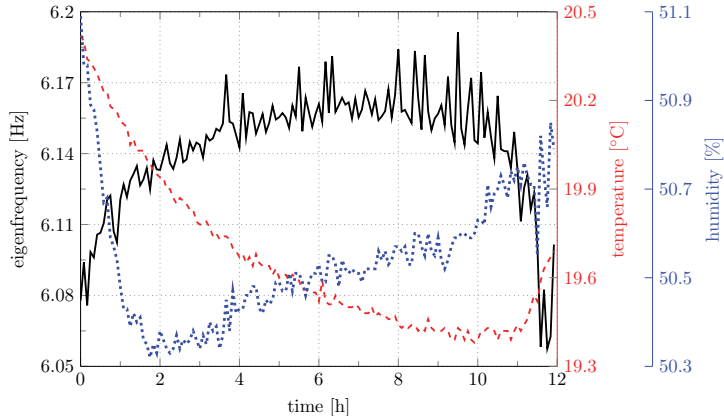


Figure 3.25: The relationship between an eigenfrequency (solid line), humidity (dotted line) and temperature (dashed line) for the painting landscape.

Then, the eigenfrequencies of the real painting in Fig. 3.24 are extracted and the first eigenfrequencies as well as the fluctuation curves of temperature and humidity are plotted in Fig. 3.25. As can be seen from this figure, the temperature fluctuates by 1.04°C , the relative humidity fluctuates by 0.77%, and the eigenfrequency fluctuates by 0.14 Hz. Since the fluctuations in climate are relatively small, the observed changes in eigenfrequency are also small. However, the negative correlations between eigenfrequency and temperature

and humidity is quite pronounced. Combined with the experimental results of primer dummy paintings, this further confirms that changes in eigenfrequency are negatively correlated with changes in climate.

3.4.2 Linearization and Eigenfrequency Compensation

The packaging box of painting is generally designed to keep humidity and temperature as stable as possible, i.e., the humidity and temperature in the packaging box only fluctuate in a small range. As shown in Fig. 3.26, the results of multiple experiments conducted on the primed dummy painting B have shown that eigenfrequency approximates a linear relationship with humidity and temperature over a small range. Therefore, in a small range of humidity and temperature, it is feasible to establish a linear relationship between eigenfrequency, humidity and temperature.

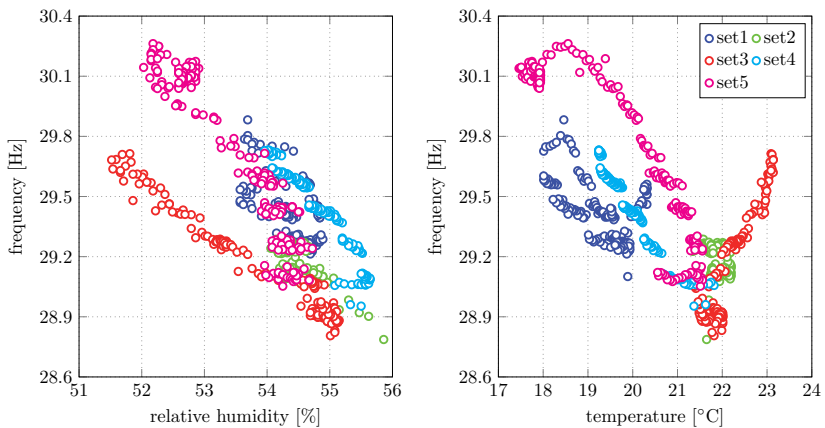


Figure 3.26: Five sets of measurement results between eigenfrequency, humidity, and temperature.

Given that for both dummy paintings and real paintings, the linear relationship between their eigenfrequencies and temperature and humidity varies from painting to painting, only the primed dummy painting B is used here as an example to describe the procedure for establishing the linear relationship. The following objective function is used to fit the first eight eigenfrequencies of the primed dummy painting B

$$f_r(H, T) = p_0 + p_H H + p_T T, \quad (3.18)$$

where f_r is the r -th eigenfrequency, H is relative humidity, T is temperature, and p_0 , p_H , p_T are fitting parameters of the two dimensional linear function. At the same time, in

order to evaluate the accuracy of linear fitting, the coefficient of determination is adopted

$$R^2 = 1 - \frac{\sum_i(y_i - f_i)^2}{\sum_i(y_i - \bar{y})^2}, \quad (3.19)$$

where y_i is the measured value, f_i is the fitted value and \bar{y} is the mean value of the measured data. The R^2 value is a statistic quantity that gives some information about the quality of the model fit, based on the proportion of total variation of outcomes explained by the model [DraperSmith98]. The closer R^2 is to 1, the better the fitting results.

The results of linear fitting using a least square fitting are listed in Table 3.2. The lowest R^2 in the fitting results is 0.825 and the highest can reach 0.961, which indicates that the linear fitting obtains a good result. Therefore, these fitting parameters can be used for eigenfrequency compensation.

Table 3.2: Linear fitting parameters of the relationship between the first eight eigenfrequencies of the dummy painting B, humidity, and temperature.

| mode r | 1 | 2 | 3 | 4 | 5 | 6 | 7 | 8 |
|--------|--------|--------|--------|--------|--------|--------|--------|--------|
| p_0 | 45.41 | 72.37 | 75.86 | 63.40 | 71.00 | 76.40 | 84.10 | 97.10 |
| p_H | -0.241 | -0.378 | -0.371 | -0.468 | -0.520 | -0.509 | -0.643 | -0.668 |
| p_T | -0.144 | -0.204 | -0.243 | -0.311 | -0.281 | -0.350 | -0.415 | -0.368 |
| R^2 | 0.892 | 0.851 | 0.961 | 0.863 | 0.892 | 0.955 | 0.825 | 0.892 |

The purpose of eigenfrequency compensation is when changing eigenfrequencies are caused by inevitable changing climate, the disturbed eigenfrequency can be compensated to the corresponding eigenfrequency under a reference climate. For example, when taking a measurement that lasts for several hours, the humidity and temperature in the climate box inevitably fluctuate, which causes the measured eigenfrequencies of the canvas to fluctuate. The fluctuating eigenfrequencies will increase the difficulty of interpreting the results. However, a reference climate can be selected, and the theoretical value of eigenfrequency f_{ref} under this climate condition can be obtained by Eq. (3.18). The theoretical value of the eigenfrequency under a changing climate f_r is also calculated by Eq. (3.18). Then, the difference between the reference eigenfrequency f_{ref} and the theoretical eigenfrequency f_r is compensated by the measured eigenfrequency f_m . Finally, the compensated eigenfrequency \hat{f}_m can be obtained, namely

$$\hat{f}_m = f_m + f_{ref} - f_r. \quad (3.20)$$

The quality of the compensation depends on the quality of the fitting. The better the fitting result, the smaller the deviation of the compensation result. For example, the measurement results in Fig. 3.26 are compensated to the eigenfrequencies when the relative humidity is 55% and the temperature is 22°C, which is the climate condition in the experimental modal analysis. The compensation results of the eigenfrequencies are shown

in the Fig. 3.27. The maximum deviation of the compensation results is 0.265 Hz, which is much smaller than the differences seen in Fig. 3.26. Although there are still deviations caused by the measurement procedure, these are much smaller than the fluctuations caused by changing climate.

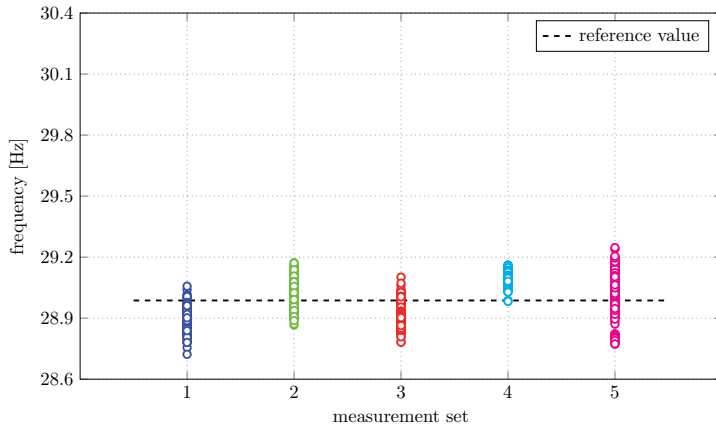


Figure 3.27: Compensation values of five sets of measurement results under a relative humidity of 55% and a temperature of 22°C.

Chapter 4

Simulation of Transport-induced Vibration

Exploring the modal characteristics has provided deeper insights into the dynamic behavior of paintings. However, accurately replicating the state of the painting during transport in a laboratory setting remains challenging. The different boundary conditions lead to variations in the modal parameters of the painting in the laboratory and during transport. Moreover, the precise magnitude and location of the excitation applied to the painting during transport are often unknown. Consequently, it is very difficult to predict the vibration experienced by the painting during transport based solely on the modal model identified in the laboratory. Nevertheless, knowing these vibration holds great significance for art conservators. By monitoring the motion of the painting during transport, they try to define safety limits of shock and vibration for the painting [Michalski91, Marcon91b, Saunders98, LasykEtAl08], predict the damage of the painting [TsiranidouEtAl11, TsiranidouEtAl13, TornariTsiranidouBernikola14], or evaluate the vibration isolation performance of the packaging system [Marcon91a, BäschlinEtAl11, LäuchliEtAl14]. Combined with the dynamic behavior of the painting [Kracht11, ChiribogaArroyo13, Hartlieb21, GaoEtAl23b], art conservators can also improve the packaging systems to prevent the eigenmodes of the painting from being excited, and avoid irreversible damage [Caldicott91, Green91, KrachtKletschkowski17, Marcon91a]. Therefore, how to effectively monitor the response of the painting to shock and vibration excitation during transport is of particular importance.

Constrained, among others, by the cramped design of packaging cases, it is difficult to directly monitor the painting vibration during transport, as the equipment required is generally too bulky to be included alongside the painting in a standard packing case. Attaching sensors to the canvas is in any case unacceptable and dangerous. Furthermore, the lack of an inertial reference makes contactless measurements very difficult. In [LasykEtAl08], an advanced small laser displacement sensor was used, but it was found that the fixture of

the sensor may possibly change the dynamic behaviors of the crate and severely limits the value of the collected information. A common practice is, to use accelerometers attached to the strainer [Caldicott91, Palmbach07, Gmach10, Kracht11, HeinemannEtAl19]. These accelerometers capture the response of the strainer to shock and vibration excitation during transport, which assists art conservators to make predictions, evaluations, and improvements. However, the response of the canvas itself is always unknown and practically impossible to monitor. If more accurate information about the vibration response or vibration level of the canvas during transport would be known, it would allow to optimize the transport conditions and develop measures to further protect the painting. Based on this motivation, this thesis proposes to simulate in the laboratory the canvas vibration during transport with high accuracy. Then, the canvas vibration can be conveniently observed in a controlled environment with respect to an inertial reference. It would serve as a reference for the actual vibration of the canvas during transport, and contribute to perform advanced investigations which cannot be done during a real transport.

Given the fragility of the paint layer and considering that the application of sensors on the paint layers or canvases of original valuable paintings is prohibited from a conservatory perspective, few works directly monitored the response of the canvas to shock and vibration excitation during transport. Predicting the vibration of the painting during transport by establishing any type of model has moreover to the knowledge of the author never been addressed. Only little work has been attempted to reproduce in the laboratory the excitation to the painting during transport, so as to observe the response of the canvas. In [Caldicott91], a uniaxial electrohydraulic shaker applying random vibration to simulate the road excitation had been developed to test a painting in the laboratory. However, the random vibration can hardly represent the characteristics of shock and vibration excitation under different road conditions. There is also a big difference between the uniaxial random vibration of the painting produced by the shaker and its spatial vibration during transport. A transport simulator with linear movement along a single axis was designed in [Palmbach07], which allows performing the simulation sequentially along each axis of the painting to reproduce the vibration of each degree of freedom acquired by the acceleration sensors during transport. Combined with some advanced measurement techniques, this simulator has made contributions to the evaluation on the painting transport conditions [TsiranidouEtAl11, TsiranidouEtAl13, TornariTsiranidouBernikola14, BäschlinEtAl11]. However, this simulator is still only capable of single axis movement. It was also stated in [Palmbach07] that the vibration reproduction accuracy of the simulator is not ideal. Therefore, in this thesis, multi-dimensional vibration directly related to the damage will be simulated with high accuracy based on the data collected by accelerometers applied on the strainer during transport.

Addressing the above issue, this thesis will present two novel approaches. A real painting transport experiment is initially conducted to provide reference data. Since the vibration of the strainer can be measured during transport with accelerometers, in the laboratory,

the assembly including the investigated painting, sensors and the hanging systems are kept in the same state as for a real transport, so as to avoid changes in the modal characteristics of the painting. The basic idea of the first approach is to reproduce the vibration on the strainer. Four electrodynamical shakers are connected to this assembly as actuators to excite the vibration of the strainer. A real-time simulation platform implementing a multi-channel active vibration control algorithm drives all actuators simultaneously and reproduces the vibration of the strainer obtained from the real transport experiment. Consequently, the vibration at arbitrary points on the canvas can be measured in the laboratory by a Laser Doppler Vibrometer (LDV) without contact, since an inertial reference is available in the laboratory. Then, an advanced analysis of transport-induced vibration is possible. Compared to this approach, the second approach is a more accessible and efficient alternative. Its main objective is, to develop a numerical model in the laboratory setting that describes the relationship between the vibration on the strainer and the vibration at an arbitrary point on the canvas. The numerical modeling relies on impulse hammer experiments. The optimal excitation points and positions are determined through comprehensive experiments. Based on the optimized numerical model and the strainer vibration collected from the real transport experiment, the vibration at an arbitrary point on the canvas can be reconstructed.

This chapter presents two innovative approaches to simulate the transport-induced vibration of the painting. The modal characteristics presented in Chapter 3 serves as a reference for setting the simulation parameters. Sections 4.1 includes the theoretical background of some active vibration control algorithms used. Then, detailed information is given in Section 4.2 about a real transport experiment used to provide the reference data on the painting. Section 4.3 applies the first approach to reproduce the canvas vibration. The experimental setup, control algorithm, and experimental results are stated step by step in this section. Subsequently, the second approach aimed at reconstructing the canvas vibration is introduced in Section 4.4, including numerical modeling, experimental setup, and numerical analysis.

4.1 Theoretical Background of LMS Algorithm

The challenge of simulating the canvas vibration during transport by reproducing the vibration on the strainer is to design a suitable controller. It is the purpose of this controller to move the painting using four electrodynamical shakers in the same way as it was measured in the crate during transport. The vibration reproduction controller in the simulation platform has to simultaneously control four actuators and reproduce the acceleration signals obtained from the real transport experiment with high accuracy. There are many algorithms that can be used to achieve this function. In the early stage of this research, a feedback controller based on an adaptive PID algorithm was tried,

but high-precision tracking could not be achieved. Besides a problem with integrator windup, long-term experiments revealed error propagation of the adaptive algorithm, which prohibited the use of this adaptive feedback control.

Instead, a feedforward controller was considered. The Filtered- x Least Mean Square (FxLMS) algorithm is a typical feedforward control algorithm in active noise control, based on the concepts of adaptive signal processing. It is derived from the Least Mean Square (LMS) algorithm, which is simple to implement, has a small amount of calculation, and has good robustness [HansenEtAl12]. The FxLMS algorithm achieved extremely good results in single-channel vibration reproduction. Therefore, an extension of this algorithm to multi-channel control is applied in order to realize the vibration reproduction of the investigated paintings. By way of prelude, the theoretical foundations of the LMS and the single-channel FxLMS algorithms are described in detail in this section.

4.1.1 Least Mean Square Algorithm

As a basis, the LMS algorithm implements a non-recursive, or finite impulse response (FIR) filter, which is probably the simplest and most commonly used architecture in adaptive digital signal processing. The typical direct realization of the FIR filter, known as the transversal filter or tapped delay line, is shown in Fig. 4.1 [HansenEtAl12]. While its performance may not be as good as that of an infinite impulse response filter with a given number of filter weights, its inherent stability and simple structure, which allows for adaptive tuning by relatively simple algorithms, tends to make it the most practical choice for digital signal processing.

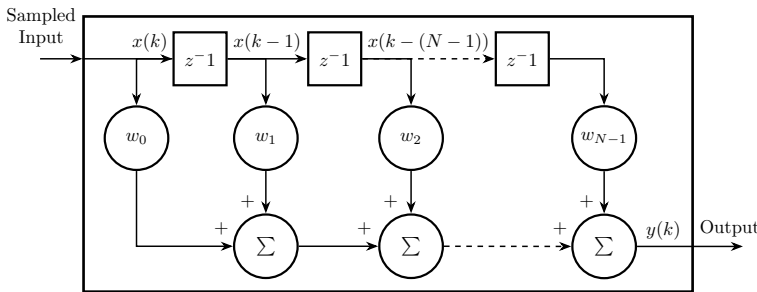


Figure 4.1: The structure of finite impulse response (FIR) filter.

At some sampling time k , the output $y(k)$ of the FIR filter is simply a weighted combination

of past input samples [HansenEtAl12]

$$y(k) = \sum_{n=0}^{N-1} w_n(k)x(k-n) = \mathbf{w}^T(k)\mathbf{x}(k) = \mathbf{x}^T(k)\mathbf{w}(k), \quad (4.1)$$

where there are N stages in the filter, \mathbf{w} is an $N \times 1$ vector of filter weight coefficients, given by

$$\mathbf{w}(k) = [w_0(k) \ w_1(k) \ \dots \ w_{N-1}(k)]^T, \quad (4.2)$$

\mathbf{x} is an $N \times 1$ vector of input samples in the delay chain of the filter, given by

$$\mathbf{x}(k) = [x(k) \ x(k-1) \ \dots \ x(k-(N-1))]^T, \quad (4.3)$$

and T denotes the transpose. The output $y(k)$ thus can also be described as a convolution of the input samples $\mathbf{x}(k)$ and filter weights $\mathbf{w}(k)$.

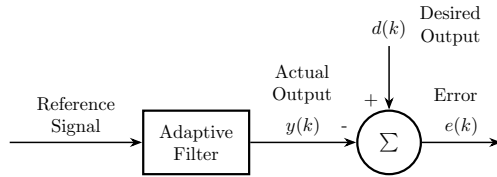


Figure 4.2: Standard adaptive filtering problem.

Consider the implementation of an FIR filter in the adaptive filtering problem shown in Fig. 4.2, where a reference signal is fed into the adaptive (FIR) filter with the aim of having the filter output match some desired output as closely as possible. The error signal $e(k)$ is defined as the difference between the desired signal $d(k)$ and the actual output signal $y(k)$ of the filter at sampling time k

$$e(k) = d(k) - y(k). \quad (4.4)$$

The ideal error criterion for such a problem is the mean square error ξ defined as the ensemble average, or expected value, of the squared value of the error signal $e(k)$

$$\xi(k) = E\{e^2(k)\}. \quad (4.5)$$

The mean square error is not the result of temporal averaging, but is rather the expected value, as denoted by the statistical expectation operator $E\{\cdot\}$ of the square of the error signal at any given instant in time. The mean square error in Equation (4.5) can be re-expressed by using Equations (4.1) and (4.4) as

$$\begin{aligned} \xi(k) &= E\{(d(k) - \mathbf{x}^T(k)\mathbf{w}(k))^2\} \\ &= E\{d^2(k)\} - 2E\{d(k)\mathbf{x}^T(k)\}\mathbf{w}(k) + \mathbf{w}^T E\{\mathbf{x}(k)\mathbf{x}^T(k)\}\mathbf{w}(k) \end{aligned} \quad (4.6)$$

with the assumption that the weight coefficient vector \mathbf{w} is uncorrelated with the input signal vector \mathbf{x} .

Solving Equation (4.6) directly to obtain a set of optimum weight coefficients is usually impractical due to a variety of problems [HansenEtAl12]. Instead, the optimum weight coefficient vector is found by some numerical search procedure. A simple gradient descent type algorithm is often implemented. This type of algorithm attempts to compute an optimum set of filter weights by adding to the present estimate of the optimum weight coefficient vector a partial negative gradient of the error surface at the location defined by this estimate. Mathematically, a generic gradient descent algorithm can be expressed as

$$\mathbf{w}(k+1) = \mathbf{w}(k) - \mu \Delta \mathbf{w}(k), \quad (4.7)$$

where $\Delta \mathbf{w}$ is the gradient of the error surface at the location given by the current weight coefficient vector, and μ is the partial negative gradient to be added, referred to as the convergence coefficient.

Returning to Equation (4.6), however, it is not practical to calculate these quantities in the equation in a practical application to obtain the deterministic gradient descent. Also, the system is rarely completely stationary, so these quantities must be recalculated over time. Therefore, some approximation must be found to avoid the limitations resulting from the need to use averaged quantities. An alternative approach is to approximate the mean square error at sampling time k , by the instantaneous error squared at sampling time k

$$\xi(k) \approx e^2(k) = (d(k) - \mathbf{w}^T(k)\mathbf{x}(k))^2. \quad (4.8)$$

Differentiating the value of instantaneous error squared with respect to the weight coefficient vector, the gradient estimate becomes

$$\Delta \mathbf{w}(k) \approx \frac{\partial e^2(k)}{\partial \mathbf{w}(k)} = -2e(k)\mathbf{x}(k). \quad (4.9)$$

Substituting this into the gradient descent algorithm format of Equation (4.7) yields the expression

$$\mathbf{w}(k+1) = \mathbf{w}(k) + 2\mu e(k)\mathbf{x}(k). \quad (4.10)$$

This is the least mean square, or LMS algorithm, attributed to [WidrowEtAl75]. To implement the algorithm and adjust the weights of the FIR filter, it is only necessary to know the value of the reference signal in the delay chain $\mathbf{x}(k)$ and the resultant error $e(k)$ when deriving the output using the current weights. For the LMS algorithm to converge in a stable manner towards the optimum solution, the convergence coefficient μ must be chosen appropriately. The bounds placed on the convergence coefficient for stable operation are [Diniz97]

$$0 < \mu < \frac{1}{\lambda_{\max}}, \quad (4.11)$$

where λ_{\max} is the largest eigenvalue of the input auto correlation matrix $E\{\mathbf{x}(k)\mathbf{x}^T(k)\}$.

The underlying LMS algorithm has a weakness in that it converges slowly. If one wishes to increase the convergence speed of the LMS algorithm, there exist a variety of solutions. The normalized LMS algorithm with a variable convergence is a typical solution and it usually converges faster than the LMS algorithm. It utilizes a variable convergence coefficient aiming at the minimization of the instantaneous output error [Bershad86, Diniz97]

$$\mu = \frac{1}{2\mathbf{x}^T(k)\mathbf{x}(k)}, \quad (4.12)$$

and hence, the updating equation for the LMS algorithm is given by

$$\mathbf{w}(k+1) = \mathbf{w}(k) + \frac{e(k)\mathbf{x}(k)}{\mathbf{x}^T(k)\mathbf{x}(k)}. \quad (4.13)$$

Similarly, other variants of the LMS algorithm, such as the variable step size LMS algorithm [ChanZerguineCowan03, AkhtarAbeKawamata06], the least mean p -power algorithm [WalachWidrow84, PeiTseng94], etc., all optimize the convergence speed of the LMS algorithm.

4.1.2 Single Channel Filtered- x LMS Algorithm

The adaptive filtering system implemented using the LMS algorithm is simple and robust, yet effective and, for all practical purposes, usually reasonably quick to converge to a near-optimal solution. This system is also the most common choice for active noise or vibration control system implementations. However, the form of the standard stochastic gradient descent (LMS) algorithm must be modified slightly to account for the significant delays that exist in the pathways between the control actuator output and the error sensor input to the controller. A block diagram of the single channel adaptive feedforward control arrangement [HansenEtAl12] which is a simple extension of the basic LMS algorithm is shown in Fig. 4.3.

The controller displayed in Fig. 4.3 is best suited in active control systems targeting single mode problems. This control system functions can be divided effectively into two parts: control signal derivation and filter weights adaptation. The task for the control system is the weights adaptation, such that the control signal derived by the FIR filter is in some sense optimal. To provide a basis for weights adaptation, the adaptive algorithm is provided with an 'error signal', a measure of the unwanted vibration or acoustic disturbance provided by some transducers in the system. The measurement provided by the error signal $e(k)$ is again the sum of the primary source generated disturbance $p(k)$ and the control source generated disturbance $s(k)$

$$e(k) = p(k) + s(k). \quad (4.14)$$

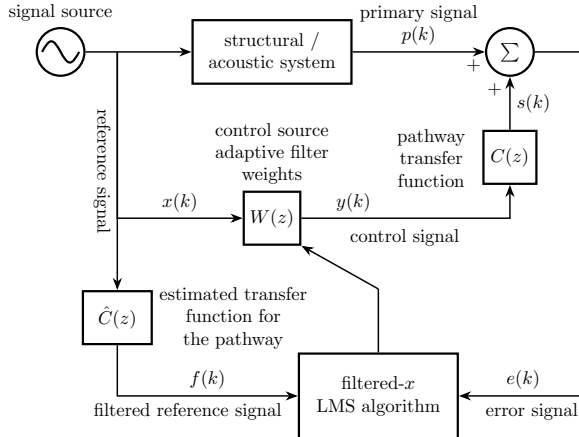


Figure 4.3: Block diagram of an adaptive single channel feedforward active control system.

The sign in Equation (4.14) is positive, as opposed to the negative used in electronic echo cancellation systems, because in an active noise or vibration control system transducers can only add signals arriving at their location. The control signal $y(k)$, the filter weight coefficients $\mathbf{w}(k)$ and the reference signal $x(k)$ are the same as defined in Eqs. (4.1–4.3). The feedforward control signal derived by the FIR control filter is not equal to the control source component $s(k)$ of the error signal. This is because the transducers (control sources and error sensors) used in an active noise and vibration control systems have characteristic frequency responses, or transfer functions. Also, there is an acoustic or structural transfer function between the point of application of the control disturbance and the location of the error sensor. These transfer functions often include a propagation delay.

All of the transfer functions between the control filter output and the error sensor output can be lumped into a single pathway transfer function. This transfer function can be modeled in the time domain as the m -order finite impulse response function

$$\mathbf{c} = [c_0 \ c_1 \ \dots \ c_{m-1}]^T. \quad (4.15)$$

The control source generated component $s(k)$ of the error signal is then equal to the convolution of the filter output $y(k)$ and this finite impulse response function

$$s(k) = \sum_{i=0}^{m-1} y(k-i)c_i = \mathbf{y}^T(k)\mathbf{c}, \quad (4.16)$$

where $\mathbf{y}(k)$ is an $m \times 1$ vector of present and past control filter outputs

$$\mathbf{y}(k) = [y(k) \ y(k-1) \ \dots \ y(k-m+1)]^T. \quad (4.17)$$

The quantity $\mathbf{y}(k)$ can be obtained by the matrix multiplication

$$\mathbf{y}(k) = \mathbf{X}^T(k)\mathbf{c}, \quad (4.18)$$

where $\mathbf{X}(k)$ is an $N \times m$ matrix of present and past reference signal vectors

$$\begin{aligned} \mathbf{X}(k) &= \begin{bmatrix} \mathbf{x}(k) & \mathbf{x}(k-1) & \dots & \mathbf{x}(k-m+1) \end{bmatrix} \\ &= \begin{bmatrix} x(k) & x(k-1) & \dots & x(k-m+1) \\ x(k-1) & x(k-2) & \dots & x(k-m) \\ \vdots & \vdots & \ddots & \vdots \\ x(k-N+1) & x(k-N+2) & \dots & x(k-m-N+2) \end{bmatrix}. \end{aligned} \quad (4.19)$$

The control source component of the error signal can now be re-expressed by substituting Equation (4.18) into Equation (4.16)

$$s(k) = [\mathbf{X}^T(k)\mathbf{w}]^T\mathbf{c} = \mathbf{w}^T\mathbf{X}^T(k)\mathbf{c} = \mathbf{w}^T\mathbf{f}(k) = \mathbf{f}^T(k)\mathbf{w}, \quad (4.20)$$

where $\mathbf{f}(k)$ is the 'filtered' reference signal vector

$$\mathbf{f}(k) = \mathbf{X}^T(k)\mathbf{c} = \begin{bmatrix} f(k) & f(k-1) & \dots & f(k-N+1) \end{bmatrix}^T. \quad (4.21)$$

Similar to the LMS algorithm, recall the gradient descent algorithm in Equation (4.7) and use the same assumption that in a practical implementation, the mean square error at sampling time k is approximated by the instantaneous error square at sampling time k . Differentiating this instantaneous error square at sampling time k with respect to the weight coefficient vector then gives

$$\Delta\mathbf{w}(k) \approx \frac{\partial e^2(k)}{\partial \mathbf{w}(k)} = 2e(k)\mathbf{f}(k). \quad (4.22)$$

Substituting Equation (4.22) into Equation (4.7), the gradient descent algorithm used for adapting the weights in the control source FIR filter is [HansenEtAl12]

$$\mathbf{w}(k+1) = \mathbf{w}(k) - 2\mu e(k)\mathbf{f}(k). \quad (4.23)$$

This is known as the single channel filtered- x LMS algorithm, which has appeared in various forms in the literature at various times [Morgan80, Burgess81].

It must be pointed out that, in the practical implementation of the algorithm in Equation (4.23), since the pathway transfer function \mathbf{c} is normally unknown, the filtered reference signal term $\mathbf{f}(k)$ is replaced by its estimate. The estimated filtered reference signal $\hat{\mathbf{f}}(k)$ is derived by convolving the reference signal vector $\mathbf{x}(k)$ with an estimated impulse response function model $\hat{\mathbf{c}}$ of the pathway transfer function in the time domain before being used in the adaptive algorithm. Therefore, the practical implementation of the algorithm is

$$\mathbf{w}(k+1) = \mathbf{w}(k) - 2\mu e(k)\hat{\mathbf{f}}(k). \quad (4.24)$$

The estimation of the pathway transfer function can be done easily by the LMS algorithm shown in Figs. 4.1 and 4.2. A random signal is fed as the reference signal to the active control system and the FIR filter, respectively. The error signal is the difference between the output of the active control system and the output of the FIR filter. The FIR filter weights are updated using the LMS algorithm to minimize the error criterion. When the algorithm converges, the FIR filter weights are the estimated pathway transfer function.

The estimates of the filtered reference signal vector used in Equation (4.24), in general, are inaccurate to some degree. This can be expected to have effect upon the stability of the filtered- x LMS algorithm in a practical system. For example, it has been demonstrated that for a sine wave input, the bounds placed on the convergence coefficient μ for algorithm stability are [SnyderHansen90]

$$0 < \mu < \frac{\cos(\varphi_h)}{\lambda_{\max} |h|}, \quad (4.25)$$

where h is the complex estimation error for the pathway transfer function, and φ_h is the phase change caused by the error in the transfer function. The larger the estimation error for the pathway transfer function, the smaller the bounds on the convergence coefficient. Even when the phase error exceeds 90° , there is no usable convergence coefficient and the active control system is unstable due to $\cos(\varphi_h) < 0$. This also reveals that it is possible to use the basic LMS algorithm directly in active control systems. However, the convergence coefficient must be chosen carefully, as well as the use of Lead-Lag compensator to ensure that the pathway phase is within 90° .

4.2 A Real Transport Experiment

The following sections will describe two approaches of simulating the transport-induced vibration of paintings in the laboratory, both of which require vibration data collected from a real transport experiment as a reference. Therefore, the setup and procedures of a real transport experiment is first presented in this section. Moreover, not all vibration on each degree of freedom of a painting plays a critical role in its potential damage, so it is necessary to extract the dominant vibration for subsequent research.

4.2.1 Experimental Procedure

The real painting 'landscape' was selected for a real transport experiment, see Section 2.2 for information about this painting. The real transport experiment was carried out in cooperation with hasenkamp Holding GmbH. They provided a proper packing case called Vario that has a flexible, shock-mounted and size-adjustable aluminum inner frame. With a Vario-system crate of high quality materials, paintings of various sizes can be transported with the best protection. The investigated painting was fixed in this packing case without

a protective backing using a patented hanging system, as shown in Fig. 4.4. This hanging system has a modular design and is perfectly adapted to the requirements of transport, installation and art storage. The overall portfolio ranges from simple protective packaging to shock-absorbing and fire-retardant climate boxes that guarantee constant temperature and humidity conditions inside the packing case. In addition, both strict conservational and ecological requirements are taken into account.

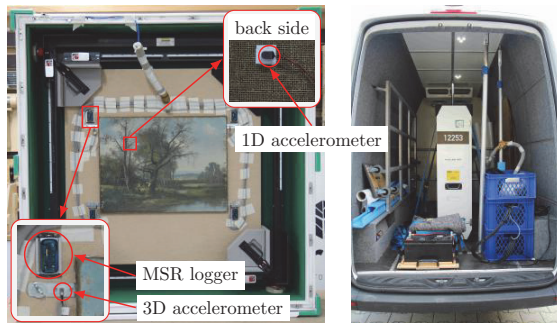


Figure 4.4: The experimental setup used for a real transport experiment of the investigated painting landscape.

Four three-dimensional accelerometers of model PCB-356A03/NC were attached to the hanging systems. The connection between the hanging systems and the strainer of the investigated painting is considered as rigid, while the strainer is also assumed to be a rigid body in this thesis. Therefore, the data collected by the four three-dimensional accelerometers is sufficient to represent the spatial vibration of the investigated painting during transport. A uniaxial accelerometer of model PCB-352A74 was attached to the canvas on the back of the investigated painting. This is only possible because this investigated painting is of negligible artistic value. The uniaxial accelerometer serves as a reference measurement of the otherwise indeterminable canvas motion during transport. Although these accelerometers have their own coordinate systems, they were all converted to the coordinate system defined in Section 2.3 when processing the data. Additionally, the temperature and the humidity inside the packing case were recorded using MSR165 data loggers. Then, the packed transport case was secured in the center of the transport vehicle with belts. The supporting data acquisition equipment and power supply facilities were also placed inside the vehicle. All packaging, handling as well as transport was carried out by professionally trained staff of hasenkamp, just as for any professional art transport. The transport experiment was carried out within the city of Cologne and lasted for one hour and the data was recorded with a time resolution of $\Delta t = 0.2\text{ ms}$. During the transport experiment, various street conditions such as highway, bad roads,

sudden braking manoeuvres, and waiting for traffic lights were experienced. The vibration data collected on the strainer and canvas, as well as the climate data, were used for the laboratory simulations in the following sections.

4.2.2 Simplified Vibration of a Painting During Transport

The general rigid body motion of the strainer consists of three independent translations and three independent rotations. This motion is transferred to the canvas via the strainer, which leads to the canvas motion in the painting plane as well as perpendicular to this plane. The damage to the paint layer is mainly caused by the canvas movement and the associated deformation of the paint layer. Due to a supporting effect provided by the tensile strength of the canvas, the movement in the painting plane leads to only very small stretches in the paint layer. In contrast, when the canvas moves perpendicularly to the painting plane, the canvas is flexible, so that there is only little supporting effect and a greater deformation, hence a damaging effect is to be expected [Sautter14]. This hypothesis needs to be clarified by additional research in the future with the fully operational laboratory test bed. Nevertheless, in this thesis, we limit ourselves to the simulation of the acceleration components perpendicular to the strainer, because only those excite the canvas motion, and consequently the paint layer motion, perpendicular to the painting plane. The considered strainer motion can be divided into three independent movements: a transnational movement in the transverse direction (z -axis), a rotational movement around the longitudinal axis (x -axis), and a rotational movement around the vertical axis (y -axis), as shown in Fig. 4.5. The translation in y - and x -direction and the rotation around the z -axis are not simulated in the laboratory setup.

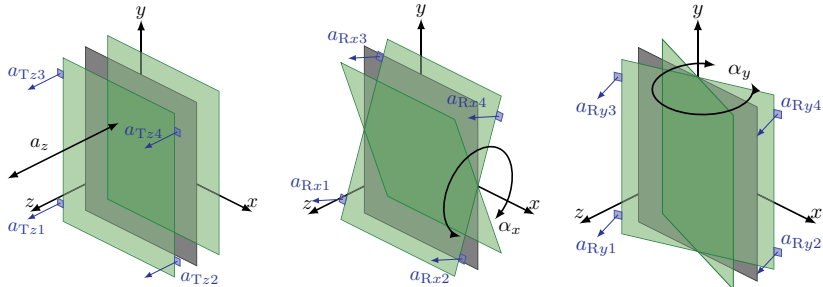


Figure 4.5: Rigid body movements of the strainer related to damage: transverse translation (left), rotation around longitudinal axis (middle) and rotation around vertical axis (right).

Obviously, the acceleration of the transverse translation of the strainer (\mathbf{a}_z) is fully captured by the components of the four accelerometers of the painting plane

$(\mathbf{a}_{Tzi}, i = 1, 2, 3, 4)$. The angular accelerations $\boldsymbol{\alpha}_x, \boldsymbol{\alpha}_y$ of the strainer rotating around the x -axis and the y -axis satisfy

$$\mathbf{a}_{Rxi} = \boldsymbol{\alpha}_x \times \mathbf{r}_i, \quad \mathbf{a}_{Ryi} = \boldsymbol{\alpha}_y \times \mathbf{r}_i, \quad i = 1, 2, 3, 4, \quad (4.26)$$

where \mathbf{r}_i is the position vector for each accelerometer, \mathbf{a}_{Rxi} and \mathbf{a}_{Ryi} are the components of the four accelerometers perpendicular to the painting plane and $\boldsymbol{\alpha}_x, \boldsymbol{\alpha}_y$ are angular accelerations. Because the positions of four accelerometers relative to the strainer are fixed, the angular accelerations $\boldsymbol{\alpha}_x, \boldsymbol{\alpha}_y$ of the strainer around the x -axis and y -axis according to Equation (4.26) are also fully captured by the components of the four accelerometers perpendicular to the painting plane. Furthermore, during transport the motion amplitude of the painting is assumed to be small in this thesis. The motion relationship between the individual degrees of freedom of the painting is completely linearized with independent rotations and not successive ones. Therefore, these three rigid body movements of the strainer are independent of each other, and, during the practical measurement, the component of each accelerometer perpendicular to the painting plane \mathbf{a}_{zi} satisfies

$$\mathbf{a}_{zi} = \mathbf{a}_{Tzi} + \mathbf{a}_{Rxi} + \mathbf{a}_{Ryi}, \quad i = 1, 2, 3, 4. \quad (4.27)$$

Thus, in summary, by tracking only the component of each accelerometer perpendicular to the painting plane, it is possible to reproduce the three movements of the painting that are particularly relevant to damage.

4.3 Reproduction of Transport-induced Vibration

The first approach proposed in this thesis to simulate the transport-induced vibration is to reproduce the vibration on the strainer by means of multi-channel active vibration control. With the assumption that the strainer is a rigid body, the vibration reproduced on the canvas can be representative of that during transport and can be conveniently measured in a controlled environment with respect to an inertial reference. Hence, Section 4.3.1 is devoted to the experimental platform built to reproduce the transport-induced vibration in the laboratory. In Section 4.3.2, a multi-channel FxLMS algorithm is applied to the experimental platform to realize the vibration reproduction. Then, Section 4.3.3 presents and discusses the vibration reproduction results on the experimental platform. In the end, the experimental platform is further optimized in Section 4.3.4 to improve the accuracy of vibration reproduction on the canvas. This section closely follows the results presented in [GaoEtAl23a, GaoZieglerEberhard23].

4.3.1 Experimental Setup

After the real transport experiment, the investigated painting was taken out from the transport crate without removing the hanging systems and transferred into the laboratory.

All the experimental setup used for vibration reproduction is shown in Fig. 4.6. The ensemble consisting of the investigated painting and the hanging systems was suspended with rubber bands on an aluminum support, forming a very soft suspension which can be approximately considered as a free suspension. Since only the component of each three-dimensional accelerometer perpendicular to the painting plane will be tracked, uniaxial accelerometers of model PCB-333B30 were used here instead. The position of each accelerometer remained the same as in the real transport experiment to ensure the correct comparison of the reproduction results. Four electrodynamic shakers used as actuators were connected to the hanging systems and placed as close as possible to the corresponding accelerometer to excite the vibration there. Each electrodynamic shaker and the hanging system were separated by an elastic O-ring to avoid the armature bending due to an over-tight connection. The electrodynamic shakers are of model PCB TMS-K2007E01. Their output frequency range is DC-9 kHz, and the maximum output acceleration under 0.907 kg load is 3.3 g peak to peak, which fully meets the experimental requirements.

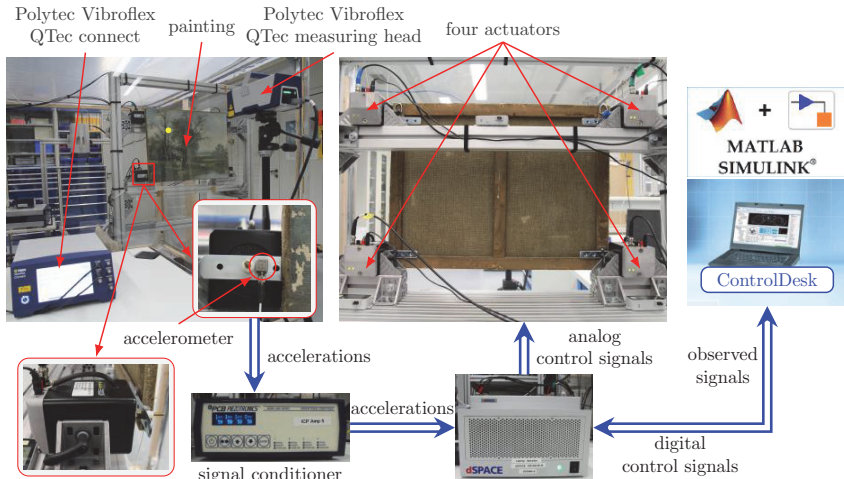


Figure 4.6: The experimental setup used for vibration reproduction of the investigated painting in the laboratory.

During the experiment, the signal conditioner of model PCB-482C24 powered the accelerometers, amplified their output voltages and transmitted them to dSpace. The dSpace device used for hardware-in-the-loop simulation consists of a DS1006 Processor Board, a DS2102 DAC Board, and a DS2004 A/D Board. The accompanying dSpace Controldesk software provided access to the simulation platform as well as to the connected control system. The simulation platform restored the voltage signals collected by dSpace to the

actual acceleration signals. The multi-channel vibration tracking controller in the simulation platform updated the control voltage of each actuator according to the difference between the actual acceleration signals and the desired acceleration signals collected in the real transport experiment. The simulation platform was built in MATLAB/Simulink and loaded into dSpace.

When stably reproducing the vibration on the strainer, the vibration responses of arbitrary points on the canvas can be measured by a Polytec Vibroflex QTec Laser Doppler Vibrometer (LDV). The innovative Polytec Vibroflex QTec LDV has the advantage of using a helium-neon laser source and a multiple channel interferometer which virtually avoids laser drop outs even when measuring uncooperative surfaces. The yellow point on the canvas of the investigated painting in Fig. 4.6 was selected to show the measurement results. This point was selected arbitrarily, but care was taken to avoid selecting a point on a vibration node of a lower eigenmode of the canvas.

The studies in Section 3.4 have shown that the dynamic characteristics of the painting are affected by climate. The data recorded in the transport experiment shows that the relative humidity in the packing case was stable at $52\%\pm0.7\%$ and the temperature was stable at $19.9^{\circ}\text{C}\pm0.5^{\circ}\text{C}$. In order to avoid the influence of changing climate on the experimental results as much as possible, all the vibration reproduction experiments were carried out in a climate chamber. The temperature and humidity in the climate chamber were adjusted to be the same as those in the transport crate during the transport experiment.

4.3.2 Multi-Channel Vibration Tracking Controller

For the vibration reproduction platform designed above, there are four actuators (electro-dynamical shakers) and four accelerometers. Every actuator must control the vibration at the corresponding accelerometer so that it is as identical as possible to the vibration captured during real transport. Therefore, a suitable controller must be designed to control all actuators simultaneously and reproduce the acceleration signals with high accuracy.

4.3.2.1 Multiple-input Multiple-output FxLMS Algorithm

Preliminary experimental results have revealed that the single channel FxLMS algorithm achieved extremely good results in vibration reproduction. However, the use of multiple single channel controllers, each linked to a single accelerometer and an actuator, did not work effectively. Instead, the single channel algorithm had been extended in order to enable it to be used in a multiple-input and multiple-output (MIMO) control scheme. Here, a feedforward controller based on the multi-channel FxLMS algorithm is adopted and its arrangement is illustrated in Fig. 4.7 [HansenEtAl12]. The control signal supplied to each actuator is generated by a separate finite impulse response (FIR) filter, and it is

decided, without loss of generality, that each actuator filter has M stages [WidrowEtAl75]. The desired signal for each accelerometer is derived from the acceleration collected in the real transport experiment. Therefore, the error signal $e_i(k)$ of the i th accelerometer at the sampling time k is the difference between the desired signal $d_i(k)$ and the sum of contributions from each of the N actuators $s_{ij}(k)$ with $N = 4$, in this thesis

$$e_i(k) = d_i(k) - \sum_{j=1}^N s_{ij}(k) \quad i = 1, 2, \dots, N, \quad j = 1, 2, \dots, N. \quad (4.28)$$

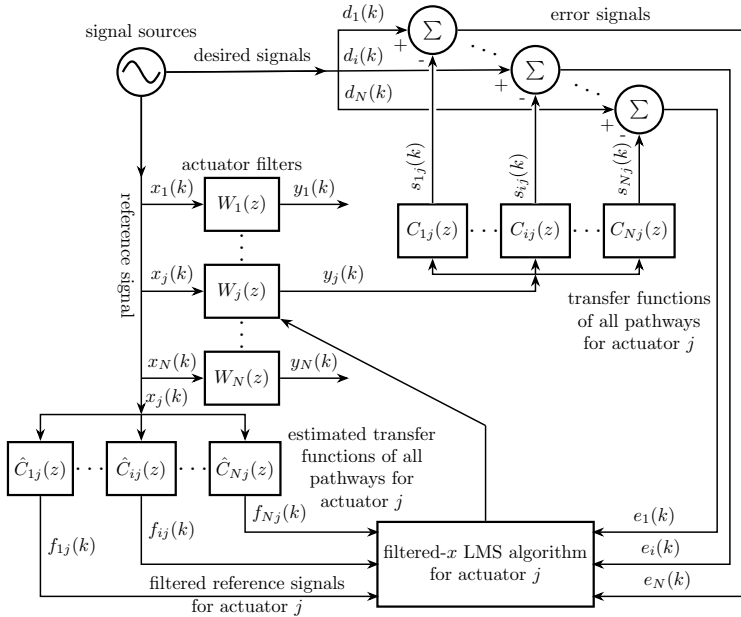


Figure 4.7: Block diagram of an adaptive MIMO feedforward active control system based on the FxLMS algorithm.

The j th actuator component of the i th error signal is not, in general, equal to the output of the j th actuator, but is rather equal to a version of the control signal which has been modified by the pathway transfer function between the output of the j th actuator filter and the collected i th acceleration signal (dSpace \rightarrow actuator \rightarrow accelerometer \rightarrow signal conditioner \rightarrow dSpace). Modeling this transfer function as an m -stage finite impulse response function c_{ij} and assuming that the system is time invariant yields

$$s_{ij}(k) = \mathbf{y}_j^T(k) \mathbf{c}_{ij}, \quad (4.29)$$

where $\mathbf{y}_j(k)$ is a vector of the most recent outputs from the j th actuator filter

$$\mathbf{y}_j(k) = \begin{bmatrix} y_j(k) & y_j(k-1) & \cdots & y_j(k-m+1) \end{bmatrix}^T. \quad (4.30)$$

The output of the j th actuator filter can also be expressed as

$$y_j(k) = \mathbf{x}_j^T(k) \mathbf{w}_j(k), \quad (4.31)$$

where $\mathbf{w}_j(k)$ is the vector of the j th actuator filter weight coefficients at the sampling time k . Then, $s_{ij}(k)$ can be re-expressed in the 'filtered reference signal' format

$$s_{ij}(k) = [\mathbf{X}_j^T(k) \mathbf{w}_j(k)]^T \mathbf{c}_{ij} = \mathbf{w}_j^T(k) [\mathbf{X}_j(k) \mathbf{c}_{ij}] = \mathbf{w}_j^T(k) \mathbf{f}_{ij}(k), \quad (4.32)$$

where $\mathbf{X}_j(k)$ is similar to Equation (4.19), an $M \times m$ matrix of the m most recent reference signal vectors

$$\begin{aligned} \mathbf{X}_j(k) &= [\mathbf{x}_j(k) \quad \mathbf{x}_j(k-1) \quad \cdots \quad \mathbf{x}_j(k-m+1)] \\ &= \begin{bmatrix} x_j(k) & x_j(k-1) & \cdots & x_j(k-m+1) \\ x_j(k-1) & x_j(k-2) & \cdots & x_j(k-m) \\ \vdots & \vdots & \ddots & \vdots \\ x_j(k-N+1) & x_j(k-N+2) & \cdots & x_j(k-m-N+2) \end{bmatrix}, \end{aligned} \quad (4.33)$$

and \mathbf{f}_{ij} is the ij th filtered reference signal vector, 'filtered' by the pathway transfer function between the j th actuator filter output and i th acceleration sensor output. In practical application, the pathway transfer functions \mathbf{c}_{ij} are usually unknown, and their estimates $\hat{\mathbf{c}}_{ij}$ must be used in calculating the filtered reference signal [Bjarnason95]. Thus, each element f_{ij} in this vector is

$$f_{ij}(k) = \mathbf{x}^T(k) \mathbf{c}_{ij} \approx \mathbf{x}^T(k) \hat{\mathbf{c}}_{ij}. \quad (4.34)$$

The key to the practical application of the MIMO FxLMS algorithm is how to construct the desired signals for each error sensor and the reference signals for each actuator. As for the active vibration control system designed in this thesis, the goal of each actuator is simply to make its corresponding accelerometer achieve the expected tracking effect. Thus, the desired signals at each accelerometer are derived from the real transport experiment. As a feedforward controller, it is desirable that every output converges to its input as precisely as possible. So the reference signal of each actuator filter is the same as the desired signal of its corresponding accelerometer, namely,

$$d_i(k) = x_j(k), \quad i = j. \quad (4.35)$$

The cost function used by the LMS algorithm or the single channel FxLMS algorithm is the mean square error. Analogously, for the MIMO control arrangement, its aim is to

realize the error criterion, which is to minimize the sum of the mean square errors of the signal from each accelerometer, Ξ , that is

$$\Xi = \sum_{i=1}^N E\{e_i^2(k)\}. \quad (4.36)$$

Differentiating this with respect to the j th weight coefficient vector produces the gradient estimate, and using it in the standard gradient descent format produces the MIMO filtered- x LMS algorithm. For the j th actuator filter this is expressed as described in [ElliottNelson85, ElliottStothersNelson87] by

$$\mathbf{w}_j(k+1) = \mathbf{w}_j(k) + 2\mu \sum_{i=1}^N \mathbf{f}_{ij}(k) e_i(k), \quad N = 4, \quad (4.37)$$

where μ is the convergence coefficient. Compared to the LMS algorithm or the single channel FxLMS algorithm, the MIMO FxLMS algorithm is more complex to analyze in terms of stability, convergence, and the effect of pathway transfer function estimation errors upon algorithm stability. To summaries conservatively, as with the single channel system, the stability of the MIMO FxLMS algorithm is dependent upon the eigenvalues of the auto correlation matrix of the filtered reference signal. Besides, the algorithm can be made stable if the errors in the estimation of the phase of the pathway transfer functions are all within the bounds of $\pm 90^\circ$. For more detailed information, the interested reader is referred to [SnyderHansen92, HansenEtAl12].

4.3.2.2 Offline Multi-Channel Pathway Modeling

The remaining problem in the above MIMO FxLMS algorithm is how to obtain the estimated pathway transfer functions $\hat{\mathbf{c}}_{ij}$. Although the FxLMS algorithm does not need the pathway model to be very accurate to maintain the stability of the system, a fast and reasonably accurate estimation of the pathway transfer function is important to ensure adequate performance, stability, and convergence speed of the active control system [HansenEtAl12]. For the multiple channel active vibration control system adopted in this thesis with 4 actuators and 4 accelerometers, there are 16 pathways that need to be modeled. Considering the inter-channel coupling effect when the control signals are fed to several actuators, here, all pathways are decided to be modeled simultaneously. Moreover, the variations of all existing pathway transfer functions are considered to be within a small range. Therefore, it is not necessary to do pathway modeling online or by training/learning algorithms. The model obtained offline can be used permanently in the actuator filter weight-update algorithm. The offline pathway modeling method is based on the LMS adaptive algorithm which has been discussed in some depth previously in Section 4.1.1. Here, some 'modeling disturbance' can be injected into all the pathway transfer function 'systems', the input of which is the control filter output and the output

of which is the error sensor output, and into several adaptive filter. Specifically, the offline multi-channel pathway transfer function estimation method applied to this thesis is shown in Fig. 4.8 and described in [WidrowEtAl75, HansenEtAl12, KuoMorgan95].

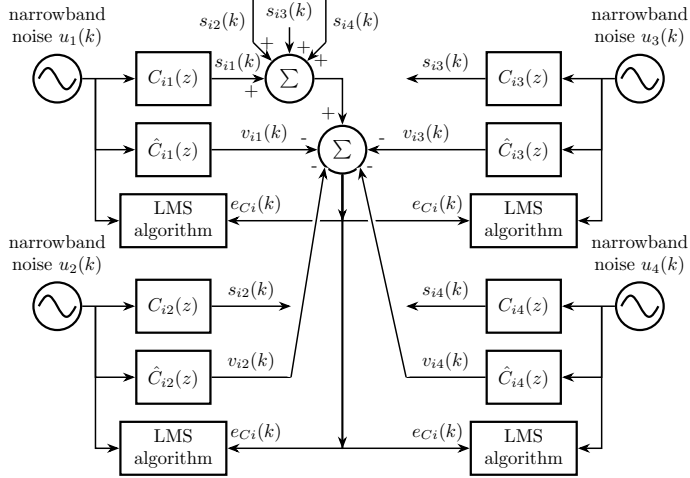


Figure 4.8: Block diagram of modeling all pathways for the MIMO FxLMS control system.

Four narrowband noise sources are fed to the four actuators. The bandwidth of the narrowband noise includes at least the working bandwidth of the MIMO active vibration control system. The residual error signal for the pathway modeling at the i th accelerometer can be written as

$$e_{Ci}(k) = \sum_{j=1}^N \mathbf{u}_j^T(k)[\mathbf{c}_{ij}(k) - \hat{\mathbf{c}}_{ij}(k)], \quad i, j = 1, 2, \dots, N, \quad N = 4. \quad (4.38)$$

Each pathway uses the LMS algorithm to estimate its model, see [HansenEtAl12], namely,

$$\hat{\mathbf{c}}_{ij}(k+1) = \hat{\mathbf{c}}_{ij}(k) + 2\mu \mathbf{u}_j(k) e_{Ci}(k). \quad (4.39)$$

To simplify the analysis, taking the transfer function estimation of the pathway linking the first actuator and the first accelerometer as an example, the relationship after the residual error signal is minimized can be written as

$$\mathbf{u}_1^T(k) \hat{\mathbf{c}}_{11}(k) \approx \mathbf{u}_1^T(k) \mathbf{c}_{11}(k) + \sum_{j=2}^N \mathbf{u}_j^T(k)[\mathbf{c}_{1j}(k) - \hat{\mathbf{c}}_{1j}(k)], \quad N = 4. \quad (4.40)$$

It can be seen from the preceding equation that if the same modeling signal is fed to all pathways, that is, $u_1(k) = u_2(k) = u_3(k) = u_4(k)$, then, there exists

$$\hat{c}_{11}(k) \approx c_{11}(k) + \sum_{j=2}^N [c_{1j}(k) - \hat{c}_{1j}(k)], \quad N = 4. \quad (4.41)$$

This indicates that the estimated model, \hat{c}_{11} , is biased by the cross coupling pathways c_{1j} and \hat{c}_{1j} ($j \neq 1$). The estimation \hat{c}_{11} can converge to c_{11} only when $c_{1j} = \hat{c}_{1j}$. This is unlikely to happen, as \hat{c}_{1j} is also adapting at the same time as \hat{c}_{11} . So there is no unique solution for either filter.

Therefore, to obtain correct models for all pathways, four uncorrelated modeling signals must be used to remove the inter-channel coupling effect [HansenEtAl12]. Besides, uncorrelated modeling signals also contribute to realize the error criterion at each accelerometer when modeling the pathways. After the residual error signal in Equation (4.38) is minimized by the adapting algorithm in Equation (4.39), the following is obtained

$$c_{ij} \approx \hat{c}_{ij}. \quad (4.42)$$

In practice, the corresponding uncorrelated narrowband noise signals are usually selected as the modeling signals according to the operating frequency band of the active vibration control system. To summarize, in this case, correct estimations are obtained for all the pathway transfer functions between the actuators and the accelerometers, which can be used in the MIMO control system described above.

4.3.3 Vibration Reproduction on the Strainer

Utilizing the experimental setup built above and the designed multi-channel vibration tracking controller, some vibration reproduction experiments can be carried out. This section will begin by introducing the parameters used in the active vibration control system, as well as some of preprocessing steps performed on the vibration collected from the real transport experiment. Then, according to the experimental results, the performance and effect of this vibration reproduction platform will be discussed.

4.3.3.1 Parameters and Preprocessing

The desired signals for each accelerometer were obtained from the real transport experiment and were acquired at a sampling rate of 5 kHz corresponding to $\Delta t = 0.2$ ms. However, such a high sampling rate need not and cannot be adopted during vibration reproduction due to hardware limitations of the real-time environment. For the multi-channel vibration tracking controller, all the actuator filters and the pathway filters are set to 100 stages. Therefore, a total of 100-order matrix operations of 16 pathways are involved in the update

process of the control algorithm. Coupled with other operations such as data acquisition, dSpace cannot complete all operations within a sampling period of 0.2 ms and the real-time simulation cannot be performed. Clearly, reducing the stage of the FIR filter increases the usable sampling frequency, but also degrades the performance of the controller. In this conflict, the sampling frequency during the vibration reproduction experiment was set as 1 kHz, i.e. $\Delta t = 1$ ms, to maintain the unchanged stage of the FIR filter.

The output performance of the electrodynamic shaker used in this thesis is limited by the fact that its acceleration output waveform has a large distortion below 5 Hz. Besides, considering that the first eigenfrequency of the investigated painting is about 7.5 Hz, the minimum operating frequency of the multi-channel vibration tracking controller is fixed at 5 Hz. According to the Nyquist-Shannon sampling theorem, when the sampling frequency is 1 kHz, there is no aliasing effect for signals below 500 Hz. The analysis of acceleration signals collected from the real transport experiment shows that their amplitudes of high frequency components are usually small. Furthermore, high frequency excitation is assumed to have neglectable effect on the damage of the canvas, because the vibration displacement of the canvas caused by high frequency excitation is typically weak due to the painting's inertia. Therefore, the highest operating frequency of vibration reproduction is set as 100 Hz in this thesis. A large number of canvas eigenmodes have already been contained in this operating frequency range [GaoEtAl23b]. This does not mean that the designed multi-channel vibration tracking controller can only work within this range. In fact, the experimental results of the single sinusoidal test have shown that it can work stably between 5 Hz and 500 Hz on our hardware. However, affected by noise, small vibration signals at very high frequency are neither relevant to painting damage nor difficult for the controller to reproduce.

Thus, before performing the vibration reproduction experiment, the original acceleration signals collected from the real transport experiment have to be preprocessed. The components between 5 Hz and 100 Hz were first extracted using a bandpass filter, and then resampled using a sampling frequency of 1 kHz. As shown in Fig. 4.9, a short but representative section of an acceleration signal collected from the real transport experiment are selected for comparison before and after preprocessing. Except for the loss of very high frequency components above 100 Hz, the dominant characteristics of the acceleration signal do not change much.

Besides, the transfer functions of all pathways linking each actuator and each accelerometer should also be estimated in advance before the vibration reproduction experiments. First, four sets of vectors with length 200000 (200 s and $\Delta t = 1$ ms) were generated in Matlab by normally distributed pseudo-random numbers. These four vectors were generated randomly and were always uncorrelated with each other. They were then passed through a bandpass filter with cutoff frequencies of 5 Hz and 100 Hz, producing four sets of uncorrelated narrowband noise. The four narrowband noise signals were fed to the four actuators

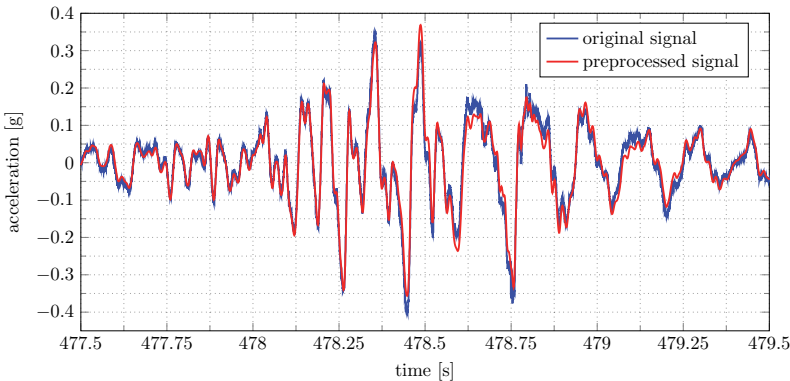


Figure 4.9: Comparison of a short section of the acceleration signal from the transport experiment before and after processing.

through the dSpace device and the transfer functions of all pathways were estimated using the offline modeling method described in Section 4.3.2.2. The normalized LMS algorithm was used instead of the basic LMS algorithm to improve the convergence speed. The estimation was considered to be completed when the filter coefficients of the individual pathway transfer functions converged stably. As an example, the estimation \hat{c}_{11} of the pathway transfer function linking the first actuator and the first accelerometer is illustrated in Fig. 4.10. The higher the filter order, the more the coefficients converge to zero, which indicates that a FIR filter with 100 stages is sufficient to estimate the pathway transfer function.

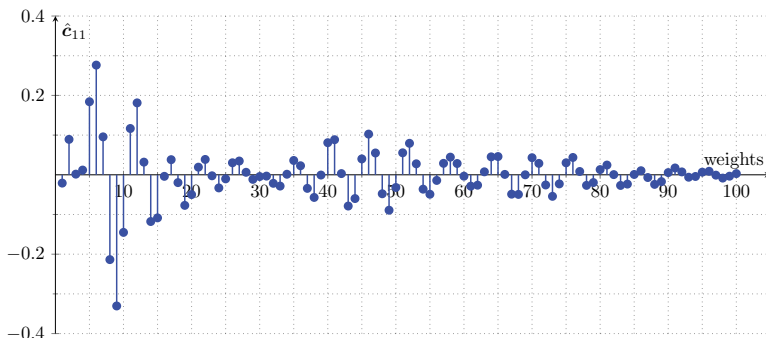


Figure 4.10: Estimates of the weight coefficients for the pathway transfer function c_{11} .

4.3.3.2 Reproduction for Vibration Response

The excitations of the painting during transport can be roughly divided into shock and vibration. The characteristics of the painting response to vibration excitation are that its amplitude and frequency change much slower than that for the shock response and repeat to a higher degree than that for single shock response. For example, when a transport vehicle is driving at a relatively steady speed on a highway, if the road condition is good, the measured response corresponds to the vibration response of the painting. The acceleration signals with a duration of 840 s collected from the real transport experiment are reproduced, and the reproduction results of a small section of the vibration response on the strainer are shown in Fig. 4.11.

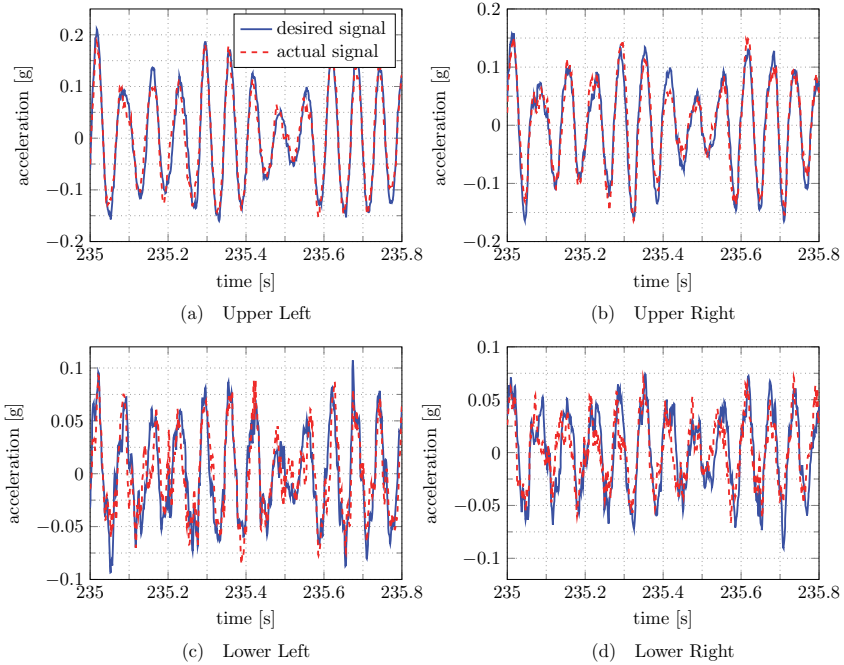


Figure 4.11: Reproduction results on the strainer for a short section of the normal vibration response.

The 'Upper Left' in Fig. 4.11a refers to the data of the accelerometer in the upper left corner when facing the investigated painting, and analogously for the other plots in Fig. 4.11. The FxLMS algorithm achieves good to satisfactory agreement for all accelerometers,

although the agreement for the two lower accelerometers is somewhat degraded due to the larger extend of high frequency components. The amplitude frequency response curves of all signals within the time range shown in Fig. 4.11 are plotted in Fig. 4.12. It further indicates that the FxLMS algorithm achieves good reproduction effect on the dominant components of the signal, but the reproduction results on the vibration with smaller amplitudes, especially those containing high frequency components, are poor.

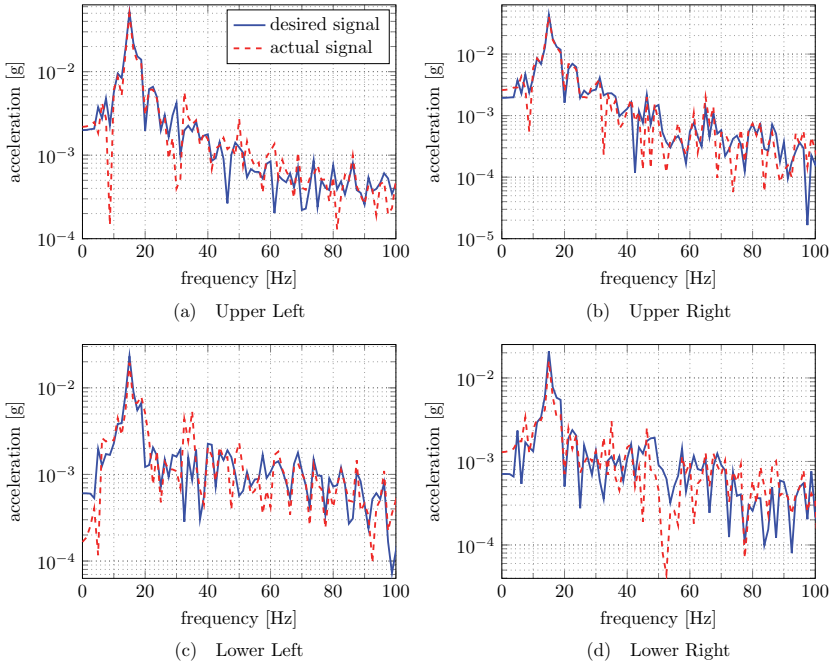


Figure 4.12: Amplitude frequency response curves of the signals in Fig. 4.11.

From the real transport experiment, it was observed that the vibration response amplitude of the painting rarely exceeds 0.25 g. Thus, the results presented in Fig. 4.11 show the reproduction quality for the higher levels of vibration amplitude. For smaller amplitudes around 0.01 g, as presented in Fig. 4.13, the reproduction effect still remains good. For the weaker vibration, the effect of vibration reproduction will deteriorate due to the influence of noise in the sampling channel. However, this is considered as uncritical since these weak vibration does not contribute to the damage to the painting.

In general, the reproduction effect on the strainer for the vibration response using the multi-channel vibration tracking controller has reached the expectation. However, its

ability to reproduce the shock response remains to be validated.

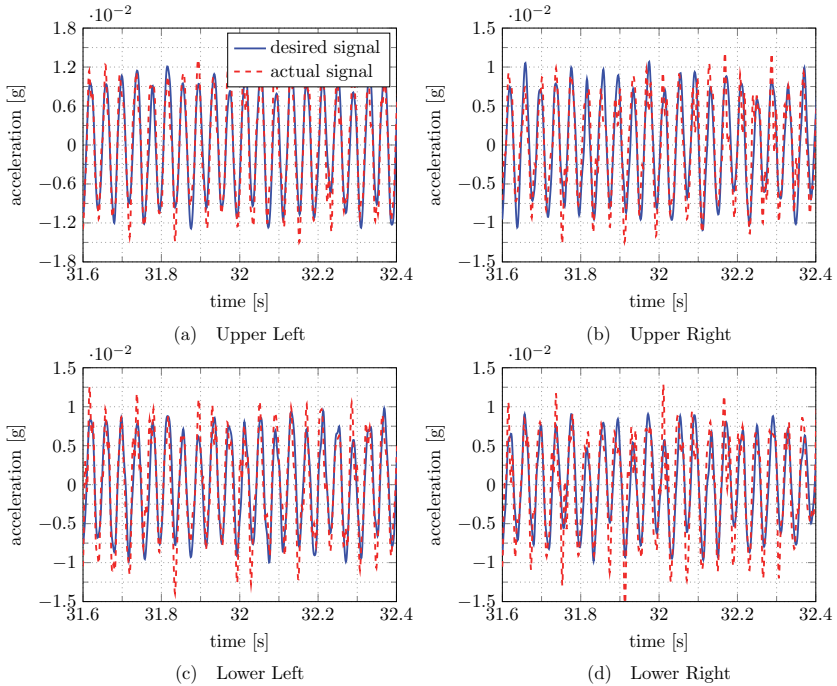


Figure 4.13: Reproduction results for a short section of the lower vibration response.

4.3.3.3 Reproduction for Shock Response

The response of the painting when being subjected to shock excitation during transport is a highly transient behavior. The shock response is characterized by rapid rise and decay of the amplitude in a short time, and the energy is distributed over a wide frequency band. For example, when the transport vehicle brakes suddenly or passes a pothole in the street, the response of the painting is dominated by the shock response. According to this characteristic, strong shock responses can easily be distinguished from normal vibration responses in the real transport experiment. However, for events of smaller shock amplitude this distinction becomes more and more difficult. The maximum amplitude of the shock response observed in the real transport experiment reaches 0.5 g. The rapid changes on amplitude and frequency pose great challenges to the multi-channel vibration tracking controller. The reproduction results of a higher shock response during the real transport

experiment are shown in Fig. 4.14.

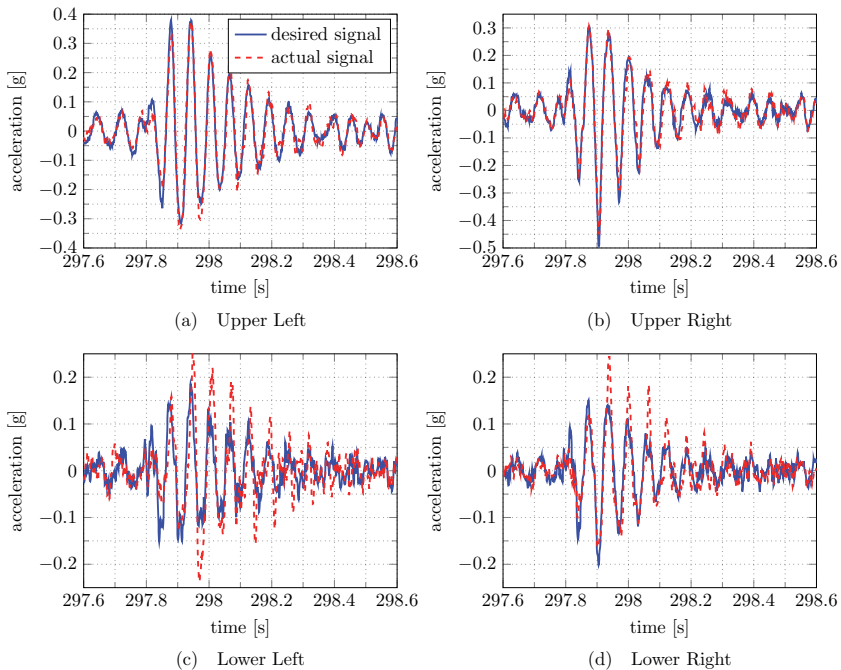


Figure 4.14: Reproduction results for a short section of the shock response.

Obviously the overall behavior is again represented well. Particularly for the two upper accelerometers the agreement is very good. The two lower accelerometers, however, show noticeable overshoot. Actually it is also observed in Figs. 4.11 and 4.13 that the vibration reproduction at the upper two accelerometers is always better than that at the lower two accelerometers. This must be related to the characteristics of the slower convergence speed of the FxLMS algorithm. However, it should also be pointed out that for the multi-channel FxLMS algorithm the cost function in Equation (4.36) aims to minimize the sum of the mean square errors of the signal from each accelerometer, but cannot completely eliminate the inter-channel coupling effect. Especially during the real transport, the amplitudes of the upper two accelerometers are usually about twice that of the lower two accelerometers, which makes vibration reproduction at the lower two accelerometers more affected by inter-channel coupling effects. Moreover, in terms of hardware, the hanging systems of the investigated painting during the transport experiment were rigidly connected to the crate. Although in the laboratory the hanging systems and the shakers were also rigidly

connected, the connection between the armature of the shaker and its support flexure was softer than the connection in transport. This elastic connection may have increased the difficulty of reproducing the shock response.

On the whole, the reproduction results still reflect most of the information about the shock response of the investigated painting. The reproduction results for both the vibration and shock responses can be considered as being fully acceptable for the intended use.

4.3.3.4 Reproducibility Test

The purpose of the vibration reproduction system designed in this thesis is to reproduce the vibration on the strainer during transport as precisely as possible, so as to observe the response of the canvas in the laboratory with respect to an inertial reference. The measurement on the canvas can provide a reference for its unknown response during the real transport. With this reference information, it is possible to assess the transport effects of paintings, to predict the potential damage to paintings caused by transport and to explore damage mechanisms of paintings during transport. All these advanced investigations require the support of a stable vibration reproduction capability. Given that a feedback controller was used for realizing vibration reproduction in the early stages of this study, the phenomenon of error propagation was found. In other words, as the reproduction experiment repeats over a long period of time, vibration reproduction deteriorates and even the control system may diverge. Therefore, it is important to investigate whether the designed vibration reproduction system itself has a stable reproducibility, i.e., whether repeated experiments really yield identical behavior. In theory, although the convergence speed of the multi-channel FxLMS algorithm is slow, as long as the iteration step size is set reasonably, the parameters of the controller are updated continuously to offset external disturbances and there is no error propagation. In order to verify the reproducibility, a repeated vibration reproduction experiment was carried out. The acceleration signals with a duration of 730 s were reproduced repeatedly several times. The velocity response of each cycle for the selected measurement point on the canvas described in Section 4.3.1 was observed by the Laser Doppler Vibrometer. The comparison of the velocity responses over a small period of time for the 3rd, 5th and 7th cycles is shown in Fig. 4.15.

Evidently, the comparison in Fig. 4.15 shows that there are only very minor differences between the different vibration reproduction cycles. The source of the difference may be the interference of external environmental noise and the influence of climate fluctuations. Anyway, this proves that the designed vibration reproduction system has a long-term stable reproducibility.

Since a uniaxial accelerometer was attached on the back of the canvas during the real transport experiment, it is necessary to compare the canvas vibration reproduced in the laboratory and collected in the real transport to further evaluate the performance of the

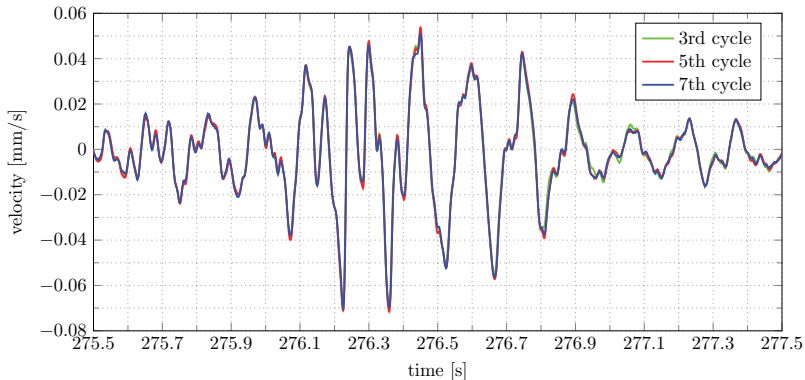


Figure 4.15: A comparison of velocity responses of selected measurement point on the canvas at different cycles.

vibration reproduction system. As a matter of fact, the comparison results are not as satisfactory as expected and such poor results are not shown here. Only a small portion of the vibration reproduction results on the canvas are in close agreement with the vibration captured in the real transport experiment. This indicates that the existing vibration reproduction system is in dire need of further optimization to meet the requirement of reproducing the canvas vibration.

4.3.4 Vibration Reproduction on the Canvas

In order to remedy the shortcomings when reproducing vibration on the canvas, an improvement to the existing vibration reproduction system is proposed in this section. The improved vibration reproduction performance will be experimentally validated both on the strainer and on the canvas. Lastly, an example is presented to illustrate how to further process the reproduced canvas vibration in the laboratory for relevant evaluation.

4.3.4.1 Improved Experimental Setup

It has been demonstrated experimentally in the preceding section that even though the existing vibration reproduction system has a very good reproduction on the strainer, the vibration reproduction on the canvas falls short of expectations. Admittedly, the fluctuation of temperature and humidity inside the climate box and the convergence accuracy of the multi-channel FxLMS control algorithm are contributing factors, but both of them are difficult to be further optimized and are not considered major factors in this

thesis. It is argued in this thesis that the dominant factor is the difference in boundary conditions between the investigated painting during transport and in the laboratory, i.e., the dynamic characteristics of the investigated painting during transport and in the laboratory are quite different due to the difference in the installation methods. It can be visualized in Fig. 4.4 that the investigated painting was rigidly mounted on a wooden plate during transport by means of the hanging systems. The wooden plate and the painting as a whole were held in the crate by four frame legs. The external excitation was transmitted from the crate through the internal structure to the frame legs and then to the wooden plate, finally causing the vibration of the painting, while in the laboratory, as shown in Fig. 4.6, four electrodynamic shakers were connected to the hanging systems of the investigated painting, which led to a direct excitation on the strainer. Compared to the real transport, the investigated painting in the laboratory is more flexible and hence has lower eigenfrequencies, because it is not supported by a stiffer wooden plate. Therefore, even if it is possible to reproduce the vibration on the strainer in the laboratory with a high degree of accuracy, the vibration on the canvas would not be precisely the same as that during transport due to changes in the dynamic characteristics of the painting.

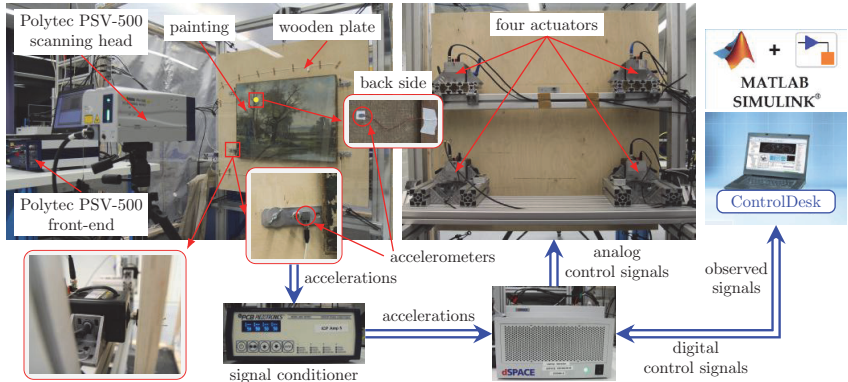


Figure 4.16: The improved experimental setup used for laboratory vibration reproduction on the canvas.

In order to overcome this distinction and keep the dynamic characteristics of the investigated painting as constant as possible, the experimental setup for vibration reproduction in the laboratory is improved as shown in Fig 4.16. A stiff wooden plate measuring 98 cm × 95 cm × 2 cm was suspended from the aluminum support with rubber bands. The ensemble consisting of the investigated painting and the hanging systems was fixed on the wooden plate, similar to the state inside the transport case. Since the investigated painting was supported by the a wooden plate, its dynamic characteristics should be close to those

during transport. Considering that the accelerometers were attached on the hanging systems, four through holes closest to the accelerometers were drilled at the wooden plate. The stinger of four electrodynamical shakers were connected to the wooden plate through these through holes. The four actuators excited the vibration of the assembly composed of the wooden plate and the investigated painting. Because the load was so heavy, a rubber pad was sandwiched between the electrodynamical shaker and the wooden plate to prevent distortion of the shaker armature due to excessive deflection. Based on this improvement and driven by the dSpace device with a multi-channel FxLMS algorithm, if a good vibration reproduction on the strainer can be obtained again, the vibration on the canvas is reproduced close to those collected during transport.

The rest of the experimental equipment is essentially the same as described in Section 4.3.1. The only change is the replacement of a Polytec PSV-500 Laser Doppler Vibrometer. It does not affect the experimental results. Following this, in order to verify that the above improvement is effective, some vibration reproduction experiments are again performed.

4.3.4.2 Improved Vibration Reproduction Results

The same segment of acceleration signals with a duration of 840 seconds collected from the real transport experiment was again used as the desired signals for vibration reproduction experiments. After several cycles, the control algorithm completely converged and a small section of the vibration signals reproduced on the strainer was intercepted and compared with the desired signals, as shown in Fig. 4.17. This short section of the vibration reproduction results contains the response to shock excitation (about 328.5 s to 329.3 s) and the response to vibration excitation (about 329.3 s to 331 s). They reflect typical acceleration signals observed on the strainer of the investigated painting during transport. Clearly, for the improved experimental setup, the multi-channel FxLMS algorithm achieves good agreement for all accelerometers as before. There is still little overshoot in the reproduction of the shock response and also some deterioration in the vibration reproduction for the high frequency components. In addition, it should be noted that the electrodynamical shaker used in this thesis has limited output capability (3.3 g peak to peak under 0.907 kg load). The maximum acceleration captured during the real transport experiment is approximately 0.5 g. The improved experimental setup is heavy, and the four shakers are only barely adequate. To reproduce higher acceleration signals, the actuators must be replaced with ones that have a higher output capacity.

Although the application of sensors on the canvases of original valuable paintings is prohibited from a conservatory perspective, during the transport and the reproduction experiments, see Figs. 4.4 and 4.17, a uniaxial accelerometer was attached on the back of the canvas (of our investigated artistically not important painting) to assess the reproduction effect on the canvas. With the aid of the improved experimental setup, the reproduction

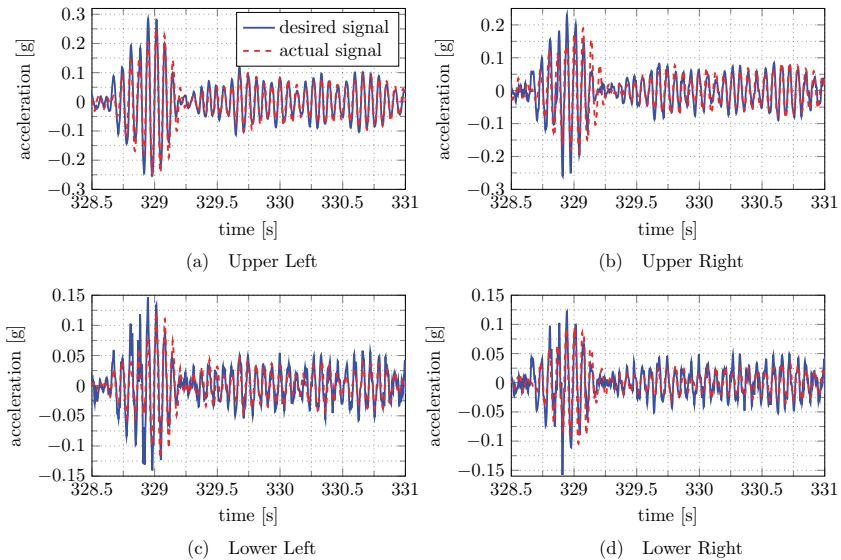


Figure 4.17: Improved reproduction results on the strainer for a short section of the signals containing the shock and vibration response.

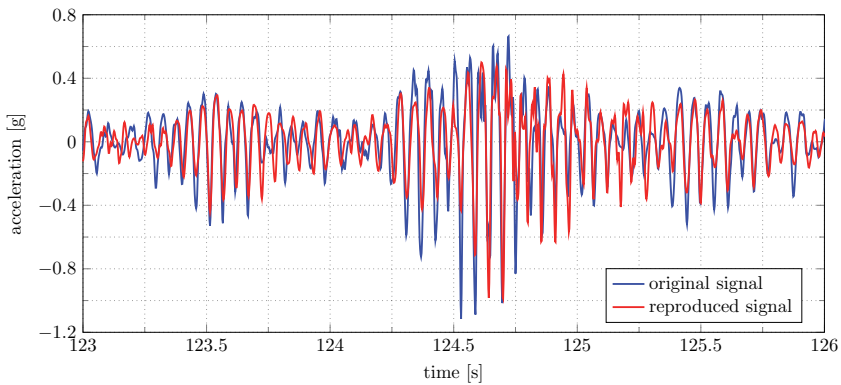


Figure 4.18: Comparison of vibration reproduction results on the canvas with signals collected during transport.

results of a short section of vibration signal on the canvas are shown in Fig. 4.17. The overall behavior is represented well, both in terms of shock response and vibration response.

However, due to small differences in the vibration reproduction on the strainer, fluctuations of the climate inside the climate box, and differences in the state of the painting in the laboratory and during transport, there is a negligible phase error in the reproduction results. The reproduction of the high frequency components is still slightly too low.

Up to this point, the reproduction results have met the initial expectations, both on the strainer and on the canvas. Therefore, the designed vibration reproduction platform can be further used for purposes such as evaluating transport effects or predicting potential damage to paintings.

4.3.4.3 Rainflow Counts for Transport Analysis

Regardless of the purpose for which the vibration reproduction platform designed above is used, the problem remains how to post-process the vibration reproduction results on the canvas to make them more intuitive and easier to understand and compare. This thesis proposes to emulate the rainflow counting algorithm used for fatigue analysis to count and analyze the vibration reproduction results on the canvas. In fatigue analysis, the strain-time history data record is flipped 90°, with the time axis vertically down, so that the data record resembles a series of roofs, with rain running down the roofs, hence the name rainflow counting [Lalanne14]. The specific algorithm for rainflow counting can be found in [ASTMInternational17].

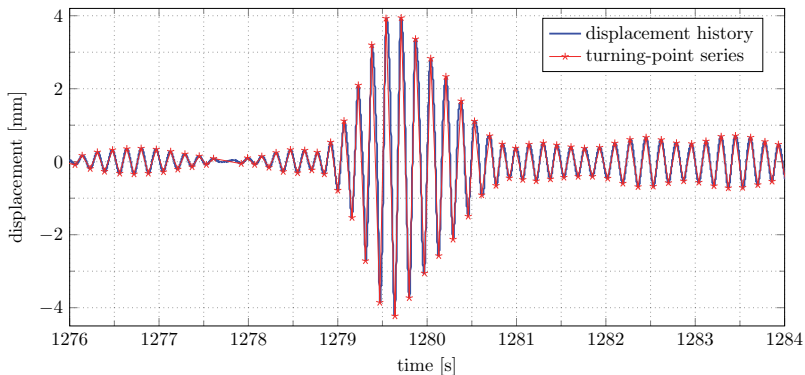


Figure 4.19: A short section of the displacement signal reproduced on the canvas and the turning-points after peak-valley filtering.

Analogous to this process, the vibration displacement is first obtained by integrating the reproduced vibration velocity at an arbitrary point on the canvas. Then observe the displacement data, set a threshold and remove cycle whose contribution to the analysis

is insignificant. Next, preserve only the maximum and minimum value of the cycles and remove the points in between. Only maximum and minimum values are relevant for the analysis. As an illustration, a small section of the displacement signal reproduced on the canvas is shown in Fig. 4.19, as well as the detected peaks and valleys of every cycle where the amplitude is above a threshold of 0.1 mm. After finding the turning point (peak and valley) of each valid cycle, the cycle counting can be performed based on the rainflow algorithm. The real transport experiment described in Section 4.2.1 lasted for one hour, and a complete reproduction of this transport experiment was conducted in the laboratory. The vibration reproduction results at an arbitrary point on the canvas were collected and statistically analyzed using the rainflow-counting algorithm described above. Consequently, the relationship between the vibration displacement and the number of cycles is obtained, as shown in Fig. 4.20. In this figure it is displayed that there are 5000 vibration cycles with an amplitude greater than 1 mm for the selected point. This thesis only suggests that the rainflow-counting algorithm can be used for transport analysis, but the more expansive studies of transport assessment and damage prediction require more experimental data, which is beyond the scope of this thesis.

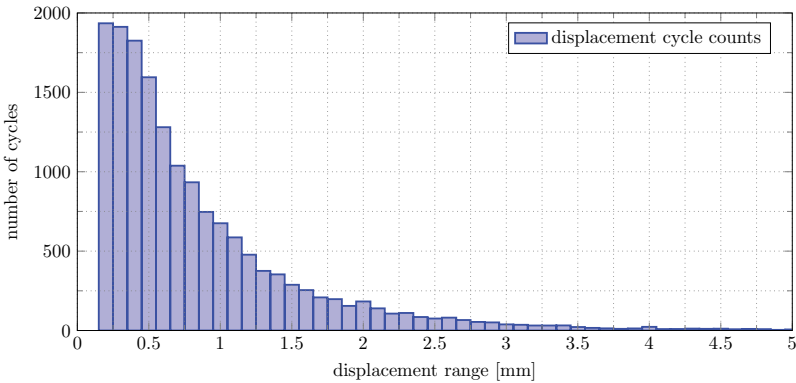


Figure 4.20: Rainflow counting results for reproduced vibration displacement at a point on the canvas.

4.4 Reconstruction of Transport-induced Vibration

Although the unknown vibration on the canvas during transport are indirectly monitored in the laboratory by means of vibration reproduction in the preceding section, this method is rather time-consuming and laborious, and occupies too much equipment to be generalized to art conservators. Hence, the second approach is developed in this thesis for simulating

the transport-induced vibration of paintings. It is a more accessible alternative compared to the vibration reproduction method. The basic idea of this approach is to establish a numerical model in the laboratory that describes the relationship between the vibration collected by the four accelerometers on the strainer and the vibration at an arbitrary point on the canvas. If the dynamic behavior of the painting in the laboratory is consistent with that during transport, then the vibration at an arbitrary point on the canvas can be reconstructed by inputting the vibration data on the strainer into the numerical model. For this purpose, the numerical model is first derived in Section 4.4.1. After that, the methodology of developing this numerical model and reconstructing the transport-induced vibration on the canvas is addressed in Section 4.4.2. In Section 4.4.3 is then the experimental setup and measurements shown. Subsequently, the optimal numerical model is determined by numerical analysis in Section 4.4.4. Finally, the effectiveness of this approach is demonstrated in Section 4.4.5 by using an example of developing a numerical model applicable of the real transport experiment.

4.4.1 Numerical Model

For ease of analysis, referring to Fig. 4.4, the state of the investigated painting during the real transport is simplified to the structure presented in Fig. 4.21. The investigated painting is mounted on a wooden crate by hanging systems. The external excitation is transferred to the painting via the crate during transport. The accelerometers A_i ($i = 1, 2, 3, 4$) are fixed to one hanging system. It does not matter whether they are uniaxial accelerometers or triaxial accelerometers, because only the component perpendicular to the painting plane is critical, as discussed in Section 4.2.2. The hanging systems and the strainer of the painting are rigidly connected, and, thus, the vibration captured by the accelerometers can represent the vibration on the strainer. There is no direct contact between the investigated painting and the crate. An arbitrary point p on the canvas is selected as the point to be investigated or measured.

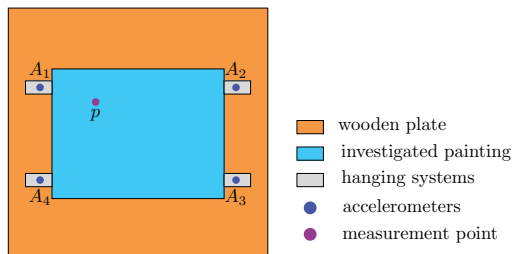


Figure 4.21: A sketch of the state of the investigated painting inside the transport case.

Despite the successful identification of modal parameters for the real painting in Section 3.3.2.3, as shown in Fig. 3.17, the reconstructed frequency response function (FRF) obtains a very good fit only near the eigenfrequencies. It is expected that the vibration reconstruction on the canvas by identified modal parameters cannot achieve satisfactory results, when the vibration frequency deviates far from the eigenfrequency. Since the vibration on the strainer during transport can be captured by accelerometers, this thesis intends to develop a model to describe the relationship between the vibration on the strainer and at an arbitrary point on the canvas. To discover this relationship, the FRF remains a good starting point. In Fig. 4.21, the FRFs at each accelerometer and at the investigated point p on the canvas can be expressed as

$$\alpha_{ij}(\omega) = \frac{A_i(w)}{F_j(w)}, \quad \beta_{pj}(\omega) = \frac{V_p(w)}{F_j(w)}, \quad (4.43)$$

where $\alpha_{ij}(\omega)$ is the accelerance between the i^{th} accelerometer and the excitation point j , and $\beta_{pj}(\omega)$ is the mobility between the investigated point p and the excitation point j . The Fourier transforms of the excitation $f_j(t)$, acceleration response $a_i(t)$, and velocity response $v_p(t)$ are $F_j(\omega)$, $A_i(\omega)$ and $V_p(\omega)$.

In the laboratory, if the experimental modal analysis is performed by the single input, single output method, Equations (4.43) are perfectly applicable for describing the measured FRFs. However, the transport case is necessarily subjected to multiple excitations all the time during transport. Moreover, the magnitudes and locations of these excitations are always unknown. If the research is limited to the vibration of the investigated point p perpendicular to the painting plane, this is a multiple input, single output problem. Equation (4.43) must be modified to accommodate the situation at the time of transport.

Although all the excitations during transport are unknown, they can be decoupled into generalized forces corresponding to the individual degrees of freedom, i.e., F_x , F_y , F_z , M_x , M_y and M_z , under the painting coordinate system established in Section 2.3. It is assumed that all vibration of the investigated painting during transport is within the linear range, that is, the individual generalized forces do not produce nonlinear vibration on the painting and the vibration produced by the individual generalized forces on the painting is independent of each other. Furthermore, as already discussed in Section 4.2.2, this thesis limits itself to the simulation of transport-induced vibration perpendicular to the painting plane, because only these vibration is particularly relevant to damage. The transport-induced vibration perpendicular to the painting plane can be decomposed into a transverse translation caused by the generalized force F_z , a rotation around the longitudinal axis caused by the generalized force M_x and a rotation around the vertical axis caused by the generalized force M_y . The transport-induced vibration generated by other generalized forces is not relevant to the subject of this thesis. Hence, by the linear superposition method, the acceleration response at each accelerometer on the strainer and

the velocity response at the investigated point p on the canvas can be expressed as

$$A_i(\omega) = \alpha_{iz}(\omega)F_z(\omega) + \alpha_{ix}(\omega)M_x(\omega) + \alpha_{iy}(\omega)M_y(\omega) \quad (4.44)$$

and

$$V_p(\omega) = \beta_{pz}(\omega)F_z(\omega) + \beta_{px}(\omega)M_x(\omega) + \beta_{py}(\omega)M_y(\omega), \quad (4.45)$$

where α_{iz} , α_{ix} and α_{iy} are the accelerances of the corresponding generalized forces at the i^{th} accelerometer, and β_{pz} , β_{px} and β_{py} are the mobilities of the corresponding generalized forces at the investigated point p on the canvas.

All accelerances and mobilities in Eqs. (4.44) and (4.45) are also unknown during transport, but they are assumed for moment to be observable in the laboratory in order to find the relationship between the acceleration response on the strainer and the velocity response on the canvas. Then, by Equation (4.44), the acceleration response of all accelerometers at each frequency point can be written as

$$\begin{bmatrix} \alpha_{1z}(\omega) & \alpha_{1x}(\omega) & \alpha_{1y}(\omega) \\ \alpha_{2z}(\omega) & \alpha_{2x}(\omega) & \alpha_{2y}(\omega) \\ \alpha_{3z}(\omega) & \alpha_{3x}(\omega) & \alpha_{3y}(\omega) \\ \alpha_{4z}(\omega) & \alpha_{4x}(\omega) & \alpha_{4y}(\omega) \end{bmatrix} \begin{bmatrix} F_z(\omega) \\ M_x(\omega) \\ M_y(\omega) \end{bmatrix} = \begin{bmatrix} A_1(\omega) \\ A_2(\omega) \\ A_3(\omega) \\ A_4(\omega) \end{bmatrix}, \quad (4.46)$$

and further abbreviated as

$$\Theta(\omega)\mathbf{f}(\omega) = \mathbf{A}(\omega), \quad (4.47)$$

where at each considered frequency, $\Theta(\omega) \in \mathbb{C}^{4 \times 3}$ is the matrix containing the accelerances of all accelerometers, $\mathbf{f}(\omega) \in \mathbb{C}^{3 \times 1}$ is the generalized force vector and $\mathbf{A}(\omega) \in \mathbb{C}^{4 \times 1}$ is the acceleration response vector of all accelerometers. Since there are four accelerometers, more than the number of generalized forces, an ordinary linear least squares estimator is used at each considered frequency to form the estimates of the generalized forces, that is

$$\mathbf{f}(\omega) = (\Theta^T(\omega)\Theta(\omega))^{-1}\Theta^T(\omega)\mathbf{A}(\omega). \quad (4.48)$$

Substituting the estimated generalized forces into Equation (4.45), the velocity response at the investigated point p on the canvas for each considered frequency can be re-expressed as

$$V_p(\omega) = [\beta_{pz}(\omega) \ \beta_{px}(\omega) \ \beta_{py}(\omega)](\Theta^T(\omega)\Theta(\omega))^{-1}\Theta^T(\omega)\mathbf{A}(\omega). \quad (4.49)$$

The vector $[\beta_{pz}(\omega) \ \beta_{px}(\omega) \ \beta_{py}(\omega)] \in \mathbb{C}^{1 \times 3}$ contains all the necessary mobility information. The matrix $(\Theta^T(\omega)\Theta(\omega))^{-1}\Theta^T(\omega) \in \mathbb{C}^{3 \times 4}$ contains all the necessary accelerance information. There is no doubt that their product at each considered frequency can be merged into a single vector, which is defined as $\Psi(\omega) = [\psi_1(\omega) \ \psi_2(\omega) \ \psi_3(\omega) \ \psi_4(\omega)] \in \mathbb{C}^{1 \times 4}$. Consequently, the velocity response at the investigated point p on the canvas in Equation (4.49) can be further simplified to

$$V_p(\omega) = \Psi(\omega)\mathbf{A}(\omega) = \mathbf{A}^T(\omega)\Psi^T(\omega). \quad (4.50)$$

Equation (4.50) indicates that the vector $\Psi(\omega)$ relates the information from the four accelerometers on the strainer to the velocity information at an arbitrary point p on the canvas. Therefore, the vector $\Psi(\omega)$ at each considered frequency is the model to be established in this thesis to reconstruct the canvas vibration. This model bypasses the difficulty of solving the generalized force. Moreover, it incorporates both acceleration and mobility information. From twelve accelerances in Equation (4.46) and three mobilities in Equation (4.45) to four parameters in vector $\Psi(\omega)$, the model reduces the number of parameters to be identified. Although it is possible to identify the modal parameters to represent the acceleration and the mobility, it has been shown that the fit was not good at each frequency. Thus, it is expected that the model $\Psi(\omega)$ at all considered frequencies is difficult to express mathematically. The easiest way to obtain the model $\Psi(\omega)$ is to identify its numerical form in the laboratory.

Since there are four unknown parameters in the vector $\Psi(\omega)$ at each considered frequency, at least four equations are required to identify all parameters. Assuming that multiple excitations are performed at different locations on the transport crate, it is possible to obtain a matrix equation from Equation (4.50)

$$\begin{bmatrix} A_{11}(\omega) & A_{12}(\omega) & A_{13}(\omega) & A_{14}(\omega) \\ A_{21}(\omega) & A_{22}(\omega) & A_{23}(\omega) & A_{24}(\omega) \\ \vdots & \vdots & \vdots & \vdots \\ A_{n1}(\omega) & A_{n2}(\omega) & A_{n3}(\omega) & A_{n4}(\omega) \end{bmatrix} \begin{bmatrix} \psi_1(\omega) \\ \psi_2(\omega) \\ \psi_3(\omega) \\ \psi_4(\omega) \end{bmatrix} = \begin{bmatrix} V_{1p}(\omega) \\ V_{2p}(\omega) \\ \vdots \\ V_{np}(\omega) \end{bmatrix}, \quad n \geq 4, \quad (4.51)$$

where at each considered frequency, $A_{ni}(\omega)$ is the acceleration response of the i^{th} accelerometer and $V_{np}(\omega)$ is the velocity response of the investigated point p on the canvas, when the excitation is performed at the n^{th} point on the transport crate. Equation (4.51) can also be solved by the ordinary linear least squares method, which yields

$$\Psi(\omega) = (\hat{\mathbf{A}}^T(\omega)\hat{\mathbf{A}}(\omega))^{-1}\hat{\mathbf{A}}^T(\omega)\mathbf{V}_p(\omega), \quad (4.52)$$

where $\hat{\mathbf{A}}(\omega)$ and $\mathbf{V}_p(\omega)$ contain the acceleration and velocity information of all excitation points at each considered frequency. The matrix $\hat{\mathbf{A}}(\omega)$ must be chosen carefully, otherwise the parameter estimation problem is ill-conditioned in the sense that small errors in the data can produce arbitrarily large errors in the parameter estimates. Therefore, the next issue to be discussed is how many excitation points should be selected at least, and how to choose their locations, in order to establish a good numerical model that can reconstruct the canvas vibration with a high accuracy.

4.4.2 Methodology for Numerical Modeling

Due to the fact that the actual transport crate is bulky and does not allow for any modifications, it is laborious to conduct experiments directly on the transport crate to

establish the numerical model. In view of the good vibration reproduction results on the canvas in Section 4.3.4, rigidly connecting the investigated painting to a wooden plate gives almost the same dynamic characteristics as during transport. This scheme is followed here for the numerical modeling. As shown in Fig. 4.22, an 11×13 excitation lattice is created on the back of the wooden plate. Each point on the lattice is a possible excitation location. The range of the lattice is only slightly wider than the range covered by the investigated painting, because it is difficult to fully excite the eigenmodes of the painting from excitation points that are too far away. In order to cross-compare whether the same excitation scheme works for different points on the canvas, four arbitrary points are selected on the canvas to establish their individual numerical models.

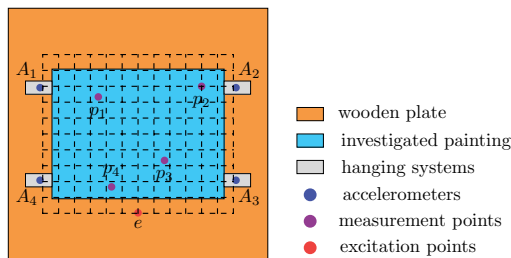


Figure 4.22: An excitation lattice created on the wooden plate and multiple arbitrary measurement points on the canvas.

Assuming that only linear vibration occurs during transport, it is simpler, less time-consuming and more effective to use an impulse signal to test the eigenmodes of the painting than to use other excitation signals (sweep signal, narrowband noise, etc.). In Fig. 3.6, it has shown that the impulse signal generated by an automatic impulse hammer is good for frequencies below 1000 Hz, which fully satisfies the requirements of numerical modeling. Therefore, hammer experiments are first performed at all excitation points on the lattice. Meanwhile, the acceleration responses of all accelerometers and the velocity responses of all measurement points on the canvas are collected at a fixed sampling frequency. The duration of these responses under impulse excitation are usually short, so the sampling time is sufficient when the signal decays to zero. To avoid the influence of fluctuating climate, all hammer experiments should be carried out in a climate box with the same temperature and humidity as during transport.

The step after the hammer experiments is to analyze the data collected from all excitation points, so as to find the optimal numerical modeling scheme, i.e., the minimum number of excitation points and the optimal excitation locations. There are a total of $\binom{143}{n}$ combinations of n ($n \geq 4$) excitation points selected from 143 excitation points. As an example, selecting 4 excitation points from 143 excitation points, a numerical model of

measurement point p_1 on the canvas in the frequency domain can be derived for each combination by Equation (4.52). Then, based on Equation (4.50), each numerical model reconstructs the velocity responses at point p_1 caused by other 139 unselected excitation points. The velocity responses in the time domain can be obtained by inverse Fourier transform. To evaluate the reconstruction results of the numerical model, the mean-square error (MSE) is used throughout. It is defined by

$$\text{MSE} = \frac{100}{N\sigma^2} \sum_{i=1}^N (v_i - \hat{v}_i)^2, \quad (4.53)$$

where v_i is an array of measured velocity and \hat{v}_i is the value of v_i reconstructed by the numerical model; σ is the standard deviation of the measured velocity and N is the number of sample points in the data record. This MSE has the following useful property, if the mean value of the measured velocity is used as a numerical model i.e. $\hat{v}_i = \bar{v}$ for all i , the MSE is 100 %. For each combination, its numerical model has 139 mean-square errors in reconstructing the velocity responses caused by the other 139 unselected excitation points. The average $\overline{\text{MSE}}$ and standard deviation σ_{MSE} of all mean square errors are used as indicators to evaluate the modeling accuracy of the numerical model. Thus, the combination with the smallest average mean-square error and standard deviation is the optimal excitation scheme for 4-point excitation. By analogy, increase the number of excitation points and repeat the above process. As a result, the modeling error of the optimal excitation scheme can be derived for different number of excitation points. The minimum number of excitation points can be determined when the average mean square error and standard deviation converge.

Once the optimal excitation scheme is obtained, a numerical model with the highest accuracy can be established to reconstruct the transport-induced vibration on the canvas. Since it is impossible to collect the velocity response on the canvas during transport, relying on the uniaxial accelerometer on the canvas alone is difficult to provide a sufficient reference. Fortunately, the vibration reproduction results have been demonstrated to have a good accuracy in Section 4.3.4. This thesis intends to evaluate the reconstruction results taking the reproduction ones as a reference. In the laboratory, the velocity at an arbitrary point on the canvas can be observed by an LDV, which is convenient for comparison and evaluation. Therefore, a reproduction experiment should be first performed on the acceleration signals collected from the real transport. The reproduced velocity responses of all measurement points on the canvas are captured. After that, the state of the experiment setup is kept unchanged, i.e., all actuators are still connected to the wooden plate. According to the optimal excitation scheme, a numerical model can be established by hammer experiments. Finally, using this numerical model and taking the original or reproduced acceleration signals as input, the transport-induced vibration at measurement points are reconstructed and compared with the reproduced results. Above are the detailed methodology of reconstructing the transport-induced vibration on the

canvas by numerical modeling. A simplified workflow thereof is provided in Fig. 4.23.

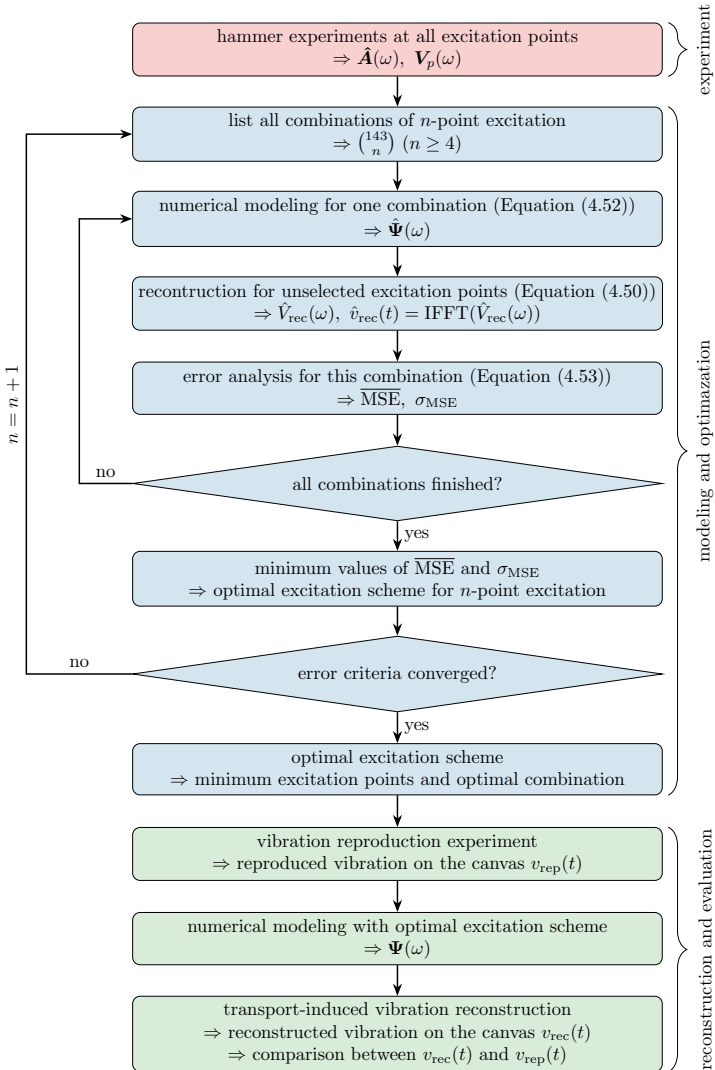


Figure 4.23: Workflow for reconstructing the transport-induced vibration on the canvas by a numerical model.

4.4.3 Experimental Setup and Measurements

The approach of reconstructing the canvas vibration through a numerical model must be experimentally verified for correctness. According to the methodology provided in the preceding section, this section focuses on constructing a corresponding experimental setup. The developed experimental setup is shown in Fig. 4.24. The investigated painting, the wooden plate, and all accelerometers were maintained in the same state as in the vibration reproduction experiments. Again, they were placed inside the climate box with the temperature and humidity adjusted to the same as that during the real transport experiment. Four measurement points, p_1 , p_2 , p_3 and p_4 , were arbitrarily selected on the canvas to build their individual numerical models. The velocity responses at these predefined points were measured with a Polytec PSV-500 scanning LDV. The velocity signals on the canvas as well as the acceleration signals from all accelerometers were collected by the Polytec PSV-500 front-end after passing through a signal conditioner.

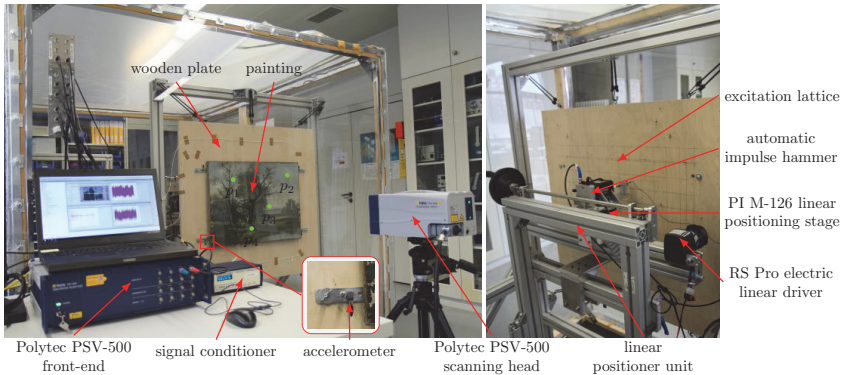


Figure 4.24: The experimental setup used for vibration reconstruction on the investigated painting in the laboratory.

On the backside of the wooden plate, as designed in the previous section, an 11×13 excitation lattice with 6 cm spacing has been inscribed. An electrodynamical shaker of model PCB TMS-K2007E01 plus a tip mechanism were supplied with pulse signals from a function generator to compose an automatic impulse hammer. The automatic impulse hammer should be moved freely on the backside of the wooden plate, so as to give excitation at any position on the excitation lattice. But the experimental operator should avoid entering the climate box as many times as possible to adjust the position of the automatic impulse hammer, otherwise the resulting climate fluctuations will take a long time to stabilize, which will greatly increase the experimental time. To address this problem, a three-dimensional linear positioner unit was constructed. The basic framework

of this linear positioner unit is a hand-cranked vertical lift structure. An additional electric linear driver, model RS PRO 1774519, was mounted on the basic framework to adjust the horizontal position. The range of the vertical lift as well as the horizontal movement covered the range of the excitation lattice. Given the various mounting errors, it is difficult to ensure that the tip of the automatic impulse hammer is always the same distance from the wooden plate when adjusting the excitation position. Therefore, a high-resolution linear positioning stage of model PI M-126.CG1 was installed on the electric linear driver. The automatic impulse hammer was mounted on this linear positioning stage. After adjusting a new excitation position, the distance between the tip of the automatic impulse hammer and the wooden plate was then adjusted by means of the linear positioning stage to ensure that the amplitude of the excitation force is always in the right range. Only an appropriate amplitude of the excitation force can fully excite the model characteristics of the investigated painting in the considered frequency range. Both the electric linear driver and the linear positioning stage were adjusted outside the climate box in ways not described in detail here. Only the vertical position needs to be adjusted each time entering the climate box, which still greatly reduces the experimental time.

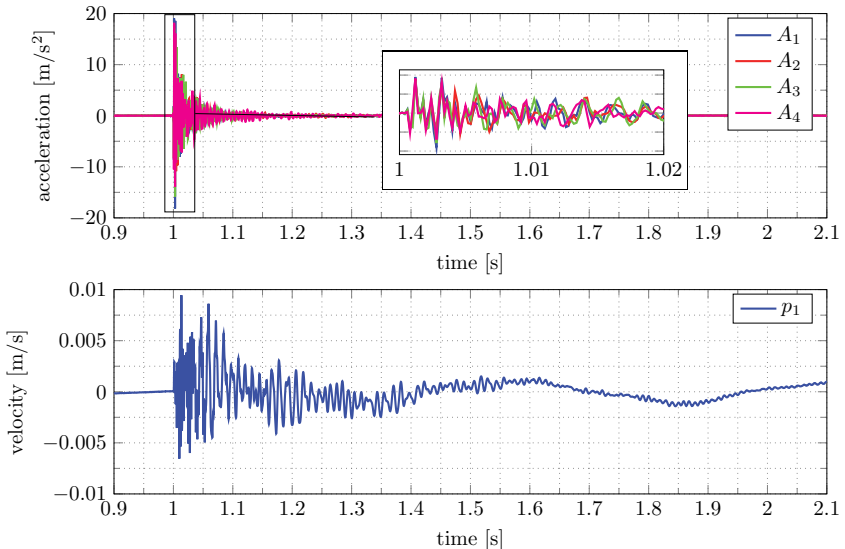


Figure 4.25: The acceleration response and velocity response captured during a single measurement.

All measurements used the same sampling rate $\Delta t = 0.2\text{ ms}$ and measurement time $T = 20\text{ s}$. In Fig. 4.25, the acceleration response of all accelerometers and the velocity

response at measurement point p_1 on the canvas obtained from a single measurement are displayed. The acceleration signals decay to almost 0 after 0.2s. The velocity signal decays a bit slower and due to the effect of the rigid body modes, the rigid body motion does not completely disappear even after 10s. Obviously, it is not necessary to use all the data collected in 20 seconds for analysis. Excessively long data will increase the burden during numerical modeling and its optimization. In order to ensure a sufficient frequency resolution for numerical modeling and vibration reconstruction, the first 10 seconds of all signals are intercepted for subsequent processing.

4.4.4 Numerical Analysis and Model Optimization

In order to establish an optimal numerical model, this section aims to analyze all the measurements. According to the methodology in Section 4.4.2, the modeling errors can be calculated for all the numerical models developed from different excitation schemes. Taking the modeling error as an indicator, the best excitation scheme can be filtered out.

4.4.4.1 Pre-analysis of a Subset

To develop an optimal numerical model for n ($n \geq 4$) points out of 143 points is a computationally intensive task. There are 16701685 possible combinations for the 4-point excitation alone. The computational effort to traverse each combination for numerical modeling and error analysis would be enormous. There is no experience to draw on for guidance on how to select excitation points or tips on which excitation points are better. Therefore, as shown in the left of Fig. 4.26, a subset including 15 points is selected from the excitation lattice. This subset is analyzed with a view to obtain some a priori knowledge, thus reduce the computational effort of finding the optimal combination from a global analysis of the entire excitation lattice.

Following the procedure devised in Fig. 4.23, arbitrary n points from this subset are selected for numerical modeling, while the unselected 143 – n points are used to compute the modeling error $\overline{\text{MSE}}$ and σ_{MSE} . After traversing all the combinations, the modeling errors at different measurement points for the optimal combination of n -point excitation are obtained as shown in the right of Fig. 4.26. As the number of excitation points increases, there is a clear tendency for the average modeling error to decay and converge. Typically, the model accuracy is considered to be very high when the MSE is less than 5 %. For the 4-point excitation, the average modeling error is higher than 10 % even for the optimal combination. It is even higher than 40 % when reconstructing the vibration on the canvas caused by some unselected excitation points. The unselected excitation points with lower errors tend to be close to the selected excitation points. However, when the number of excitation points is increased to 5, the average modeling error decays dramatically to

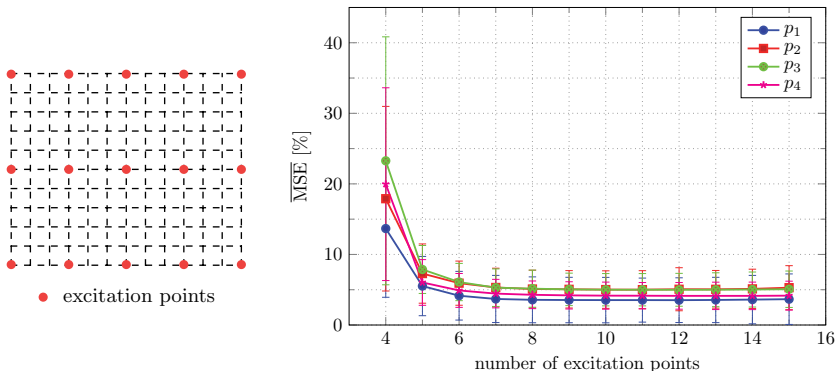


Figure 4.26: A subset from the excitation lattice (left) and the modeling errors of the optimal n -point numerical model in that subset (right).

less than 8 %. Starting from 6-point excitation, the modeling error has begun to converge. From 8-point excitation onwards, a further increase in the number of excitation points no longer significantly improves the quality of the numerical model. This indicates that in Equation (4.52), although 4 excitation points are sufficient to develop a numerical model, the condition number of matrix $(\hat{\mathbf{A}}^T(\omega)\hat{\mathbf{A}}(\omega))^{-1}\hat{\mathbf{A}}^T(\omega)$ is usually larger in this case. The larger the condition number of matrix, the more susceptible the numerical model is to error. Increasing the number of excitation points is one of the effective measures for improving the condition number of matrix. Figure 4.27 illustrates the average condition numbers of matrix $(\hat{\mathbf{A}}^T(\omega)\hat{\mathbf{A}}(\omega))^{-1}\hat{\mathbf{A}}^T(\omega)$ for all combinations of different number of excitation points in the considered frequency range. As the number of excitation points increases, the level of the average condition number of matrix decreases significantly, which corroborates the error analysis in Fig. 4.26.

The modeling effect of the numerical model is further illustrated. One reconstruction of velocity response at measurement point p_1 on the canvas is shown in Fig. 4.28. This response is caused by an unselected excitation point and the numerical model is developed by the optimal combination of 8-point excitation. The mean square error of this reconstruction is 4.22 %, which is very close to the average mean square error of the optimal combination of 8-point excitation. It can be seen that the overall reconstruction is very good. The reconstruction on the lower frequency component is particularly impressive, while for the higher frequency component it is slightly lacking.

In Fig. 4.27 it is also found that for n -point excitation the combination whose average condition number achieves a minimum value tends to have a lower $\overline{\text{MSE}}$ as well. This suggests that the correct choice of excitation locations is another measure to improve the condition number of matrix. Therefore, by analyzing the features of both the best and worst

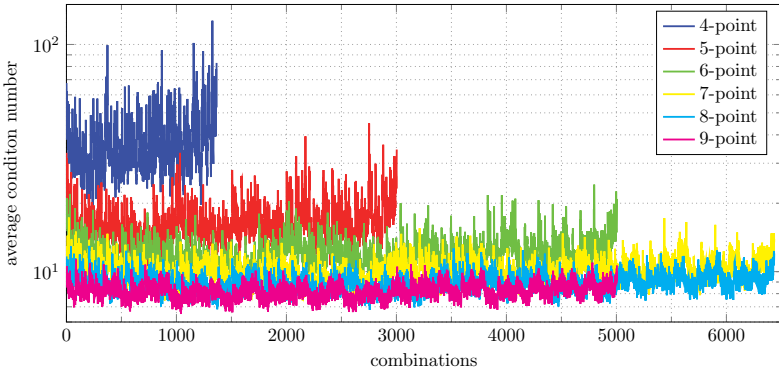


Figure 4.27: The average condition numbers of matrix $(\hat{\mathbf{A}}^T(\omega)\hat{\mathbf{A}}(\omega))^{-1}\hat{\mathbf{A}}^T(\omega)$ for all combinations of different number of excitation points.

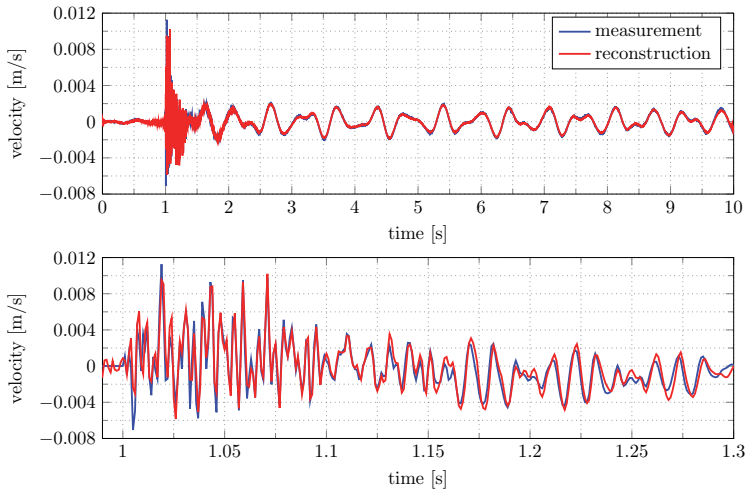


Figure 4.28: The reconstruction for one measurement using a numerical model developed by the optimal combination of 8-point excitation, top: global, bottom: a partial segment.

combinations of excitation locations within the subset, one can facilitate the global analysis for the entire excitation lattice in the next stage. These features can be used to identify and exclude unnecessary combinations, thereby reducing the amount of computation required for analysis. Using the numerical model developed for the measurement point p_1 on the canvas as an example, the first three optimal combinations of excitation locations

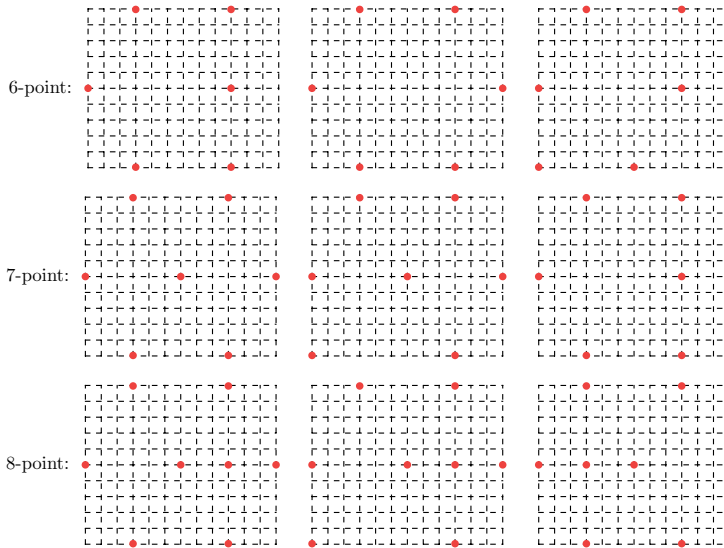


Figure 4.29: The top three optimal combinations of excitation locations for different number of excitation points in the subset.

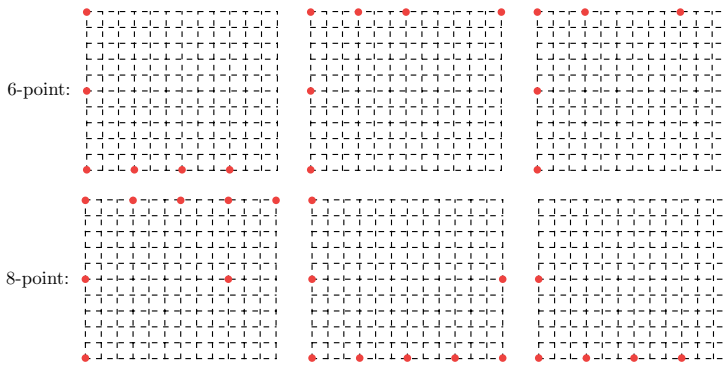


Figure 4.30: The worst three combinations of excitation locations for different number of excitation points in the subset.

for the 6-point, 7-point and 8-point excitation within the subset are listed in Fig. 4.29. Similarly, in Fig. 4.30, the worst three combinations of excitation locations for the 6-point and 8-point excitation within the subset are shown. Besides the listed combinations, many

other combinations have similar $\overline{\text{MSE}}$ values but are not presented here. It is reasonable to speculate that the numerical models developed by them should theoretically have the same accuracy, but differences arise due to various experimental errors.

As can be seen from Figs. 4.29 and 4.30, the better combinations feature excitation locations that are generally more widely distributed across the canvas, rather than clustered within a few adjacent rows or columns. When more than half of the excitation locations are concentrated in a single row or column, the numerical model established by that combination is usually less accurate. Interestingly, axisymmetric combinations consistently form a significant proportion of the optimal combinations. Unlike irregular combinations, axisymmetric combinations are both universal and practical, offering a straightforward approach to perform a global analysis of the excitation lattice by focusing on the optimal axisymmetric combinations. Therefore, to reduce the computational effort in the global analysis of the excitation lattice, the following three guidelines have been developed to identify the necessary combinations:

- each combination should be symmetric with respect to the symmetry axis of the excitation lattice;
- no more than half of excitation locations may be in same row or column;
- all excitation locations must avoid clustering in any small area consisting of 6 adjacent rows or 6 adjacent columns.

4.4.4.2 Global Analysis of Excitation Lattice

Filtering the combinations from the entire excitation lattice using three guidelines outlined in the preceding section significantly reduces computational effort compared to the original. For instance, the number of combinations to be traversed for the 4-point excitation is reduced from 16701685 to 12925. Hence, again following the procedures devised in Fig. 4.23, a global analysis is performed on the the combinations filtered from the entire excitation lattice. Figure 4.31 takes the measurement points p_1 and p_4 on the canvas as examples to show a comparison of the modeling error of the optimal combinations for n -point excitation within the subset and the global analysis. The global analysis further enhances the modeling accuracy of the numerical model. This improvement is most notable with the 4-point excitation, where the model error $\overline{\text{MSE}}$ and σ_{MSE} both see significant reductions. As the number of excitation points increases, the improvement in $\overline{\text{MSE}}$ continues to diminish, e.g., for the measurement point p_4 on the canvas, the modeling error for the optimal combination of 8-point excitation is only reduced from 4.28 % to 4.11 %. In contrast, σ_{MSE} consistently maintains a significant improvement, which indicates that the optimal combination obtained from the global analysis is more universal.

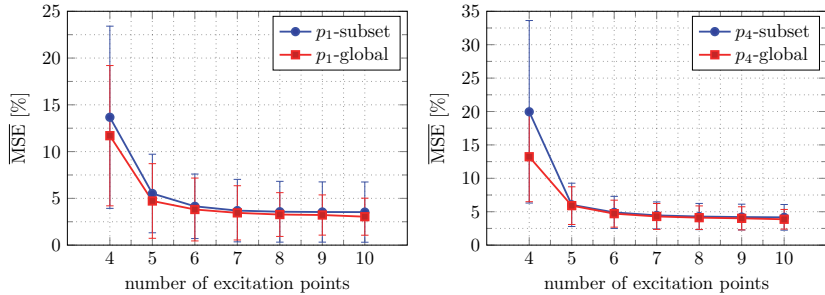


Figure 4.31: The modeling errors at points p_1 (left) and p_4 (right) on the canvas for n -point numerical model developed by the optimal symmetric combination in the excitation lattice.

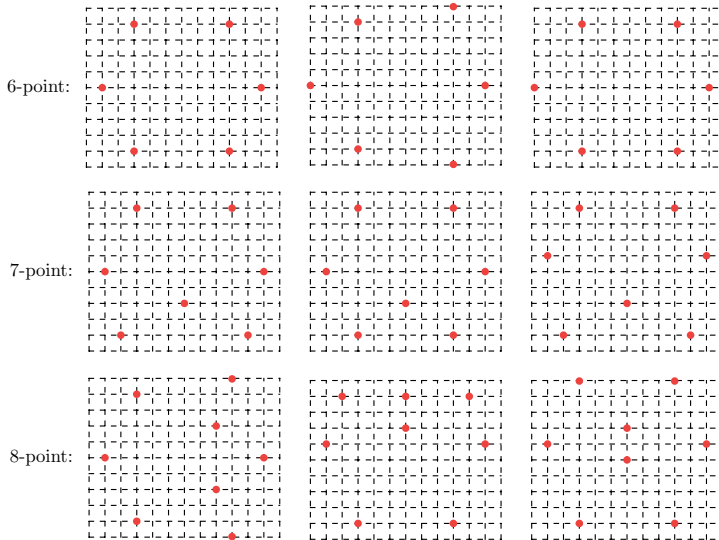


Figure 4.32: The top three optimal combinations of excitation locations for different number of excitation points in the global analysis.

Based on the results of global analysis, the distribution of excitation locations for the optimal combinations can be determined. Still taking the numerical model developed for the measurement point p_1 on the canvas as an example, the first three optimal combinations of excitation locations for the 6-point, 7-point and 8-point excitation within the entire excitation lattice are illustrated in Fig. 4.32. It is important to note that within the

global analysis, for each n -point excitation, there exist more combinations that have nearly identical modeling accuracy. For example, the numerical model at measurement point p_1 on the canvas developed with the optimal combination of 8-point excitation has a modeling error of $\overline{\text{MSE}} = 3.27\%$ and $\sigma_{\text{MSE}} = 2.34\%$. In contrast, the subsequent 1000th combination has a modeling error of $\overline{\text{MSE}} = 3.48\%$ and $\sigma_{\text{MSE}} = 2.71\%$. Their errors are so similar that they can be considered to have nearly the same modeling effect.

Moreover, as the modeling error approaches convergence, it is observed that the optimal combination for one measurement point on the canvas yields good modeling accuracy across other points as well. Specifically, an optimal combination of n -point excitation ($n \geq 6$) tends to be universally effective. For instance, the optimal combination of 8-point excitation at measurement point p_1 on the canvas mirrors the optimal combination at measurement point p_4 . Beside that, considering the modeling error at measurement point p_2 and p_3 , the numerical models developed by this combination yield an $\overline{\text{MSE}}$ of 4.92% and σ_{MSE} of 2.24% at p_2 , and an $\overline{\text{MSE}}$ of 4.96% and σ_{MSE} of 2.57% at p_3 . Comparatively, the minimum modeling errors observed at p_2 is an $\overline{\text{MSE}}$ of 4.82% with σ_{MSE} of 2.2%, and at p_3 , an $\overline{\text{MSE}}$ of 4.83% with $\sigma_{\text{MSE}} = 2.06\%$. Thus, in practical scenarios, using the optimal combination for one measurement point on the canvas to establish a numerical model for any other arbitrary point proves beneficial, offering time and effort savings at the expense of only a slight reduction in accuracy.

To summarize, the characteristics of the best excitation combinations are informed by the subset analysis. This analysis is followed by a thorough examination of the entire excitation lattice to identify the optimal combinations of n -point excitation. These optimal combinations will then be employed in the subsequent step to reconstruct the transport-induced vibration on the canvas.

4.4.5 Vibration Reconstruction Results

Due to the challenge of obtaining sufficient vibration data on the canvas directly from the real transport experiment, the vibration reconstruction results lack a primary reference. However, as highlighted in Section 4.3.4, the accuracy of vibration reproduction has been validated. Therefore, a comparison between vibration reconstruction and vibration reproduction is conducted to assess the quality of the numerical model.

Following the methodology outlined in Section 4.4.2, a vibration reproduction experiment was first performed to gather the acceleration data on the strainer and the velocity data at all measurement points on the canvas. To maintain consistency in the modal characteristics of the investigated painting, all actuators and the wooden plate remained connected. As detailed in Section 4.4.4.2, the modeling error has converged with 8-point excitation, leading to the selection of its optimal combination at measurement point p_1 for numerical modeling. Hammer experiments were then executed at corresponding locations on the

excitation lattice to record acceleration data on the strainer and velocity data at all measurement points. This process enables the development of a numerical model for any measurement point, as described in Equation (4.52). As an example, the numerical model developed for measurement point p_1 on the canvas in the frequency domain is shown in Fig. 4.33, highlighting only the components below 100 Hz. The peaks of this numerical model on each component may indicate where the eigenfrequencies of the investigated painting are located. Notably, for real paintings, the relationship between the vibration on the strainer and the vibration at arbitrary point on the canvas is quite complex. It is challenging to express them mathematically, thus the use of a numerical model provides a more effective approach.

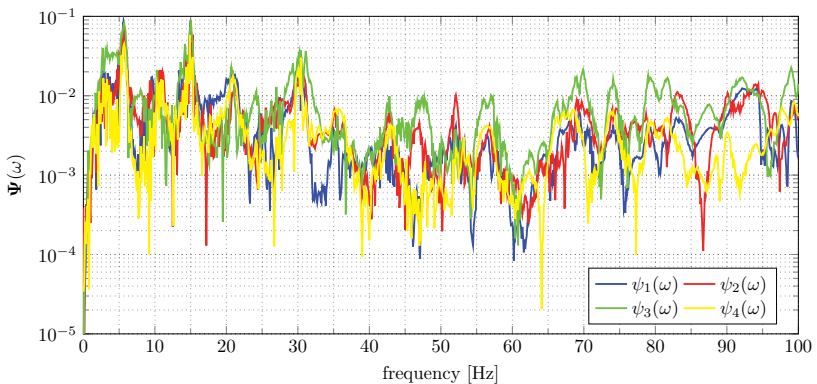


Figure 4.33: The numerical model established for the measurement point p_1 on the canvas by the optimal combination of 8-point excitation.

The acceleration data on the strainer collected from the vibration reproduction experiment is used as input for the numerical model. Then the transport-induced vibration on the measurement point p_1 can be reconstructed using the numerical model developed for this point. A comparison of the reconstruction and reproduction results for a small segment of the signal is shown in Fig. 4.34. Despite a slight error, the overall reconstruction results agrees with the reproduction results. For a reproduction signal of up to 740 seconds, the mean square error of reconstruction results is 12.2%. It is larger than the average mean square error of the optimal numerical model in Section 4.4.4.2, but the accuracy of such vibration reconstruction is still quite good considering various factors such as noise interference, climate fluctuations, and so on.

Moreover, a conclusion is drawn in Section 4.4.4.2 that the optimal combination of n -point excitation ($n \geq 6$) is generally effective across other measurement points on the canvas. To verify this conclusion, the aforementioned optimal combination of 8-point excitation

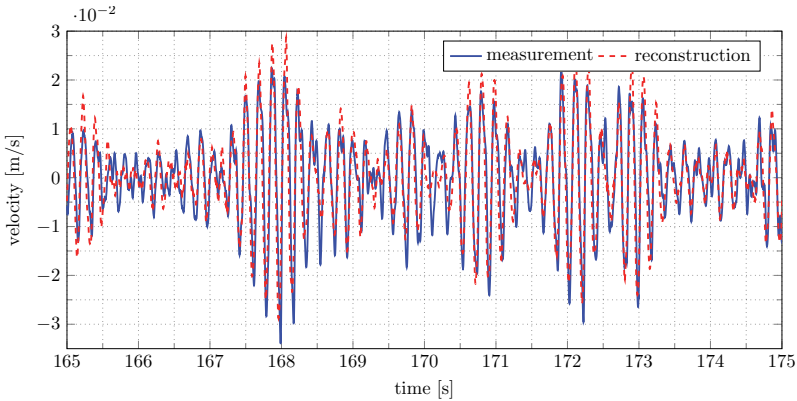


Figure 4.34: Transport-induced vibration reconstruction results at the measurement point p_1 using the optimal numerical model of 8-point excitation.

used at measurement point p_1 is applied to develop a numerical model for measurement point p_3 . This numerical model are used to reconstruct the transport-induced vibration at measurement point p_3 . Consequently, as shown in Fig. 4.35, a small segment of reconstructed signal is compared to the corresponding reproduced signal. Obviously, the overall behavior is again represented well by the reconstruction results, which is a strong proof of the universality of the optimal combination.

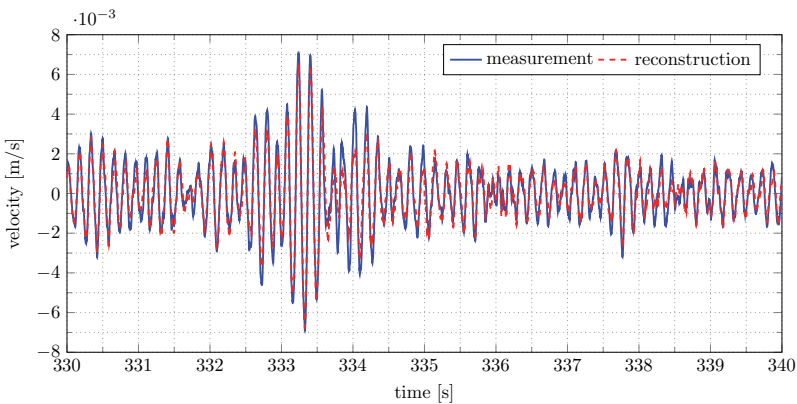


Figure 4.35: Transport-induced vibration reconstruction results at the measurement point p_3 using the numerical model developed by the optimal combination at p_1 .

All in all, the transport-induced vibration reconstruction on the canvas by means of numerical model has fully achieved the expected results. Since the optimal combinations of excitation are known, it simplifies and increases the efficiency of vibration reconstruction in practical applications. Although it may be slightly less accurate than direct vibration reproduction, vibration reconstruction serves as a more accessible alternative, offering a useful reference to the unknown vibration on the canvas during transport.

Chapter 5

Nonlinear Dynamic Behavior of Paintings

Both the study on the modal characteristics of paintings in Chapter 3 and the simulation of transport-induced vibration in Chapter 4 follow a hypothesis that since the vibration displacement is small, paintings can be treated as a linear system during transport, i.e., their model parameters are always considered constant. Not limited to the work in this thesis, many other works on the transport of paintings upholds this linear hypothesis [LäuchliEtAl14, KrachtKletschkowski17, Palmbach07, TornariTsiranidouBernikola14, WeiKragtVisser05, ChiribogaArroyo13]. However, some researches have shown that the modal characteristics of paintings are not only affected by climate [Michalski91, Mecklenburg82, HaganEtAl09], but also vary with different vibration intensities [Kracht11, Hartlieb21]. These researches indicate that there are nonlinear aspects in the modal characteristics of paintings, and the linear hypothesis remains to be checked. Therefore, in order to provide a more in-depth insight into the modal characteristics of paintings, it is essential to examine the nonlinear dynamic behavior of paintings. Furthermore, for the purpose of improving the packaging system so as to protect the painting from potential damage during transport, it is of great significance to investigate whether the modal nonlinearities of paintings occur during transport and whether these modal nonlinearities need to be accounted for in the design of the packaging system. The modal characteristics of paintings as affected by climate have been thoroughly discussed in Section 3.4. Moreover, most of the current packing cases have been equipped with a fire-retardant climate box that guarantees constant temperature and humidity conditions inside the packing case. Thus, in this chapter, an investigation will be focused on the modal nonlinearities of paintings when being subjected to different intensities of shock and vibration excitation during transport.

There have been few researches on the modal nonlinearities of paintings under different vibration intensities in the last decades. In [Hartlieb21], it was discovered that the resonance

frequencies vary with the excitation intensities when testing the eigenfrequencies of canvases with different materials. In [Kracht11], a detailed research about the modal nonlinearities of paintings was carried out. Sweep experiments were conducted in [Kracht11] to simulate the vibration of paintings. Experimental results showed that the canvas exhibited strong progressive stiffness characteristics and degressive damping characteristics. That is, with the increase in the external excitation, the resonance frequencies of paintings increase, and the amplitudes of resonance peaks decrease. It was also mentioned in [Kracht11] that the resonance peaks are asymmetric, and the resonance peaks obtained by up-sweep and down-sweep, i.e. sweep with increasing and decreasing frequency, respectively, are different. These nonlinear phenomena were explained and discussed in [Kracht11] in terms of the Duffing oscillator model. However, whether these nonlinear phenomena occur during transport and whether the design of packaging systems needs to take these nonlinear factors into account has not yet been examined. Moreover, paintings are subjected to not only vibration excitation but also shock excitation during transport, which means that a general conclusion about the modal nonlinearities of paintings under different types of excitation deserves a further investigation.

Based on the above motivation, in order to simulate the excitation that paintings receive during transport, hammer experiment and sweep experiment are adopted in this thesis. The hammer experiment is realized by an automatic impulse hammer which is used to simulate a shock excitation on the painting during transport. The sweep experiment is realized by an electrodynamical shaker, as well as a loudspeaker. They are used to simulate the vibration excitation on the painting during transport. Both the hammer and sweep excitation differ from the nondeterministic excitation occurring during a real transport. However, they represent limit cases that are clearly defined and can easily be compared for different measurements. Besides, narrowband noise is used to simulate the random excitation on the painting during transport, and the nonlinear output frequency response functions (NOFRFs) are identified for the painting to detect the presence of nonlinearities. For simplifying the analysis of measurement results, even the method developed in Chapter 4 for simulating the transport-induced vibration was also not applied here. Since the aim is the evaluation of nonlinear behavior, a simple axial excitation is chosen instead of a multi-axial excitation. This allows to directly relate excitation amplitude with (possibly nonlinear) response. The excitation is chosen perpendicular to the painting plane for nonlinear effects are more likely to occur in this direction. In order to avoid excessive excitation amplitudes, these are chosen in the range which was recorded during real transports [HeinemannEtAl19, GaoEtAl23a].

In an effort to draw a general conclusion about the modal nonlinearities of paintings, two real paintings with natural aging and a recently manufactured dummy painting are tested in this chapter. The two real paintings are of negligible artistic value, and thus, they can be tested under lab conditions. The dummy painting was made by an experienced art conservator, with uniform tension and uniform and homogeneous distribution of primer

and paint. It does not yet show any deterioration in terms of aging. In all experiments, the vibration accelerations on the strainer of three investigated paintings are collected. Besides that, the vibration velocities and vibration displacements at selected measurement points on the canvases are also captured together. The vibration velocity on the canvas is combined with the corresponding excitation force to calculate the frequency response function (FRF), from which the modal nonlinearities can be analyzed. The vibration displacement of the canvas can intuitively express the vibration intensity of the investigated paintings. The vibration acceleration on the strainer is compared with those recorded during real transports, which is then used to assess whether the modal nonlinearities occur during transport. According to all experimental results for three investigated paintings, the general behavior of modal nonlinearities under different intensities of shock and vibration excitation are summarized. Consequently, a conclusion of whether the modal nonlinearities of paintings should be considered during transport is derived.

This chapter is divided as follows. Section 5.1 contains a description of the experimental setup used to test the modal nonlinearities of paintings, and shows some measurement results. Through a short introduction to different experimental results, Section 5.2 discusses whether paintings can be treated as a linear system during transport. Subsequently, in Section 5.3, the general behavior of modal nonlinearities for three investigated paintings is summarized and their possible consequences for transport are discussed. Finally, the methods used to identify the nonlinear dynamic behavior of paintings in the laboratory are summarized in Section 5.4. This chapter follows the findings published in [GaoEtAl22] while enhancing the methodology for determining the presence of modal nonlinearities in paintings during transport.

5.1 Experimental Setup and Measurements

Three different paintings are investigated in this chapter to explore their nonlinear dynamic behaviors. The first painting shows a seascape, and the second is a still life painting. Their specific information can be found in Section 2.2. Both of them are real paintings, though of negligible artistic value, and have become fragile and massively damaged after natural aging. The purpose of studying two real paintings simultaneously is to discover the similarities and the differences in modal nonlinearities between real paintings. The last painting is the dummy painting D bearing the logo of the author's institute, details of which can be found in Section 2.1.3. In contrast with the real paintings which were built, primed, painted etc. by the artist and were also left in the pre-tension state as of purchase/loan, the purpose of the dummy painting is to set up an intentionally simplified dummy model in order to assess whether some of the observed properties change with those simplifications. Because the dummy painting has only been dried for less than a month, there is almost no deterioration in terms of aging. Through in the research related

to this dummy painting, the similarities and differences in modal nonlinearities between the real paintings after natural aging and the young painting can be discovered. Each investigated painting was equipped with four perforated metal plates, which are used to simulate the state of the painting being fixed on a transport crate, and also to facilitate the hanging of the painting in the laboratory.

Figure 5.1 depicts the experimental setup used to study the modal nonlinearities of the investigated paintings. It consists of three investigated paintings, three different excitation mechanisms, a Polytec VibroFlex Laser Doppler Vibrometer (LDV), three triaxial accelerometers and a climate box. The investigated painting was mounted with rubber bands on an aluminum support, forming a very soft suspension which can be approximately considered as a free suspension. Although the described suspension differs from the typical boundary conditions during transport, the vibration of the painting (and the paint layer) could still be generated to be essentially the same as for a real transport, if multidimensional excitation forces were produced such that the multidimensional accelerations measured in the laboratory were the same as measured during the real transport. As long as the desired motion of the investigated painting is generated, the difference in boundary conditions has no negative impact on the measurements. Three triaxial accelerometers were attached on the perforated metal plates in order to monitor the acceleration of the investigated painting and compare it with the vibration acceleration recorded during the real transport experiments in [HeinemannEtAl19, GaoEtAl23a]. The model of the triaxial ICP accelerometers is PCB-356A03/NC.

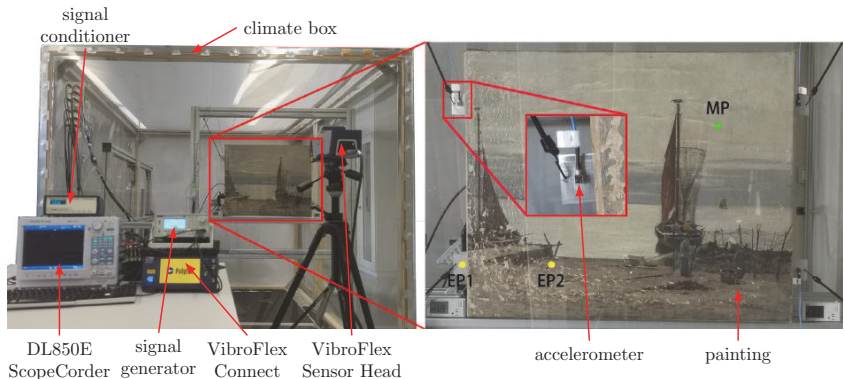


Figure 5.1: Experimental setup built for the investigation of modal nonlinearities of paintings inside a climate box in the laboratory.

In principal, a mobility measurement would have to be performed for many points to fully capture the spatially distributed motion of the paint layer and to also fully evaluate the

spatial distribution of nonlinearities. However, measurements conducted at different points on the canvas revealed similar results as to the extent of nonlinear behavior. Therefore, for simplicity, the green point labeled MP on the investigated painting shown in Fig. 5.1 was selected as a representative point to present the experimental results in this chapter. In order to avoid the loss of modal information during the experiment due to the measurement point being located on one of the nodal lines of the first eight eigenmodes, this measurement point was selected at one fourth of the width and height of each investigated painting. The seascape painting is less damaged at this point, while the still life painting has obvious cracks at this point. The vibration velocity signals at measurement points were measured with a Polytec VibroFlex LDV. The VibroFlex LDV has the advantage of using a CO₂-based Laser source and a multiple channel interferometer which virtually avoids laser drop outs even when measuring uncooperative surfaces. Rigorous inspection of the measurement signals in time domain revealed no laser drop outs. Velocity and displacement on the measurement points were measured simultaneously.

To test the nonlinear dynamic behavior of paintings, three different types of excitation were adopted for experimental research. The first type of excitation is an impulse excitation generated by an automatic impulse hammer as shown in the left of Fig. 5.2. The automatic impulse hammer is composed of an electrodynamical shaker and a modified tip mechanism that generates a very short hit and avoids double hits. The impulse excitation directly acted on a metal plate on the investigated painting from the back, which was used to simulate the shock excitation to the painting during transport. The excitation point is shown as the yellow point labeled EP1 in Fig. 5.1. The contact force between the excitation point on the investigated painting and the tip of the automatic impulse hammer was measured by an ICP force sensor of model PCB 086E80. The excitation was chosen such that measured acceleration covers the acceleration range measured for shock events in real transport.



Figure 5.2: Three different excitation mechanisms used for experimental research on the modal nonlinearities of paintings, left: automatic impulse hammer, middle: sweep shaker, and right: sweep loudspeaker.

The second type of excitation is the sweep excitation generated by an electrodynami-

cal shaker or a loudspeaker. The sweep excitation was used to simulate the vibration excitation to the painting during transport. When the excitation was generated by an electrodynamical shaker, the excitation position was the same as for the hammer experiment on the strainer, but the brass stinger of the shaker was firmly connected to the perforated metal plate with two nuts as shown in the middle of Fig. 5.2. The input force of the shaker was measured by an ICP force sensor of model PCB 208C01. In order to obtain a realistic excitation intensity, root mean square values of acceleration responses on the painting strainer as measured in [HeinemannEtAl19, GaoEtAl23a] were used. When the excitation was generated by a loudspeaker, the loudspeaker was simply faced to the investigated painting in a distance of round about 1 cm, as shown in the right of Fig. 5.2. This contactless experimental method is particularly suitable for measuring the modal nonlinearities of real precious paintings. However, because the input pressure generated by acoustic excitation is difficult to measure, the modal nonlinearities of investigated paintings can only be analyzed and evaluated based on the velocity response on the canvas instead of the mobility which would require a force or pressure measurement.

The last type of excitation is narrowband noise, which used the same equipment as the sweep excitation. It was used to simulate the indeterministic excitation to the painting during transport. The signals required for each of these excitation mechanisms were provided by a function generator, and the excitation intensity were adjusted by the input voltage. In order to avoid the influence of changing climate on the modal characteristics of investigated paintings as much as possible, all experiments were carried out in a self-designed climate box. The potential relative humidity adjustment range of the climate box is 35 %-90 %, while $52.5\% \pm 0.4\%$ was used for the experiments if not separately mentioned, and the temperature was kept constant at 22°C. In this range, the changes in modal characteristics caused by changing climate have been checked to be negligible.

All measurement signals were amplified using a signal conditioner and recorded by a Yokogawa ScopeCorder of model DL850E. The acceleration response on the strainer was sampled at a rate of 1 kHz, while the velocity response on the canvas was sampled at a rate of 20 kHz. The measurement duration for hammer experiments was set to 10 seconds, and for sweep experiments, it was extended to 100 seconds. Since the excitation force, the acceleration response on the strainer, and the velocity response on the canvas under pulse excitation have been discussed in Chapters 3 and 4, here only the excitation force and the velocity response for a single measurement under up-sweep excitation are shown in Fig. 5.3. In the velocity response, three red dashed lines indicate the time when the first three resonant frequencies occur. These resonance peaks exhibit varying degrees of asymmetry in the time domain, suggesting the presence of nonlinear characteristics. Signals in the time domain provide rather limited information, and, therefore, they must be converted to the frequency domain for more in-depth research.

The vibration velocity on the canvas and the excitation force were collected to study the

modal nonlinearities of investigated paintings, i.e. so-called mobilities were measured. To rule out misinterpretations by leakage effects due to finite measurement time, different window functions were applied to the time domain signal. Among others, a Bartlett and a Von Hann window were used for the sweep experiments and an exponential window was used for the impact experiments. In the frequency range of interest, apart from the most subtle differences, the mobilities were identical. Also, coherence was checked to evaluate the quality of measurement. No detrimental effects were found.

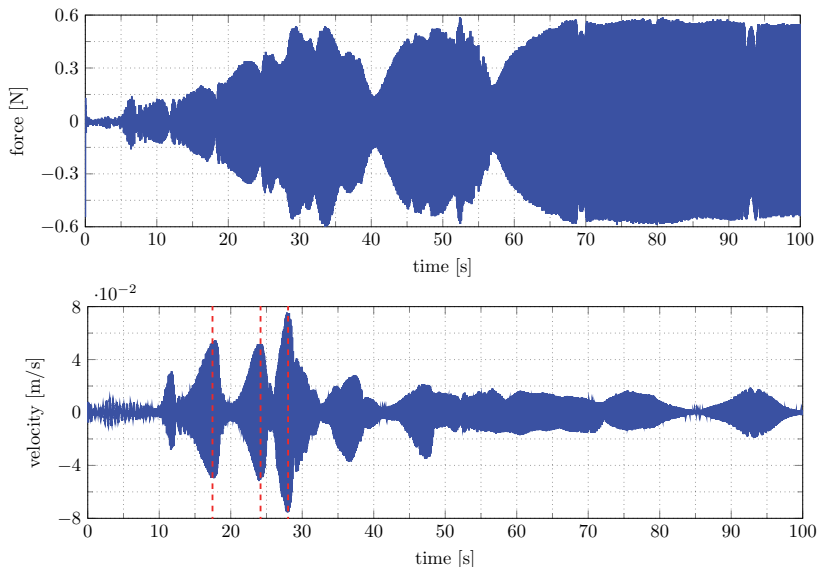


Figure 5.3: Excitation force and velocity response on the canvas of a single measurement under up-sweep excitation, top: excitation force, bottom: velocity response.

5.2 Identification of Nonlinear Dynamic Behavior

In the following, the nonlinear dynamical behaviors of the three investigated paintings under varying excitation levels are identified by different types of experiments. By comparing the shock and the vibration intensity of the investigated painting with that during a real transport in [HeinemannEtAl19, GaoEtAl23a], it is clarified that the dynamical behaviors of paintings observed in the laboratory covers the dynamical range that occurs during transport. This analysis allows for a subsequent determination of whether the painting can be treated as a linear system during transport.

5.2.1 Hammer Experiment with Excitation on the Strainer

The first experiment is realized by an automatic impulse hammer exciting the strainer of the three investigated paintings. This simulates the shock excitation during transport, so as to study the influence of different shock intensities on the modal characteristics. During the experiment, the mobility

$$Y(\omega) = \frac{V(\omega)}{F(\omega)} \quad (5.1)$$

at the measurement point MP is calculated with the Fourier transformed velocity response $V(\omega)$ at the measurement point and the Fourier transformed excitation force $F(\omega)$ at the excitation point EP1.

Figure 5.4 depicts the experimental results of the mobilities at the measurement point for different hammering forces applied to the strainer of the seascape painting. Due to the possible nonlinear dynamical behavior, the concept of eigenfrequency is no longer applicable, and therefore the peaks identified in the spectrum are henceforth referred to as resonance peaks, and their corresponding frequencies as resonance frequencies. The identified first resonance frequency of the seascape painting is about 7.83 Hz. All the peaks below 7.83 Hz are detected as the rigid body modes of the painting, i.e. the undeformed painting vibrates relative to the aluminum support. The strong consistency of the mobility curves at different hammering forces is a corroboration of the rigid body modes. With respect to the structural eigenmodes of the painting, it can be clearly observed that the corresponding resonance frequencies do not change with the changing hammering force intensities. For the lower modes, the amplitude of the resonance peaks remains stable across various hammering forces. In contrast, the amplitude of the resonance peaks in some higher modes fluctuates significantly. This behavior can be attributed to the soft suspension, which causes considerable rigid body motion in the painting under higher hammering forces. As a result, part of the excitation force may not effectively excite the painting's eigenmodes. Moreover, despite their different modal characteristics, the still life painting and the dummy painting D have also shown the same general behavior, i.e. their modal characteristics did not change for different shock intensities.

Limited by the maximum input voltage of the automatic impulse hammer, the maximum hammering force that can be achieved on the strainer of the seascape painting is about 22 N in a contact time of 10 ms. Within this range of hammering force, the maximum acceleration measured on the strainer is about 13 g ($1\text{ g} \approx 9.8\text{ m/s}^2$). Since during the real transports in [HeinemannEtAl19, GaoEtAl23a], the maximum acceleration on the strainer caused by the shock excitation does not exceed 1 g, the maximum shock intensity of the seascape painting during the hammer experiment is much higher than that during the real transport. For the still life painting and the dummy painting D, their real transport data are not available. However, similar accelerations were measured for the still life painting and the dummy painting D in the laboratory experiments. The weight of the still life

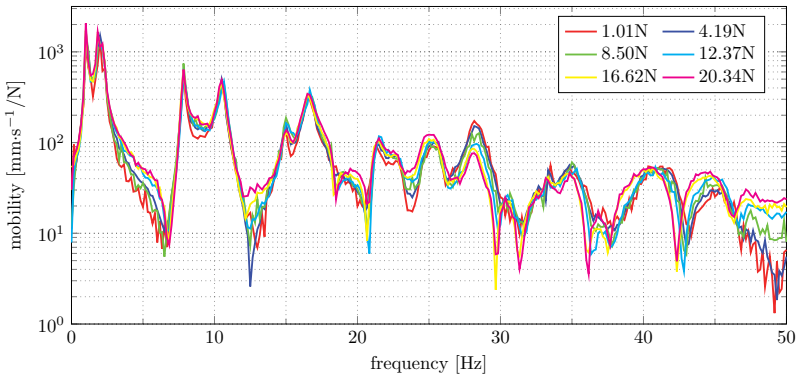


Figure 5.4: Mobilities of the measurement point obtained by applying different hammering forces to the strainer of the seascape painting.

painting is comparable to the seascape painting, while the weight of the dummy painting D is roughly twice as heavy as the seascape painting. Despite this, the measured acceleration in the hammer experiment exceeds those of the seascape painting during the transport by a factor of 10. Consequently, it can be concluded that the modal characteristics of the three investigated paintings observed in this hammer experiment encompass the modal characteristics they would experience when being subjected to shock excitation during a real transport.

In summary, the modal parameters of the investigated paintings remain consistent even under shock excitations much higher than those encountered during a real transport. Therefore, the hammer experiment on the strainer supports the hypothesis that the painting can be treated as a linear system when being subjected to shock excitation.

5.2.2 Sweep Experiment with Excitation on the Strainer

Subsequently, the sweep experiment using an electrodynamic shaker was carried out on the strainer of three investigated paintings, with the aim of simulating the different intensities of vibration excitation suffered by the painting during transport. The frequency range of the sweep excitation extended from 1 Hz to 55 Hz, and was performed with a constant sweep rate in a sweep duration of 100 seconds. In order to guarantee that the excitation used could be considered as a quasi-static excitation with no eminent transient effects, experiments with up to five times slower sweep rates were conducted with no apparent changes in the measurement results. To avoid misinterpretation in terms of nonlinearity, the input force was evaluated in terms of harmonics. The second harmonic turned out to be suppressed by more than 30 dB and higher harmonics were suppressed at

least 36 dB for the full frequency range of interest.

Similar to the hammer experiment on the strainer, the mobilities at the measurement point under different vibration intensities are analyzed. The measured mobilities appear to be very noisy and littered with additional peaks. A thorough analysis turned out that this is not caused by an improper measurement setup (bad signal-to-noise ratio, etc.), but it was found to be caused by harmonics and their influence on the mobility when calculated according to Equation (5.1). Those effects will be discussed in more detail later. Based on Equation (3.5), estimating the mobilities by means of calculating the auto spectrum and the cross spectrum of excitation force and velocity response can improve the quality of the curves. In Fig. 5.5, the mobility spectrum of the seascape painting under different sweep intensities in an entire sweep range is shown, but a moving average filter with a window length of 10 samples was used to smooth the mobilities. Different sweep intensities are denoted by L_1, L_2, \dots, L_{12} , where L_1 represents the lowest sweep intensity of 0.0664 N (peak to peak value) at 50 Hz and L_{12} represents the highest sweep intensity of 4.69 N (peak to peak value) at 50 Hz.

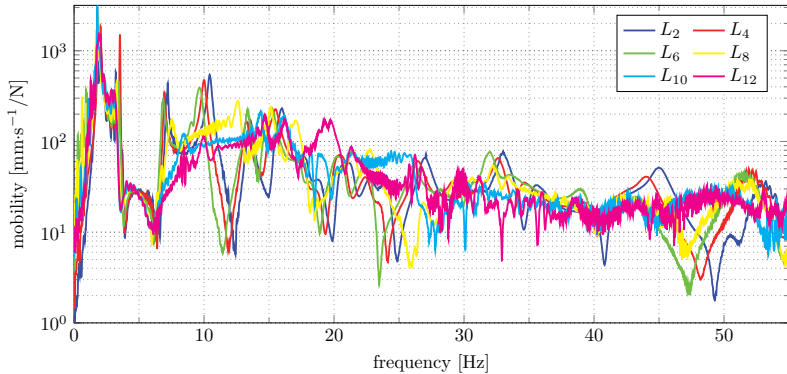


Figure 5.5: Mobility spectrum at the measurement point obtained by applying different intensities of up-sweep excitation to the strainer of the seascape painting.

In Fig. 5.5, the resonance peaks of the first eigenmode are identified around 7 Hz. Below 7 Hz, the resonance peaks do not change with different sweep intensities, and hence they are identified as rigid body modes. Above 7 Hz, the resonance peaks of each eigenmode are different under different sweep intensities, which clearly indicates that the seascape painting exhibits considerable modal nonlinearities. For the reasons mentioned above, the analysis of modal nonlinearities above 20 Hz is almost impossible. Below 20 Hz four resonance frequencies are found which are used in the following to investigate the modal nonlinearities to more detail. Figure 5.6 presents the mobilities in a reduced frequency range in separate plots for smaller and stronger sweep intensities. The resonance frequencies first decrease

slightly with increasing intensities, see the left side of Fig. 5.6, and then increase sharply with increasing intensities, see the right side of Fig. 5.6. In particular, the first and second resonance frequencies at higher sweep intensity even rise to the positions of the second and third resonance frequencies at lower sweep intensity, respectively. Another observation is that the amplitude of each resonance peak decreases with increasing sweep intensities. When the sweep intensity is high enough, the resonance peak even becomes relatively flat and difficult to identify. Qualitatively, similar behavior was observed for the still life painting and the dummy painting D. For the lack of fundamentally different insight, these results are not provided here.

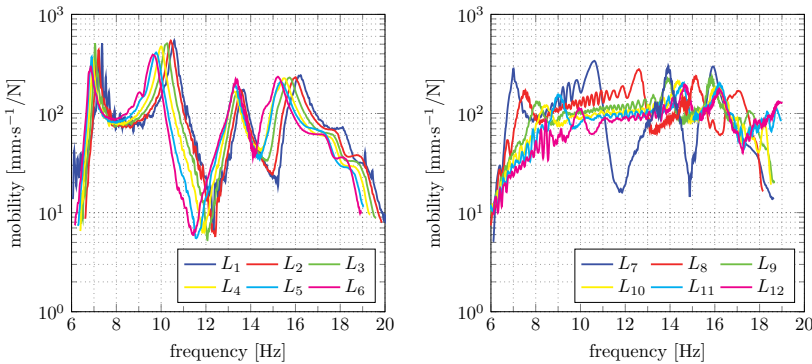


Figure 5.6: Changes in the resonance peaks of the first four eigenmodes at the measurement point when up-sweep excitations of different intensities are applied to the strainer of the seascape painting, left: lower intensities, right: higher intensities.

Although it is known that there are modal nonlinearities in paintings, it is still unknown whether they will show an effect during transport. For this reason, a comparison of the vibration intensity of the seascape painting between the sweep experiment and a real transport is carried out. Table 5.1 lists the statistics of the vibration acceleration on the strainer during an entire transport experiment in [HeinemannEtAl19], as well as the lowest intensity sweep experiment (L_1) and the highest intensity sweep experiment (L_{12}). A direct comparison is difficult because the excitation during transport is quasi-random, which is different from the constant intensity sweeps in the laboratory. Besides, the vibration during transport always originated from three dimensional excitation, whereas the uniaxial excitation was used during the sweep experiment. To address this issue, only the acceleration component perpendicular to the painting plane, i.e., the z -axis component a_z , is considered and split into three categories: $a < 0.1 \text{ g}$, $0.1 \text{ g} \leq a < 0.5 \text{ g}$, and $a \geq 0.5 \text{ g}$. Table 5.1 displays the percentage distribution of the acceleration signals recorded on the strainer of the seascape painting across these three intervals during the entire

transport experiment and for the lowest (L_1) and highest (L_{12}) intensity sweep experiments. Additionally, the root mean square (rms) values and the limit values of the acceleration signals are provided. All values indicate that the entire range of the accelerations measured during a real transport is fully captured by the laboratory experiments. Furthermore, based on the mean square value, the vibration intensity of the seascape painting during transport is roughly between the sweep intensities L_6 and L_7 , where its modal characteristics have already undergone obvious nonlinearity. Therefore, it can be concluded that the seascape painting are subject to non-negligible modal nonlinearities due to changes in vibration intensity during transport. The same conclusion must be drawn for the still life painting and the dummy painting D.

Table 5.1: A comparison of the vibration acceleration on the strainer of the seascape painting between a sweep experiment and a real transport experiment. All values are given in $g \approx 9.8 \text{ m/s}^2$.

| acceleration | $a < 0.1 \text{ g}$ | $0.1 \text{ g} \leq a < 0.5 \text{ g}$ | $a \geq 0.5 \text{ g}$ | rms | min | max |
|--------------------------------------|---------------------|--|------------------------|--------|--------|-------|
| $a_z, \text{ transport } [\text{g}]$ | 86.4% | 13.5% | 0.1% | 0.08 | -0.83 | 0.83 |
| $a_{z1}, L_1 [\text{g}]$ | 100% | 0% | 0% | 0.0065 | -0.034 | 0.018 |
| $a_{z2}, L_1 [\text{g}]$ | 100% | 0% | 0% | 0.0087 | -0.047 | 0.039 |
| $a_{z3}, L_1 [\text{g}]$ | 100% | 0% | 0% | 0.0078 | -0.036 | 0.036 |
| $a_{z1}, L_{12} [\text{g}]$ | 68.3% | 27.1% | 4.6% | 0.28 | -1.45 | 1.46 |
| $a_{z2}, L_{12} [\text{g}]$ | 69.6% | 20.6% | 9.8% | 0.40 | -1.46 | 1.50 |
| $a_{z3}, L_{12} [\text{g}]$ | 63.1% | 24.2% | 12.6% | 0.41 | -1.14 | 1.39 |

In short, the sweep experiment reveals that all investigated paintings produce apparent modal nonlinearities during transport. Therefore, the paintings cannot be simply treated as a linear system when being subjected to vibration excitation during transport. This is contrary to the prevalent hypothesis. Even though this conclusion is only verified for the three paintings investigated in this work, a high probability is claimed that this is the case with many other paintings of comparable size and weight. It is even believed that nonlinear effects of a similar extent appear in paintings of other size and weight. The general behavior of the nonlinearities for sweep excitation and their consequences for a real transport will be further analyzed and discussed in the subsequent sections.

5.2.3 Hammer Experiment with Excitation on the Canvas

In the above hammer experiment and sweep experiment, completely different dynamical behaviors of investigated paintings were identified at different excitation intensities. The shock signal has a short action time, and its energy is distributed over a wide frequency

band. Thus, the energy allocated to each eigenmode is very small, resulting in a weak response of each eigenmode. On the contrary, the vibration signal has a long action time, and the energy is concentrated in a small frequency range. As long as the excitation frequency is close to the resonance frequency of a certain eigenmode, a strong response of this mode will be triggered. As can be seen from the sweep experiment, the stronger the response of the eigenmode, the more pronounced the modal nonlinearity exhibited. Therefore, it can be reasonably assumed that as long as the energy of the shock excitation is large enough to produce a stronger response for each eigenmode of the canvas, the modal nonlinearities would be similar to that in the sweep experiment, and hence would also be observed in the hammer experiment.

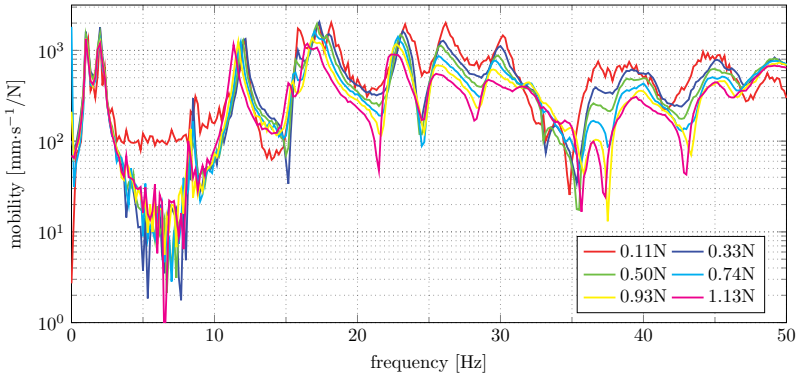


Figure 5.7: Mobility spectrum at the measurement point obtained by applying different intensities of hammering forces to the canvas of the seascape painting.

In order to verify this assumption, an exaggerated experiment was designed and then conducted. Different from the hammer experiment where the excitation was performed on the strainer, this experiment selected the excitation point directly on the canvas. In this way it avoided the consumption of shock energy on the strainer, so that the canvas can obtain excessive shock. The location of the excitation point on the canvas is shown as the yellow point labeled EP2 in Fig. 5.1 and is centrally symmetrical with the measurement point. The experimentally obtained mobilities at the measurement point under different hammering forces directly on the canvas of the seascape painting are shown in Fig. 5.7. Due to the soft material of the canvas, the contact force between the hammer and the canvas is much smaller than the contact force between the hammer and the strainer. Figure 5.7 shows that the resonance frequency of the seascape painting tends to decrease as the hammering force increases, and the amplitude of the resonance peak also decreases accordingly, which is fully consistent with the trend of modal nonlinearities under lower sweep intensities shown in the left of Fig. 5.6. This indicates that the excessive shock on

the canvas at this time made the response of each eigenmode reach the same level of that under the lower sweep intensities. The hammer experiments on the canvases of the still life painting and the dummy painting D also show similar dynamical behavior, but are again not presented here.

In conclusion, with the help of the hammer experiment on the canvas, it can be demonstrated that regardless of whether the painting is subjected to shock or vibration excitation during transport, as long as the excitation energy is high enough, the painting will exhibit modal nonlinearities. Although the hammer experiment on the canvas is not practically allowed for real paintings of artistic value, and has only been conducted under laboratory conditions for paintings of negligible artistic value, it has still served being valuable for comparison and evaluation.

5.2.4 Nonlinear Output Frequency Response Functions

The above experiments demonstrated through deterministic signals that paintings exhibit modal nonlinearities with increasing excitation intensity under mechanical load. However, paintings are always subjected to nondeterministic excitation during transport. In order to compensate for the influence of the differences in excitation characteristics on the conclusions, this section aims to further demonstrate the existence of nonlinearity in the transport-induced vibration of paintings by means of random excitation and nonlinear output frequency response functions.

5.2.4.1 Theoretical Background

In [LangBillings05, Billings13, BaymaZhuLang18], the definition of nonlinear output frequency response functions (NOFRFs) is given

$$G_n(j\omega) = \frac{\int_{-\infty}^{+\infty} \cdots \int_{-\infty}^{+\infty} H_n(j\omega_1, \dots, j\omega_n) \prod_{i=1}^n U(j\omega_i) d\omega_1 \cdots d\omega_n}{\int_{-\infty}^{+\infty} \cdots \int_{-\infty}^{+\infty} \prod_{i=1}^n U(j\omega_i) d\omega_1 \cdots d\omega_n}, \quad n = 1, \dots, N, \quad (5.2)$$

under the condition of $U(j\omega_i) \neq 0$, where $U(j\omega)$ is the Fourier transform of system input $u(t)$ and $H_n(j\omega_1, \dots, j\omega_n)$ is the n th order generalized frequency response function (GFRF), see [George59, LangBillings96]. Then, the output frequency response $Y(j\omega)$ of a nonlinear system can be expressed as

$$Y(j\omega) = \sum_{n=1}^N Y_n(j\omega) = \sum_{n=1}^N G_n(j\omega) U_n(j\omega). \quad (5.3)$$

In this formula, $U_n(j\omega)$ is n th order nonlinear input of the system or denotes the Fourier transform of $u^n(t)$, $Y_n(j\omega)$ is the n th order output frequency response of the system.

Equation (5.3) is expressed in a manner which is similar to the description for the output frequency response of linear systems. The above description can be represented as Fig. 5.8. A very important property of the NOFRFs $G_n(j\omega)$ is that it is insensitive to a change of the input spectrum by a constant gain, which allows the identification of the NOFRFs directly using the system input and output data.

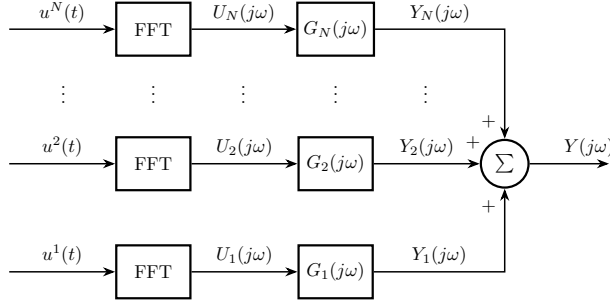


Figure 5.8: The output frequency response of a nonlinear system described by the NOFRFs.

From Equation (5.3), it is known that

$$\begin{aligned} Y(j\omega) &= \sum_{n=1}^N G_n(j\omega)U_n(j\omega) = \sum_{n=1}^N (G_n^R + jG_n^I)(U_n^R + jU_n^I) \\ &= \sum_{n=1}^N (G_n^R U_n^R - G_n^I U_n^I) + (G_n^R U_n^I + G_n^I U_n^R)j, \end{aligned} \quad (5.4)$$

where G_n^R and G_n^I are the real and imaginary parts of $G_n(j\omega)$, and U_n^R and U_n^I are the real and imaginary parts of $U_n(j\omega)$. Therefore

$$\begin{bmatrix} \operatorname{Re} Y(j\omega) \\ \operatorname{Im} Y(j\omega) \end{bmatrix} = \begin{bmatrix} U_1^R, \dots, U_N^R, -U_1^I, \dots, -U_N^I \\ U_1^I, \dots, U_N^I, U_1^R, \dots, U_N^R \end{bmatrix} \begin{bmatrix} G^R \\ G^I \end{bmatrix}, \quad (5.5)$$

where $G^R = [G_1^R, \dots, G_N^R]^T$ and $G^I = [G_1^I, \dots, G_N^I]^T$.

Consider the case $u(t) = \alpha u^*(t)$ where α is a constant and $u^*(t)$ is the input signal under which the NOFRFs of the system are to be evaluated, then,

$$U_n(j\omega) = \alpha^n U_n^*(j\omega), \quad (5.6)$$

where

$$U_n^*(j\omega) = \frac{1/\sqrt{n}}{(2\pi)^{n-1}} \int_{\omega_1 + \dots + \omega_n = \omega} \prod_{i=1}^n U^*(j\omega_i) d\sigma_{n\omega}, \quad (5.7)$$

and $U_n^*(j\omega)$ is the Fourier transform of $u^*(t)$. Excite the system \bar{N} times using the input signal $\alpha_i u^*(t)$ ($i = 1, \dots, \bar{N}$) where $\bar{N} > N$ and $\alpha_{\bar{N}}, \alpha_{\bar{N}-1}, \dots, \alpha_1$ are constants which satisfy the condition $\alpha_{\bar{N}} > \alpha_{\bar{N}-1} > \dots > \alpha_1 > 0$ to generate \bar{N} output frequency responses $Y_i(j\omega)$. From Equation (5.5), it is known that the output frequency responses can be related to the NOFRFs as

$$\begin{bmatrix} \operatorname{Re} Y_1(j\omega) \\ \operatorname{Im} Y_1(j\omega) \\ \vdots \\ \vdots \\ \operatorname{Re} Y_{\bar{N}}(j\omega) \\ \operatorname{Im} Y_{\bar{N}}(j\omega) \end{bmatrix} = \begin{bmatrix} \alpha_1 U_1^R, \dots, \alpha_1^N U_N^R, -\alpha_1 U_1^I, \dots, -\alpha_1^N U_N^I \\ \alpha_1 U_1^I, \dots, \alpha_1^N U_N^I, \alpha_1^N U_1^R, \dots, \alpha_1^N U_N^R \\ \vdots \\ \vdots \\ \alpha_{\bar{N}} U_1^R, \dots, \alpha_{\bar{N}}^N U_N^R, -\alpha_{\bar{N}} U_1^I, \dots, -\alpha_{\bar{N}}^N U_N^I \\ \alpha_{\bar{N}} U_1^I, \dots, \alpha_{\bar{N}}^N U_N^I, \alpha_{\bar{N}}^N U_1^R, \dots, \alpha_{\bar{N}}^N U_N^R \end{bmatrix} \begin{bmatrix} G_1^{*R}(j\omega) \\ G_1^{*I}(j\omega) \\ \vdots \\ \vdots \\ G_{\bar{N}}^{*R}(j\omega) \\ G_{\bar{N}}^{*I}(j\omega) \end{bmatrix}. \quad (5.8)$$

Consequently, the values of the NOFRFs $G_1^{*}(j\omega), \dots, G_{\bar{N}}^{*}(j\omega)$ can be determined using a least squares-based approach. This algorithm requires experiment or simulation results for the system under \bar{N} different input signal excitations $\alpha u^*(t)$. The approach can be applied when either a simulation model such as a mathematical, finite element model is available, or when practical experiments for multiple inputs can be performed on the system.

5.2.4.2 Nonlinearity Detection in Paintings

The NOFRFs provide a convenient approach in reflecting the strength of system nonlinearities and fault detection because these are functions of a single frequency variable [PengEtAl11, MaoEtAl18]. The NOFRFs $G_n(j\omega)$ represent a frequency domain description of the dynamical properties of the system, and any differences between the GFRFs of a normal and a nonlinear or damaged structure will be reflected by differences between the NOFRFs evaluated using the same system input. Consequently, the NOFRFs or an associated index can be used to describe the features of a structural system for nonlinearity or damage detection purposes. The NOFRF-based index can be defined as

$$Fe(n) = \frac{\int_{-\infty}^{+\infty} |G_n(j\omega)| d\omega}{\sum_{n=1}^N \int_{-\infty}^{+\infty} |G_i(j\omega)| d\omega}, \quad 1 \leq n \leq N. \quad (5.9)$$

The index $Fe(n)$ can be used to represent the features of a system, and because $\sum_{n=1}^N Fe(n) = 1$, this index reflects the strength of the different order of system nonlinearities. For example, $Fe(1) \approx 1$ implies that $G_1(j\omega)$ dominates the system behavior and the contribution of higher-order NOFRFs to the system frequency response can be neglected. In this case, the system can be considered linear and the system output frequency response can approximately be described by $Y(j\omega) = G_1(j\omega)U_1(j\omega)$. Alternatively, if $Fe(5) \approx 1$ this implies that the fifth-order system nonlinearity dominates the system behavior. Therefore, the N values of the index $Fe(n)$ describe the nonlinearity status of the system and can be used for structural nonlinearity and damage detection.

Based on the ideas introduced above, nonlinearity detection was conducted in the thesis for the three investigated paintings using the NOFRF-based analysis. The experimental setup is identical to the sweep experiment with excitation on the strainer. However, the excitation signal was replaced by a narrowband noise. It was generated in Matlab by normally distributed pseudo-random numbers with length 100000 (100s and $\Delta t = 1\text{ ms}$) and passed through a low-pass filter with a cutoff frequency of 50 Hz. The narrowband noise with an amplification factor of α_i was fed into the electrodynamic shaker to excite the three investigated paintings. A total of 20 steps of amplification factor ($\bar{N} = 20$) were selected and ensured that the largest root mean square values of the data collected by all accelerometers on the strainer exceed those during transport in [HeinemannEtAl19]. Record the excitation force and the velocity response on the canvas. The system NOFRFs $G_n(j\omega)$ can then be identified based on Equation (5.8). Here, the maximum order of the NOFRFs is limited to $N = 6$. Further, the values of a NOFRF-based index in Equation (5.9) were determined for three investigated paintings as shown in Table 5.2.

Table 5.2: Values of the NOFRF index for the three investigated paintings.

| painting | $Fe(1)$ | $Fe(2)$ | $Fe(3)$ | $Fe(4)$ | $Fe(5)$ | $Fe(6)$ |
|------------|---------|---------|---------|---------|---------|---------|
| seascape | 0.636 | 0.232 | 0.092 | 0.035 | 0.004 | 0.001 |
| still life | 0.601 | 0.223 | 0.106 | 0.056 | 0.010 | 0.004 |
| dummy | 0.552 | 0.257 | 0.122 | 0.056 | 0.011 | 0.002 |

The results in Table 5.2 show that the NOFRF index clearly reveals the presence of nonlinearities in paintings. The index $Fe(1)$ is a feature which represents the linear characteristic of paintings. All three paintings have the largest value in $Fe(1)$, but they do not dominate absolutely. This suggests that although linear characteristics are still predominant, nonlinear characteristics should not be ignored. The indices $Fe(2), \dots, Fe(6)$ are all features which represent nonlinear characteristics of paintings. They decay with increasing order. The first four orders of $Fe(n)$ already take up more than 98 % of the weight, therefore the higher orders of NOFRF are negligible.

All in all, this section employs narrowband noise to simulate the transport-induced vibration of paintings, which is more inclined to the actual situation. The existence of nonlinearities in paintings during transport is further argued by identifying NOFRFs. This reinforces the view that modal nonlinearities in paintings during transport cannot be ignored.

5.3 Modal Nonlinearities During Vibration

After the observation in the previous section that sufficiently large excitation energies can trigger nonlinear phenomena, the results obtained from sweep experiments are further

analyzed in this section for the three investigated paintings. Their general behavior of modal nonlinearities is discussed and some possible consequences of the modal nonlinearities on transport are deduced accordingly.

5.3.1 Analysis of Nonlinear Characteristics

As demonstrated by the experimental results in Section 5.2.2, only the sweep experiment can fully identify the modal nonlinearities of the three investigated paintings. Thus, the analysis of the modal nonlinearities presented in this section is only based on the sweep experiment results. Furthermore, it is already known that the modal nonlinearities of paintings are directly related to the vibration intensity. The peak value of the vibration displacement for each eigenmode can most intuitively reflect its vibration intensity. Even in the nonlinear case, the frequency corresponding to the peak vibration displacement of an eigenmode is sometimes referred to as resonance frequency, and the peak is referred to as resonance peak [NayfehMook08]. For the sake of brevity, this convention has been adopted as it represents the same concept. However, it should be noted that in the nonlinear case both terms have a different meaning than in the linear case.

This study establishes the relationship between the resonance frequency and the vibration displacement amplitude at resonance for each eigenmode under different vibration intensities. This analysis aids in examining the modal nonlinearities of the three investigated paintings. Figures 5.9, 5.10 and 5.11 show the relationship between the resonance frequency of the first two eigenmodes and their corresponding vibration displacement at the measurement point for the seascape painting, the still life painting, and the dummy painting D, respectively, during sweeping with increasing and decreasing frequency. In these figures, the peak to peak values of vibration displacements are plotted. It should be noted that the intention is to express the change in resonance frequency for the amplitude of the resonance peak under different vibration intensities, which are characterized by peak-to-peak vibration displacement.

First of all, the most obvious characteristic is the nonlinearity of the resonance frequency. With respect to the two real paintings, as the vibration displacement increases, their resonance frequency first drops slightly and then rises sharply. The only difference is that, probably due to the higher eigenfrequency, the resonance frequency of the still life painting changes less than that of the seascape painting. On the contrary, for the dummy painting D, its resonance frequency always increases with the increase of vibration displacement. Although fluctuations in the resonance frequency of the dummy painting D are observed at lower vibration displacements, more detailed investigation has shown that those fluctuations are caused by very small changes in climate. Even though a climate box was used, very small changes in climate are very difficult to avoid. Furthermore, it turned out that the freshly prepared dummy painting is more sensitive to climate changes

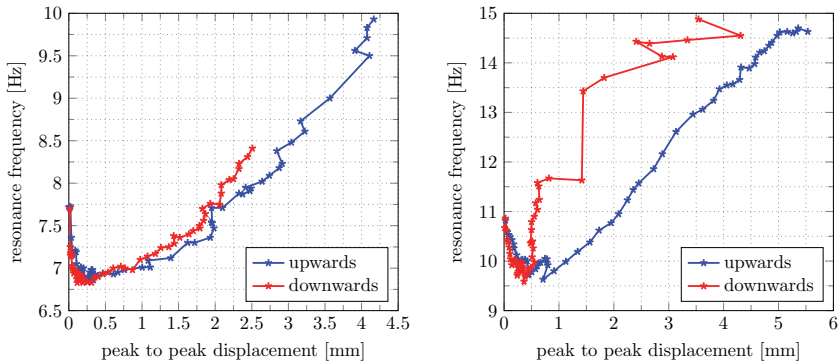


Figure 5.9: Relationship between the first two resonance frequencies of the seascape painting and their corresponding vibration displacements at the measurement point, left: the first eigenmode, right: the second eigenmode.

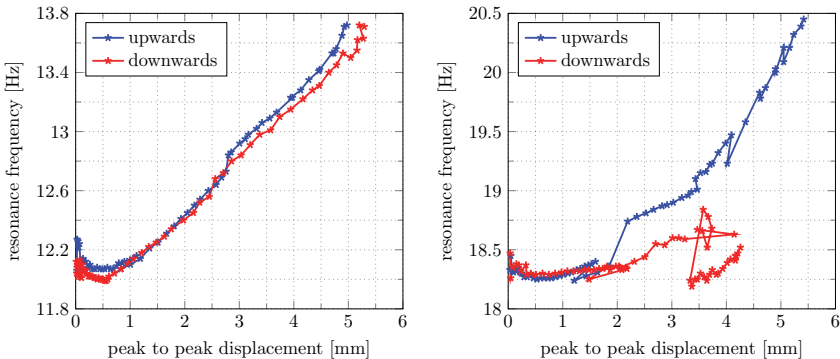


Figure 5.10: Relationship between the first two resonance frequencies of the still life painting and their corresponding vibration displacements at the measurement point, left: the first eigenmode, right: the second eigenmode.

than the real paintings after natural aging.

The next notable modal nonlinearity that can be observed is the difference in modal characteristics obtained by sweeping upwards and downwards. When the vibration displacement is lower, under the same vibration intensity, the resonance frequency obtained by sweeping upwards is basically the same as that obtained by sweeping downwards. However, as the vibration displacement increases, the difference between the modal characteristics obtained by up-sweep and down-sweep becomes larger and larger. Under

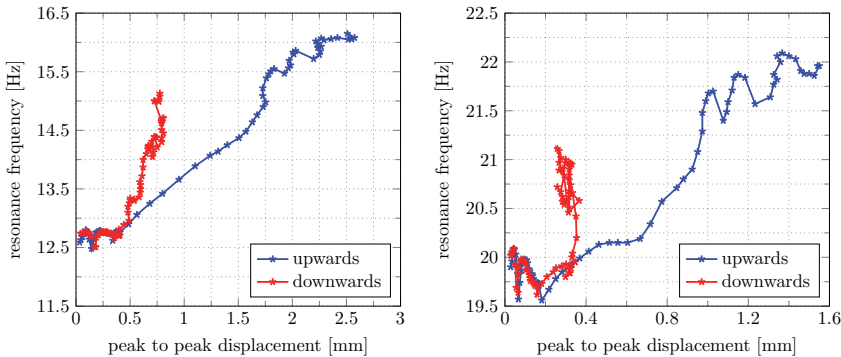


Figure 5.11: Relationship between the first two resonance frequencies of the dummy painting D and their corresponding vibration displacements at the measurement point, left: the first eigenmode, right: the second eigenmode.

the same vibration displacement, for the seascape painting and the dummy painting D, the resonance frequency obtained by up-sweep is higher than that obtained by down-sweep, while for the still life painting, the opposite is true. Moreover, during the sweep experiment, the input voltage ranges of the electrodynamic shaker were the same for both the up-sweep and down-sweep, but the maximum vibration displacement obtained for down-sweep is smaller than those for up-sweep. The only exception is that for the first eigenmode of the still life painting, its maximum vibration displacement obtained by down-sweep is slightly higher than that obtained by up-sweep.

The last modal nonlinearity relates to the decrease in the amplitude of the resonance peak in the mobility curve. Although the vibration displacement of the painting increased gradually with increasing input voltage of the shaker, the amplitude of each resonance peak in the mobility curve decreases with vibration intensity, as shown in Fig. 5.6. As for the reasons of this behavior, two assumptions can be given. Firstly, it may be that with increasing excitation intensity, hence increasing vibration amplitude, also damping due to moving air increases. Secondly, it may also be possible that as vibration intensity increases, the intensity of the harmonics gradually increase, thereby reducing the proportion of energy occupied by the primary resonance. In order to verify, or negate those assumptions, more detailed research is necessary.

5.3.2 Discussion on the Consequences for Transport

Since it has been demonstrated that modal nonlinearities inevitably occur during transport, and the characteristics of modal nonlinearities in paintings have also been summarized,

some possible consequences of modal nonlinearities for painting transport will be discussed in this subsection.

5.3.2.1 Resonance Frequency

The variation of resonance frequency with vibration intensity is the most typical characteristic of the modal nonlinearities for paintings. For a linear system, the resonance frequency would not depend on excitation amplitudes. If the painting is only subjected to shock excitation during transport, the painting can be directly treated as a linear system, simply because the energy delivered to the painting is too small to drive the response into a region of considerable nonlinearity. Once the painting is subjected to vibration excitation during transport, the change of resonance frequency caused by its modal nonlinearity will become a problem that cannot be ignored. Table 5.3 lists the variation in the first three resonance frequencies of the three investigated paintings and the peak to peak value of the corresponding maximum vibration displacement at resonance, which have been shown to possibly occur during transport in Section 5.2.2. Most of the resonance frequencies have a variation in more than 2 Hz when the amplitude of the vibration displacement is only 2 mm. Such a wide variation range will greatly increase the probability of the eigenmodes being excited during transport, which will make the painting more susceptible to damage. Besides, if the packaging system only takes vibration isolation measures against the eigenfrequency of the painting, then when the painting is subjected to stronger vibrations, these measures will not help due to the change of the resonance frequency. Therefore, in order to prevent the eigenmodes of the painting from being excited during transport, it is necessary to consider the variation range of the resonance frequency.

Table 5.3: The variation of the first three resonance frequencies for three investigated paintings and their maximum vibration peak to peak displacement at resonance for the up-sweep experiment.

| painting | Δf_1 [Hz] | Δd_1 [mm] | Δf_2 [Hz] | Δd_2 [mm] | Δf_3 [Hz] | Δd_3 [mm] |
|------------|-------------------|-------------------|-------------------|-------------------|-------------------|-------------------|
| seascape | 3.09 (42 %) | 4.16 | 4.07 (38 %) | 5.53 | 3.02 (22 %) | 4.28 |
| still life | 1.65 (14 %) | 4.98 | 2.20 (12 %) | 5.42 | 2.21 (10 %) | 5.39 |
| dummy | 3.67 (29 %) | 2.58 | 2.53 (8 %) | 1.55 | 2.00 (8 %) | 1.25 |

5.3.2.2 Amplitude of the Resonance Peak

As mentioned in Section 5.3.1, because of the modal nonlinearity, the change in the resonance frequency is always accompanied by the change in the amplitude of the resonance peak. Generally, in the frequency response function curve, the amplitude of the resonance

peak decreases with the increase in the vibration intensity. At a lower vibration intensity, the resonance peak is sharp and the amplification is higher, while at a higher vibration intensity, the resonance peak is broad or even flat, and the amplification is lower, as shown in Fig. 5.6. This does not mean that the actual vibration amplitude decreases with excitation intensity, but rather that a certain excitation is amplified to a lower extent. In fact, as the vibration intensity increases, the response on the canvas continues to increase, but to a smaller proportion than the increase in excitation intensity. The frequency range of a sharper resonance peak that can cause a strong vibration is smaller than that of a broader resonance peak. In summary, for higher excitation intensities large canvas displacements will likely be excited over a broad frequency bandwidth (broad and flat peak). For smaller excitation intensities strong canvas displacements will only occur if a resonance frequency is almost exactly hit, but if that happens, even smaller excitation intensities lead to large displacements (sharp and high peak).

5.3.2.3 Harmonics

It is a general property of nonlinearity that harmonics can be observed in sinusoidal sweep experiments and it is inevitable to observe them to some extent in modal testing. However, the excessively strong harmonics observed in the three investigated paintings make the harmonic phenomenon a problem that cannot be ignored during transport. The right of Fig. 5.12 shows the response of the seascape painting to a simple harmonic excitation at 21.8 Hz with an intensity of magnitude L_7 . The intensity of the subharmonic at approximate 11 Hz observed in the seascape painting is of the same order of magnitude as the fundamental vibration. Besides, it has also been observed in the seascape painting that the intensity of the superharmonics for a fundamental frequency of 7.95 Hz is even higher than that of the fundamental vibration, as shown in the left of Fig. 5.12. Excessive harmonics will also damage paintings and accelerate their aging. Therefore, it is necessary not only to prevent the eigenmodes from being excited during the transport of paintings, but also avoiding the excitation of harmonic vibrations as much as possible. This makes the dynamic design of isolation devices for transport crates much more difficult because not only the regions of fundamental resonance frequencies (referred to as eigenfrequencies from a linear perspective) must be avoided, but also their sub- and superharmonics. This leaves very little room for harmless frequency ranges to which dynamic isolation devices for a safer transport can be tuned.

The excessive appearance of harmonics also makes the identification of the fundamental resonance frequencies more difficult. When calculating the mobility according to Equation (5.1), the harmonics can lead to a very noisy mobility. The reason for this is that for a sinusoidal sweep experiment the system responds with a considerable magnitude with a different spectral content (harmonics) than the excitation (fundamental). Hence, in Equation (5.1) a response of considerable magnitude (harmonics) is divided by a very

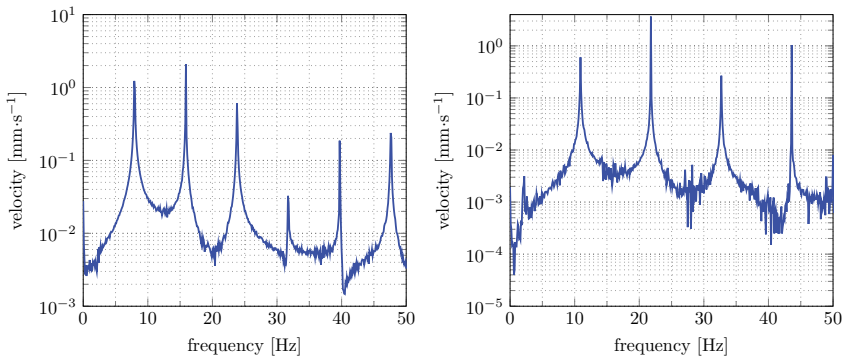


Figure 5.12: Superharmonics with a fundamental frequency of 7.95 Hz (left) and the subharmonic with a fundamental frequency of 21.8 Hz (right) for the seascape painting.

small excitation signal because the excitation frequency is the fundamental. For a real measurement, the response (harmonics) is essentially divided by noise and, therefore, the harmonic peak appears as an extremely noisy peak. This is the reason for the necessary filtering in Section 5.2.2.

5.3.2.4 Up and Down Sweep

It is an observation that the same excitation intensity leads to different resonance amplitudes depending on whether the sweep was performed upwards or downwards. Thereby, another consequence for transport arises which is more readily to be understood when presented as in Fig. 5.13 which shows the mobility for an up and down sweep.

Obviously for a frequency range between 17 Hz and 35 Hz, the response is different whether the excitation frequency approaches a resonance frequency from above or from below. Not only does the resonance frequency change, but also the sharpness and width of the resonance peak are affected. This implies that besides the excitation intensity, the history of the excitation, too, has an influence on the vibration response which may lead to a wider band of undesired excitation frequencies. Therefore, it is not enough to only analyze the content of the excitation spectrum of the painting during transport and propose vibration isolation measures accordingly. It is also necessary to analyze different excitation schemes, taking into account the situation that the excitation approaches the vibration mode from the forward and reverse direction.

In [Kracht11], the Duffing oscillator has been used as an analogy to account for nonlinear phenomena in paintings, such as the variation of resonance frequency with excitation intensity and the difference between the up sweep and down sweep, among others. This

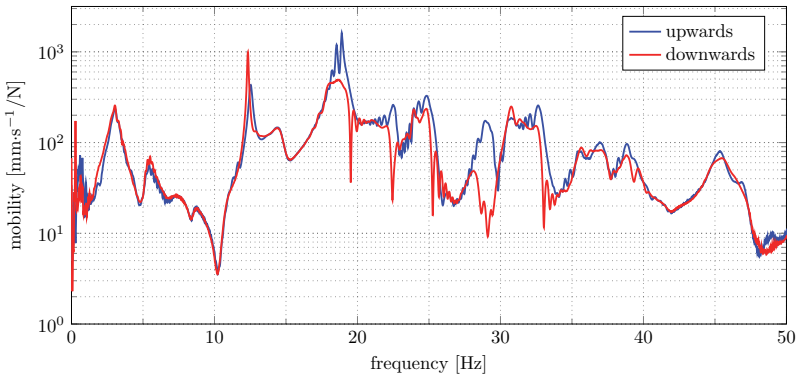


Figure 5.13: Mobility difference between up and down sweep for the still life painting at an excitation intensity L_8 .

theory can be further extended by combining the results in this thesis and the properties of square and cubic stiffness nonlinearities described in [NayfehMook08]. That is, in addition to the linear stiffness, the bending stiffness of the canvas itself suffers from a squared stiffness term plus a cubic stiffness term, and consequently a geometric nonlinearity under high excitation intensity.

The system with positive quadratic nonlinearity exhibits a softening effect, causing the frequency response curves to shift toward lower frequencies. Conversely, a system with positive cubic nonlinearity exhibits a hardening effect, bending the frequency response curves toward higher frequencies and is accompanied by jump phenomena. These behaviors were consistently observed during the experiments. It is reasonable to speculate that when the excitation intensity is weak, the linear stiffness dominates. The vibration of the painting remains within the linear range and does not exhibit any nonlinearities, as demonstrated by the hammer experiment on the strainer. However, as the excitation increases, the quadratic stiffness gradually comes into play. Increased excitation leads to a decrease in resonance frequency, as shown by the hammer experiment on the canvas, without significant differences between upward and downward sweeps. At sufficiently high excitation levels, the cubic stiffness term becomes more influential than the quadratic stiffness term and dominates the response. Consequently, the resonance frequency increases with higher excitation intensity, as demonstrated by the sweep experiment on the strainer. Additionally, the jump phenomenon characteristic of the Duffing oscillator, associated with cubic stiffness, manifests as a difference between upward and downward sweeps in paintings. Moreover, the canvas material of the painting may also exhibit nonlinear damping, inferred from the observation that the resonance peak flattens as excitation intensity increases. However, all these theories require validation through further practical experiment.

5.4 Nonlinear Behavior Identification Methods

In this thesis several devices as well as different methods have been used to identify the nonlinear dynamic behaviors of paintings. As a mechanism omitted in the preceding sections, the method of using a loudspeaker to test the modal nonlinearities of paintings will be added in this section. Then, the advantages and disadvantages of all the methods are analyzed and their applicability occasions are discussed.

5.4.1 Sweep Experiment with Loudspeaker

Although the sweep experiment with the electrodynamic shaker can adequately capture the modal nonlinearities of paintings, there exist some deviations between the observed modal characteristics and its true modal characteristics. This is due to the fact that the stinger of the shaker was firmly connected with the painting strainer, which has changed the boundary conditions of the painting and consequently its dynamics, too. For example, the results of the hammer experiment on the strainer in Fig. 5.4 and the sweep experiment with electrodynamic shaker in Fig. 5.5 determined the first resonance frequencies of the seascape painting to be 7.83 Hz and 7 Hz, respectively, which was precisely caused by the difference in boundary conditions. For this reason, loudspeakers were used as excitation sources to measure the modal characteristics of the painting in some researches [WeiKragtVisser05, ChiribogaArroyo13]. As a contactless excitation method, it is simpler to measure the modal characteristics of the painting by using loudspeakers. As shown in the right of Fig. 5.2, it is only necessary to face the loudspeaker to the painting and provide an excitation signal to the loudspeaker through the signal generator, then the vibration of the canvas can be excited. This method is especially suitable for studying the modal characteristics of real precious paintings. However, because it is difficult to obtain any knowledge about the energy distribution of the loudspeaker input to the canvas, all analysis about the modal characteristics of the painting can only be based on the response of the canvas. It is the purpose of this section to verify the feasibility of using loudspeakers to measure the modal nonlinearities of paintings.

The parameters of the sweep excitation with loudspeaker are the same as the parameters of the sweep excitation with shaker. Figure 5.14 shows the velocity response spectrum for the canvas of the seascape painting under different acoustic excitation intensities when sweeping upwards. In order to highlight that those intensities do not correspond to those of the shaker experiment, they are denoted by $\tilde{L}_1, \tilde{L}_2, \dots, \tilde{L}_6$. The loudspeaker used in this thesis is a woofer with an advertised frequency characteristic of less than 30 dB loss between 20 Hz and 3000 Hz. But it can be seen from the velocity response spectrum, that the eigenmodes below 20 Hz are also well excited, which proves a good applicability of this measurement method.

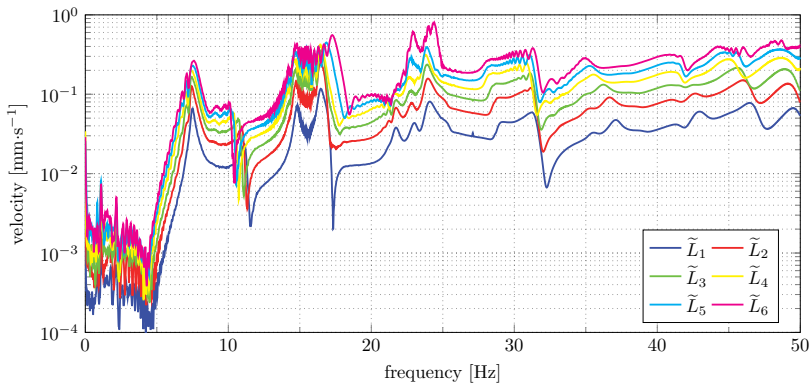


Figure 5.14: Velocity response spectrum for the canvas of the seascape painting under different intensities of acoustic excitation when sweeping upwards.

It is observed from Fig. 5.14 that most of the resonance frequencies first decrease and then increase with the increase in the acoustic excitation intensity, which is consistent with the trend observed from the sweep experiment with the shaker. Different resonance frequencies are also observed between the up-sweep and down-sweep. This proves the feasibility of using loudspeakers to measure the modal nonlinearities of paintings. However, unlike the electrodynamic shaker, due to the gap between the painting and the loudspeaker, the output energy of the loudspeaker does not fully engage with the painting. Consequently, the loudspeaker fails to excite the painting to achieve the same high vibration intensities as observed in the sweep experiment with the shaker. Therefore, it proves challenging for loudspeaker experiments to measure the modal nonlinearities of paintings to the same extent as observed during transport. Moreover, because the acoustic excitation is of different nature and directly excites only the canvas and is generally of smaller intensity, it is impossible to compare the state of the painting under the excitation of the loudspeaker with the state of the painting during transport. Thus, it is difficult to evaluate the modal nonlinearities obtained by sweep experiment with loudspeaker.

5.4.2 Evaluation of Different Identification Methods

The above performed analysis demonstrates that the identification about the modal nonlinearities of paintings is absolutely necessary for improving transport and the design of the packaging system. In this chapter, four experimental methods have been adopted to identify the nonlinear dynamic behavior of paintings, namely the hammer experiment on the strainer, the hammer experiment on the canvas, the sweep experiment with shaker

and the sweep experiment with loudspeaker. Different experimental methods can excite different vibration intensities, resulting in different ranges of modal nonlinearities that can be observed. Taking the first resonance frequency of the seascape painting as an example, the results obtained by four different experimental methods are shown in Fig. 5.15.

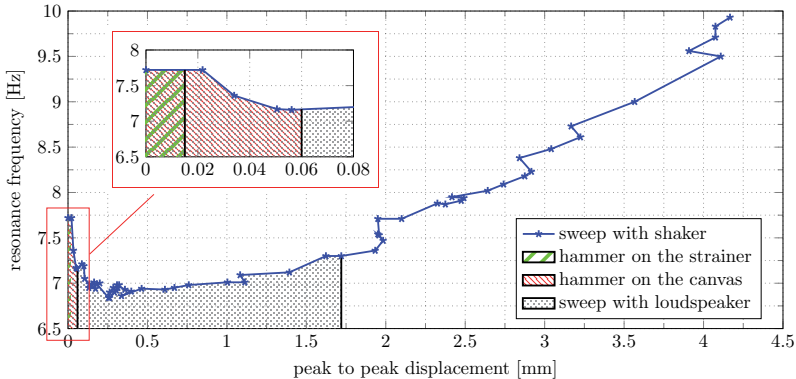


Figure 5.15: Different experimental methods lead to different vibration intensities and different observation ranges of modal nonlinearities.

The hammer experiment on the strainer cannot excite a strong response of the eigenmode, which results in the modal characteristics obtained under different shock intensities always being the same. Hence, it is difficult to observe the modal nonlinearities of the painting by conducting this method. But it is the best method to quickly measure the eigenfrequencies and the eigenmodes of the painting in a linear range. Because of excessive shock, the hammer experiment on the canvas can observe some slight modal nonlinearities of the painting, but this method is only suitable for lab conditions and for paintings of negligible artistic value or dummies. The sweep experiment is the best method to identify the modal nonlinearities of the painting. The modal nonlinearities observed in the sweep experiment with shaker are the most comprehensive, while the contactless sweep experiment with loudspeaker has a smaller range of observed modal nonlinearities. The use of narrowband noise supplemented by nonlinear output frequency response functions can detect the presence of nonlinearities, but it is difficult to identify the specific nonlinear dynamic behavior of paintings.

Chapter 6

Conclusion and Outlook

The interlibrary transport of paintings requires appropriate procedures in order to minimize associated risks and hazards involved in the transport process. One significant concern is vibration exposure during transport, which can lead to cracking on paint layers and even loss of paint from canvas. Consequently, art conservators must properly pack and handle paintings in order to protect them. However, a large number of decisions and precautions currently taken to mitigate the effects of vibration or to define tolerable levels of vibration are based on a limited understanding of the dynamic characteristics of the painting itself. Furthermore, most previous studies have measured everything except the painting itself, with vibration data from the strainer or packing case providing little insight into the actual behavior of the canvas. There is thus a lack of understanding of the actual vibration behavior of the canvas and its relationship to the damage produced in paintings during transport. Systematic research in this area is needed to provide guidelines to help art conservators in the care of their collections. This is where this thesis comes in and makes its contribution. With the modal characteristics summarized throughout this thesis from multiple paintings, art conservators can target improvements to the transport environment. As well, by applying the transport-induced vibration simulation methods developed in this thesis, many advanced investigations which cannot be done during a real transport can be easily performed in a controlled environment. In contrast to many other studies, all results in this thesis are realized by combining experimental, simulation and numerical approaches to confirm the practical applicability of the introduced models and methods.

First of all, using experimental modal analysis, the modal characteristics of paintings were examined progressively from simple to complex structures. Three different dummy paintings before and after the application of primer as well as two real paintings were investigated and their modal parameters were extracted. It was found that the canvas of the newly made painting is too soft and highly damped before the primer is applied, resulting in a weak response to the excitation, and hence, the identification of the exact modal parameters are difficult. After the application of primer, the canvas becomes stiffer

and less damped, significantly enhancing the identification quality of modal parameters. Many eigenmodes for the dummy painting with primer are concentrated in the frequency range below 100 Hz. As a simplified mechanical model, the rectangular vibrating membrane effectively predicted eigenfrequencies and mode shapes with a small error. However, various inhomogeneities in density, tension, and thickness, among others, caused variations in mode orders and distortions in the mode shapes, as evidenced by finite element (FE) models. Besides, the tilted canvas further exacerbated the distortion of mode shapes, but different securing methods of the canvas on the strainer were not observed to have a significant influence on the eigenmodes. After long-term aging, the painting material becomes softer and more damped, but the lower eigenmodes remain clearly recognizable. Compared to the new dummy painting, real paintings show significantly lower eigenfrequencies and many eigenmodes are concentrated within 50 Hz. Due to the excessive damage making the inhomogeneities of real paintings more severe, their mode shapes are more distorted, which makes it difficult to find a reference from the simplified mechanical model or FE model. These investigations show the general dynamic behavior of paintings, which, despite possible variations in transport, remains the fundamental basis for art conservators to improve transport conditions and predict potential damage.

The experimental research also revealed that climate is an important factor influencing the modal characteristics of paintings. The modal characteristics of paintings before applying primer are insensitive to changes in climate. However, after applying primer, a negative correlation between eigenfrequency of paintings and both temperature and humidity has been observed, as is the case with real paintings. The relationship between them can be linearized, i.e., a definite temperature and humidity gives a uniquely determined eigenfrequency. This allows for the possibility of compensating the changing modal characteristics based on a reference climate.

The bigger part of the thesis was concerned with the simulation of transport-induced vibration. Two approaches were proposed to address this issue, with reference data extracted from a real transport experiment. Both approaches are limited to simulating the transport-induced vibration perpendicular to the painting plane, which is most directly relevant to painting damage. The first method aims at replaying the vibration on the strainer, thereby reproducing the transport-induced vibration on the canvas. A simulation platform implementing a multi-channel FxLMS algorithm was developed for this purpose. The control algorithm simultaneously drove four electrodynamic shakers connected to the strainer and excited the strainer to move in a manner identical to the movement measured during transport. Consequently, the vibration at arbitrary points on the canvas can be measured by LDVs without contact and with respect to an inertial reference. The experimental results indicate that this simulation platform has a high accuracy in reproducing the vibration response on the strainer, even for small vibration around only 0.01 g. Some overshoot in the reproduction of shock response is observed in some cases, but the overall reproduction is still good. Furthermore, the vibration observed on the

canvas has a stable reproducibility. However, they deviate from the measurements during transport due to differences in the boundary conditions of paintings. For this reason, an improvement was conducted on the simulation platform. The investigated painting was fixed on a wooden plate, so as to simulate the state during transport as much as possible. The actuators drove the whole system consisting of the painting and the wooden plate thus replaying the vibration on the strainer. As a result of experiments, the overall behavior of the vibration on both the strainer and the canvas is well represented by this method. In order to further process the reproduction results on the canvas, the rainflow counting algorithm was used in this thesis to count and analyze the vibration data, which provides a better indicator for comparing the performance of different transport crates and assessing the painting damage. This reproduction approach to simulating the transport-induced vibration provides a reference for the unknown canvas vibration response during transport and allows art conservators to conduct relevant advanced investigation in the laboratory.

As a more accessible alternative, the second approach to simulating the transport-induced vibration is intended to reconstruct the vibration on the canvas. A numerical model describing the relationship between the vibration of all accelerometers on the strainer and the vibration at an arbitrary point on the canvas has been derived. Accordingly, a methodology for finding the optimal numerical model has been established. This methodology is based on hammer experiments to select the minimum number of excitation points and the optimal excitation locations from an excitation lattice. The numerical model developed for this excitation pattern is considered as being optimal. Furthermore, the analysis shows that the optimal excitation pattern generally applies to every point on the canvas. Feeding the vibration data from all accelerometers on the strainer into this numerical model, yields the vibration reconstruction at the corresponding point on the canvas. The experimental results show that the vibration reconstruction on the canvas agrees well with the vibration reproduction results. Therefore, the vibration reconstruction method offers a more accessible and practical alternative to vibration reproduction method, also providing valuable insights into the unknown vibration experienced by canvas during transport.

From the above study it was found that the modal characteristics of paintings vary with the vibration intensity. Whether this nonlinearity manifests itself during transport has been explored in the last part of this thesis. Three different mechanical loads including shock excitation, sweep excitation and narrowband noise were used to simulate the excitation to which the painting was subjected during transport. Referring to a real transport, experimental results show that it is difficult for shock excitation to excite the nonlinearities of paintings during transport. In contrast, paintings subjected to vibration excitation during transport are likely to exhibit modal nonlinearities. The narrowband noise experiments further demonstrate this conclusion through nonlinear frequency response functions. Modal nonlinearities in paintings include changes in resonance frequency, changes in resonance peak, harmonics, and differences in forward and reverse sweeps, all

of which can further exacerbate the deterioration of paintings during transport. Therefore, modal nonlinearities are a factor that should not be ignored in both the design of packing cases and the handling and packing of paintings. It is equally important to test the modal nonlinearities of paintings in advance using appropriate methods.

The advancements made in this thesis concerning the modal characteristics of paintings and the simulation of transport-induced vibration pave the way for further research. Referring to the summarized modal characteristics can guide the optimal design of transport crates, as well as the handling and packing of paintings. Since a larger number of eigenmodes for real paintings are concentrated in the lower frequency range, and their resonance displacements are usually significant, it is necessary to prevent these lower eigenmodes of paintings from being excited during transport. Given the existence of modal nonlinearities, vibration isolation measures should also take into account nonlinear factors such as resonant frequency variations, harmonics, and excitation history. Therefore, future research could focus on designing rational vibration isolation measures. Additionally, applying the two developed methods of simulating the transport-induced vibration could provide a reliable reference for the unknown vibration on the canvas during transport. This could offer new indicators for evaluating the transport quality. The performance of different transport crates can thus be compared more directly. The prolonged transport-induced vibration simulation could help observe the painting damage and further investigate the damage mechanism, so as to develop a tolerable vibration level. All of them are areas of great practical value for future research. Another research avenue might tackle the challenge of developing a nonlinear model for paintings. Although the nonlinear dynamic behavior of paintings has been identified in this thesis, there is still a lack of a proper model to explain the causes of these nonlinear phenomena. In addition, the accuracy of vibration reconstruction on the canvas by means of numerical model is not high enough because it is a linear model by its formulation. Introducing the nonlinear elements into the numerical model will be beneficial to improve the quality of the reconstruction results.

Appendix

A.1 Experimental Modal Analysis on Unprimed Dummy Painting B

Figure A.1 displays the CMIF of unprimed dummy painting B calculated from the mobility matrix in the frequency range up to 120 Hz and highlight the identified eigenfrequencies. In the evaluated frequency range, about 25 eigenfrequencies are identified, most of which are found in the first CMIF. In the low frequency range up to 11 Hz, due to the soft suspension of the dummy painting, nine eigenfrequencies related to rigid body modes are identified.

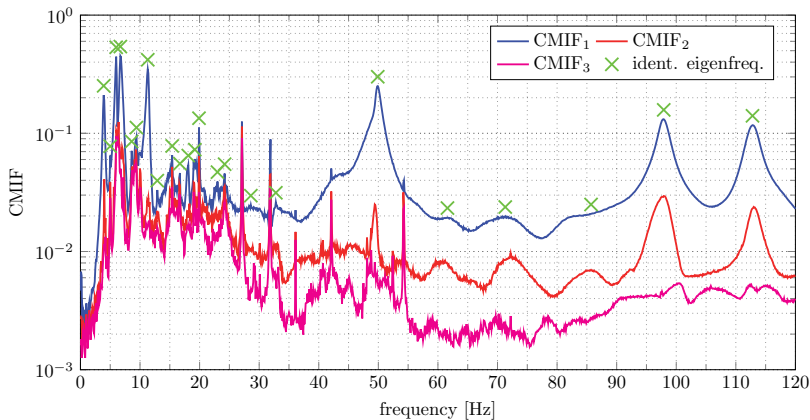


Figure A.1: CMIF of unprimed dummy painting B with identified eigenfrequency locations.

Figure A.2 shows the measured and reconstructed mobilities of unprimed dummy painting B in amplitude and phase for one input-output combination. This comparison allows assessing the quality of modal parameter identification of dummy painting B and also serves as a modal model. Following this, the viscous damping identified for each eigenmode and their average values are illustrated in Fig. A.11.

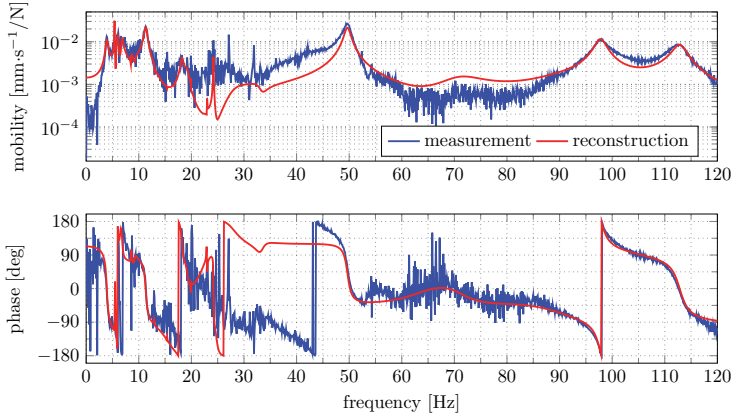


Figure A.2: Amplitude (top) and phase (bottom) of a mobility excited in the bottom center and measured in the upper right for unprimed dummy painting B.

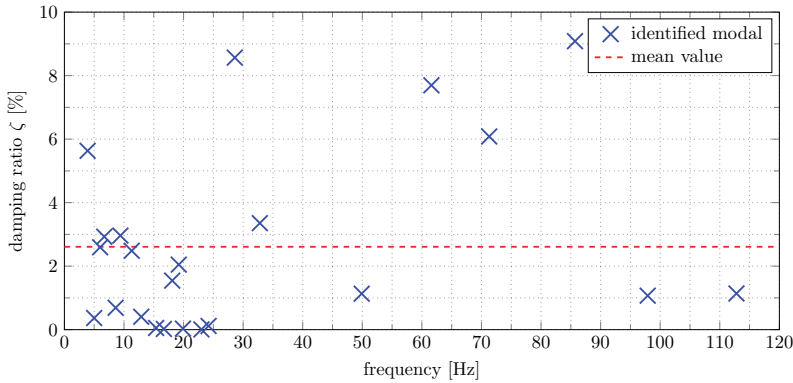


Figure A.3: Identified modal damping ratios for unprimed dummy painting B and their mean value.

Moreover, the eight identified mode shapes of unprimed dummy painting B with their corresponding eigenfrequencies are presented in Fig. A.4. The ordering in Fig. A.4 does not represent the modal order because of the low signal-to-noise ratio in the lower frequency range (below 50 Hz) and the serious noise interference, which make it difficult to recognize some of the eigenmodes. They are only selected eigenmodes with distinctive features. The eigenmode at 48.8 Hz is similar to the fourth eigenmode of the simplified mechanical model or the FE model.

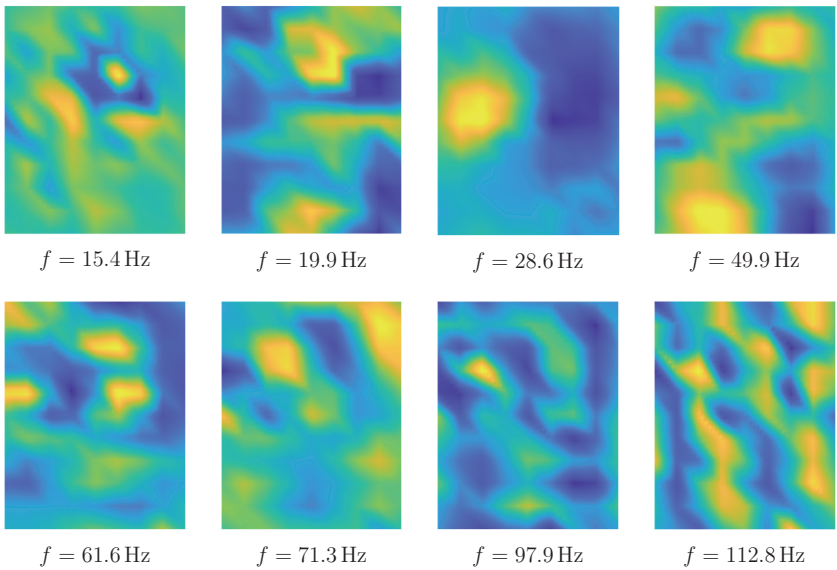


Figure A.4: The eight identified eigenmodes obtained from the experimental modal analysis for unprimed dummy painting B.

A.2 Experimental Modal Analysis on Unprimed Dummy Painting C

Figure A.5 illustrates the CMIF for unprimed dummy painting C, calculated using the mobility matrix within the frequency range up to 120 Hz. It emphasizes the eigenfrequencies that have been identified. Within this frequency range, approximately 23 eigenfrequencies have been pinpointed, predominantly situated in the first CMIF. Specifically, within the lower frequency range, up to 12 Hz, seven eigenfrequencies linked to rigid body modes are detected, owing to the soft suspension characteristics of the dummy painting.

Figure A.6 depicts the amplitudes and phases of the measured and reconstructed mobilities of unprimed dummy painting C for a single input-output pairing. This side-by-side comparison enables the evaluation of the modal parameter identification quality for dummy painting C, essentially functioning as a modal model. Subsequently, Fig. A.7 showcases the identified viscous damping values for each eigenmode as well as their average values.

In addition, Figure A.8 displays the eight identified mode shapes of unprimed dummy

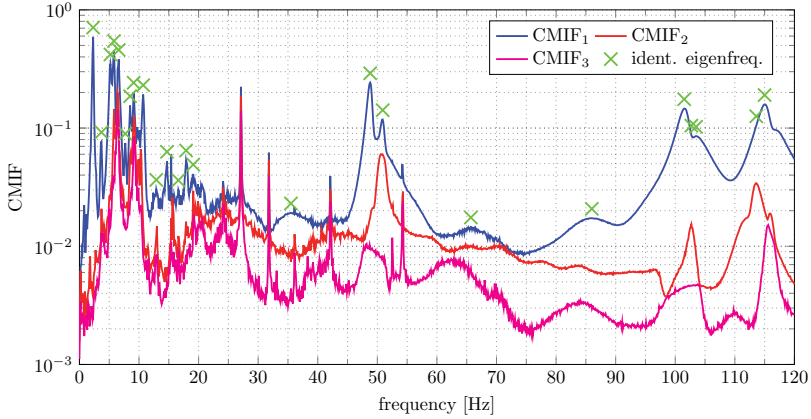


Figure A.5: CMIF of unprimed dummy painting C with identified eigenfrequency locations.

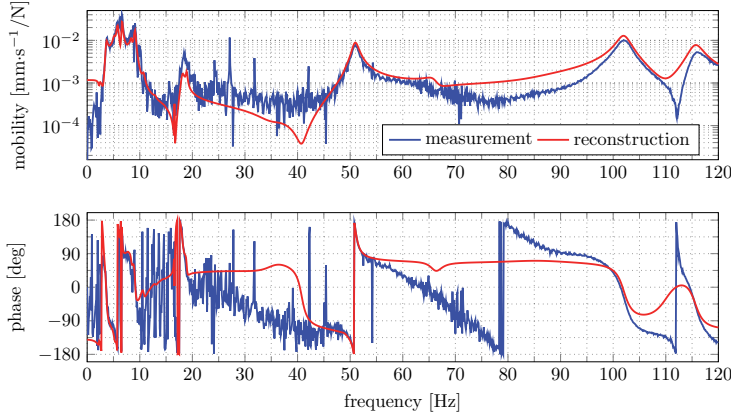


Figure A.6: Amplitude (top) and phase (bottom) of a mobility excited in the bottom center and measured in the upper right for unprimed dummy painting C.

painting C alongside their corresponding eigenfrequencies. However, it's important to note again that the order depicted in Fig. A.8 does not accurately represent the modal order due to challenges posed by a low signal-to-noise ratio below 50 Hz, coupled with significant noise interference. Consequently, some of the eigenmodes become difficult to identify. Notably, the displayed eigenmodes are selectively chosen based on their unique characteristics. Specifically, the eigenmode at 50.9 Hz bears resemblance to the third

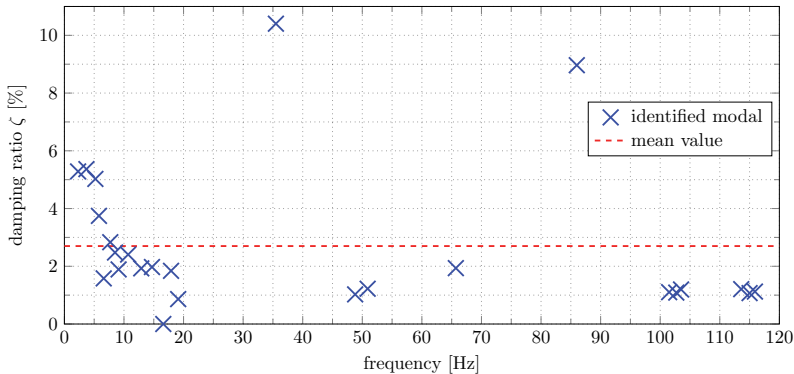


Figure A.7: Identified modal damping ratios for unprimed dummy painting C and their mean value.

eigenmode found either in the simplified mechanical model or in the FE model.

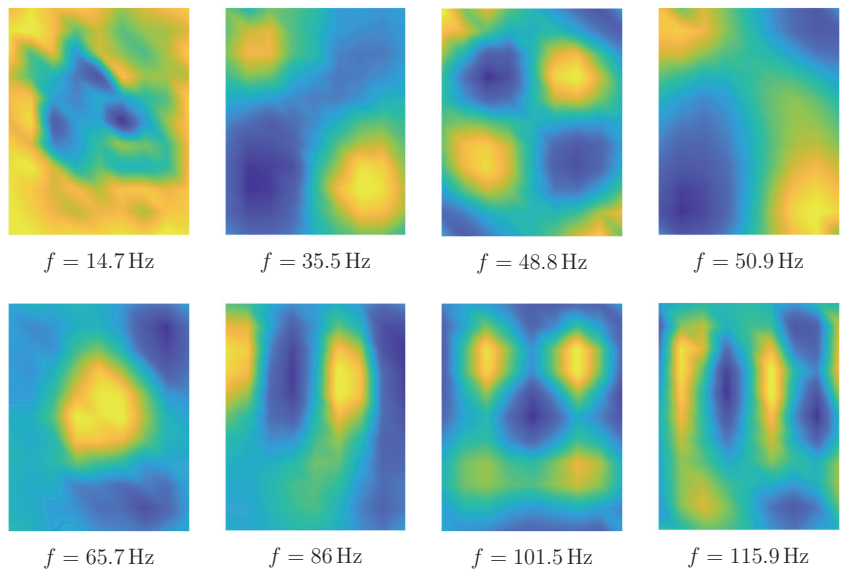


Figure A.8: The eight identified eigenmodes obtained from the experimental modal analysis for unprimed dummy painting C.

A.3 Experimental Modal Analysis on Primed Dummy Painting B

Figure A.9 shows the CMIF of primed dummy painting B derived from experimental modal analysis and highlights the identified eigenfrequencies. All peaks are clear and easily recognizable as the dummy painting becomes stiffer and less affected by noise after the primer is applied. A total of about 20 eigenfrequencies, 16 of which correspond to structural modes, are identified in the frequency range shown. Since the fluctuations in temperature and humidity are smaller, there are less secondary peaks. Below 25 Hz, the eigenfrequencies identified are related to the rigid body modes due to the soft suspension of the dummy painting. The first eigenfrequency is identified at 22.3 Hz. The small peak at 34.3 Hz is considered to be a small residue of the rubber band suspension.

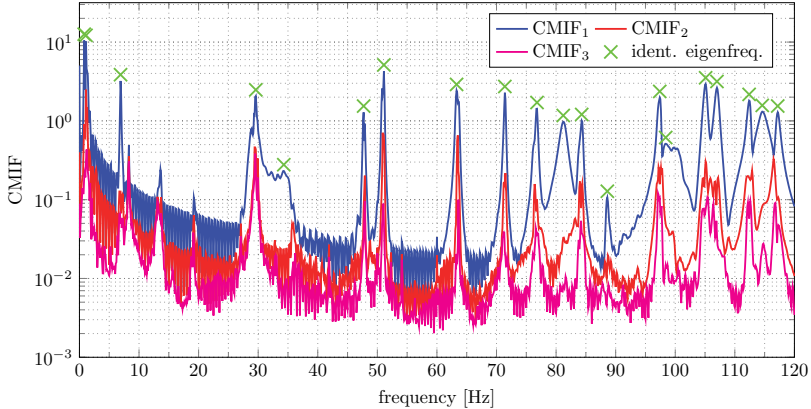


Figure A.9: CMIF of primed dummy painting B with identified eigenfrequency locations.

Figure A.10 compares the amplitudes and phases of the measured and reconstructed mobilities of primed dummy painting B under an input-output combination. The reconstructed mobilities fit the measured mobilities well over the evaluated frequency range. The quite good agreement between the measurements and the reconstructions indicates a successful parameter identification. Following this, Fig. A.11 illustrates the identified viscous damping ratios ζ_r for each eigenmode and their average values. Besides the rigid body modes, the viscous damping ratios of all structural modes are less than 1 %, with an average damping ratio of about 0.52 %, which is much smaller than the viscous damping ratios of the unprimed paintings.

Lastly, the first eight identified mode shapes of primed dummy painting B are presented in Fig. A.12. Owing to the better quality of parameter identification, the labelled numbers are

the order of each eigenmode. Most of the eigenmodes are distorted, but their corresponding standard mode shapes can be found in the simplified mechanical model. The FE model can demonstrate that these distortions may be caused by inhomogeneous tension or density. In addition, starting from the seventh eigenmode, the eigenmodes become severely distorted, which may have an additional influence caused by tilted canvas.

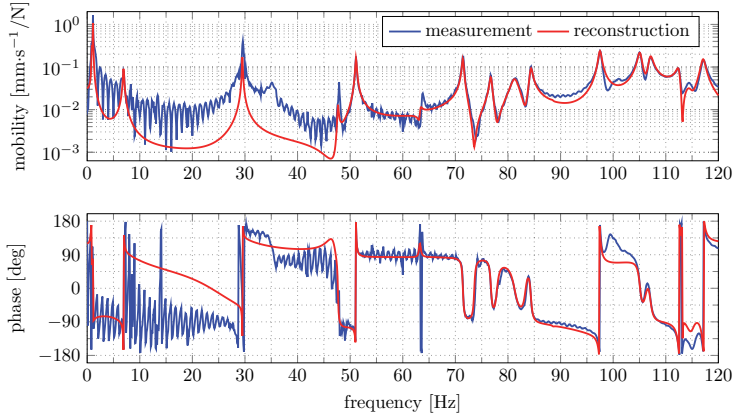


Figure A.10: Amplitude (top) and phase (bottom) of a mobility excited in the bottom center and measured in the middle for primed dummy painting B.

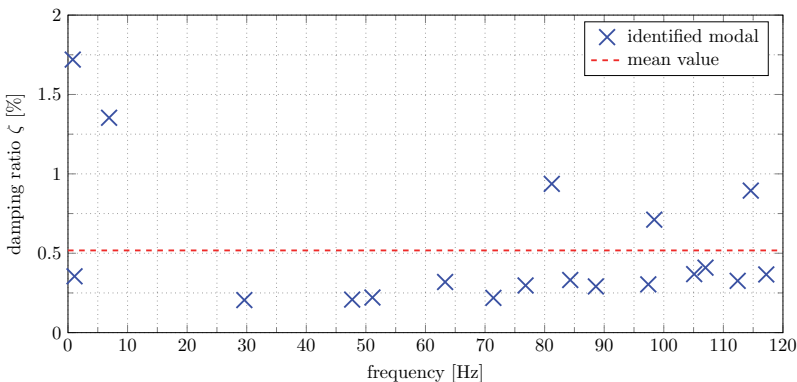


Figure A.11: Identified modal damping ratios for primed dummy painting B and their mean value.

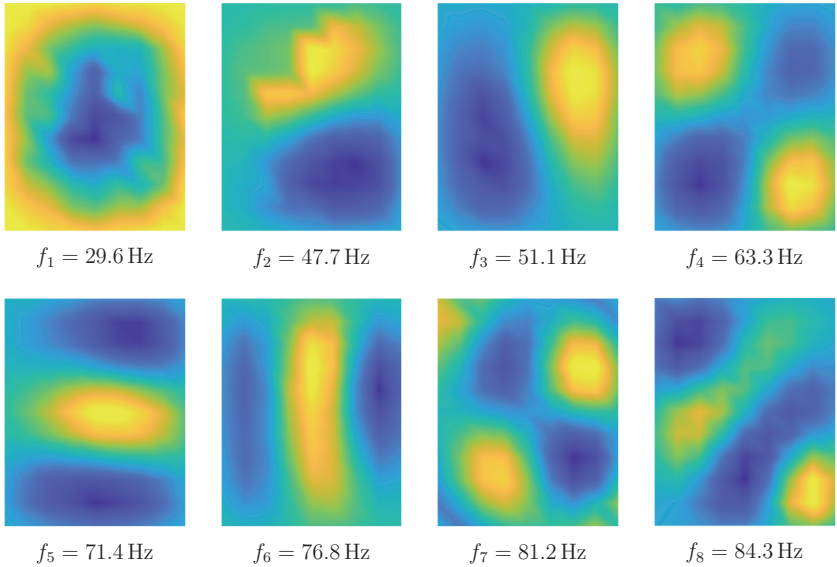


Figure A.12: The first eight identified eigenmodes obtained from the experimental modal analysis for primed dummy painting B.

A.4 Experimental Modal Analysis on Primed Dummy Painting C

As for the primed dummy painting C, the CMIF curves obtained from its experimental modal analysis are displayed in Fig. A.13, together with the identified eigenfrequencies. Again, all the peaks became pronounced after the application of primer. Moreover, the fluctuation in climate during the experiment is small, and almost no secondary peaks are found in the CMIF curves. Over the frequency range shown, a total of about 24 eigenfrequencies are identified, 20 of which correspond to structural modes. The first eigenfrequency is identified at 25.5 Hz, and peaks below this frequency are identified as corresponding to rigid body modes. The small peak at 27.5 Hz is considered to be a small residue of the rubber band suspension.

The measured and reconstructed mobilities for one input-output combination are used as an example in Fig. A.14 to illustrate the high quality of the modal parameter identification. Subsequently, the viscous damping ratios identified for each eigenmode are shown in Fig. A.15. Most of the structural modes have damping ratios less than 0.5 %. The eigenmode at 106.6 Hz has a high damping ratio that pulls up the mean value. Finally,

the first eight identified mode shapes of primed dummy painting C are listed in Fig. A.16 with their corresponding modal orders. It is surprising to find that the listed modal shapes are very regular with low distortions. All these modal shapes can find their counterparts in the simplified mechanical model. However, probably due to inhomogeneity or bending stiffness, some of the modal orders with close eigenfrequencies are reversed, such as the mode shapes at 41 Hz and 44.8 Hz.

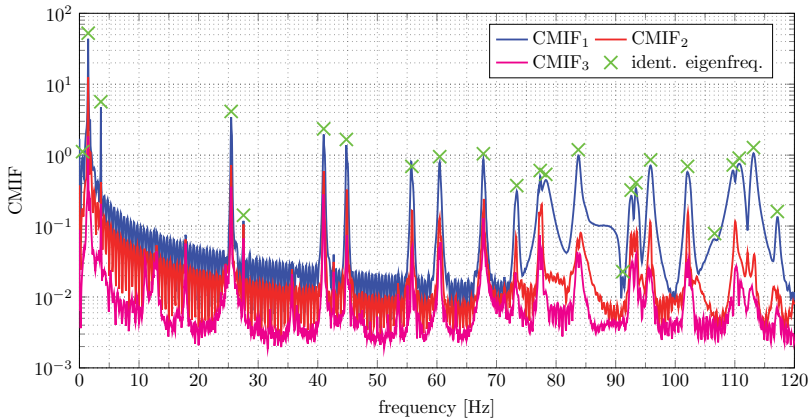


Figure A.13: CMIF of primed dummy painting C with identified eigenfrequency locations.

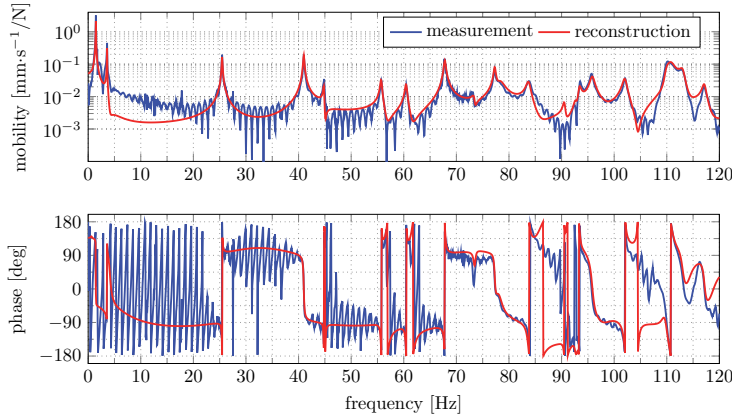


Figure A.14: Amplitude (top) and phase (bottom) of a mobility excited in the bottom center and measured in the middle for primed dummy painting C.

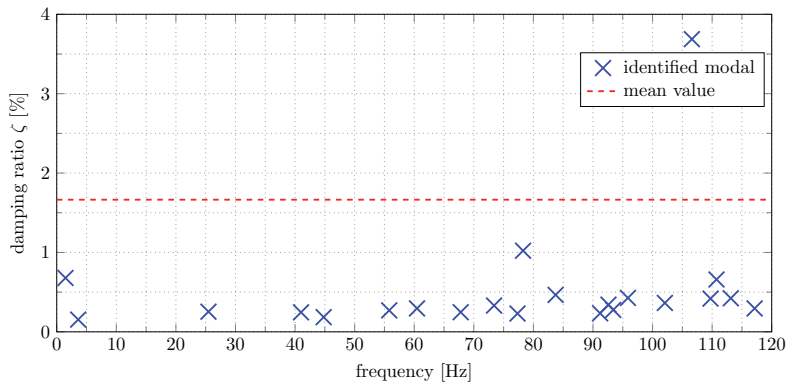


Figure A.15: Identified modal damping ratios for primed dummy painting C and their mean value.

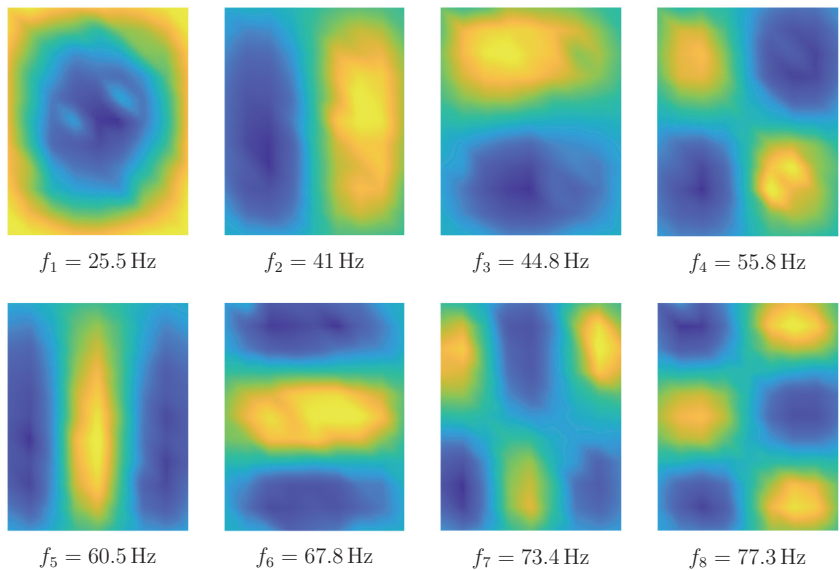


Figure A.16: The first eight identified eigenmodes obtained from the experimental modal analysis for primed dummy painting C.

A.5 Experimental Modal Analysis on Painting Landscape

The CMIF curves of the painting landscape obtained from the experimental modal analysis are shown in Fig. A.17. In the evaluated frequency range up to 100 Hz, 44 eigenfrequencies are identified, which is a denser distribution than that of the painting still life. The first eigenfrequency is located at 7 Hz. Since the experimental modal analysis of the landscape painting is performed during a simulated transport process using different suspensions than the other paintings, no rigid body modes are observed.

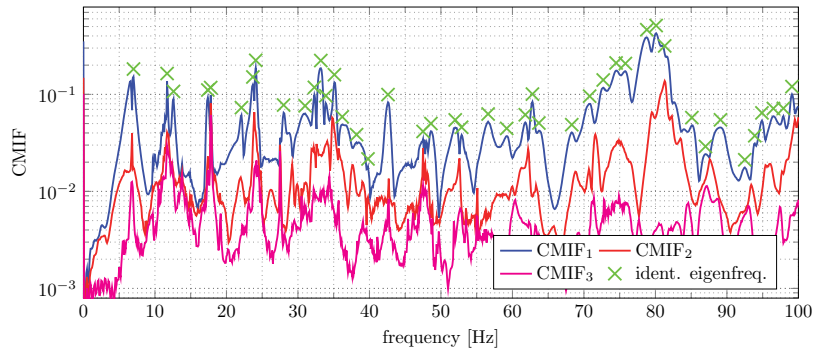


Figure A.17: CMIF of painting landscape with identified eigenfrequency locations.

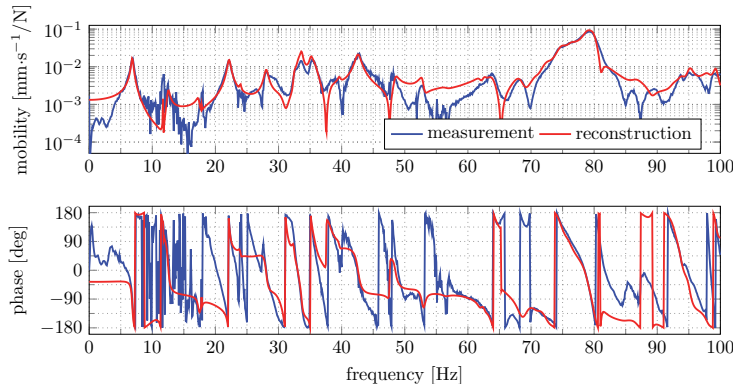


Figure A.18: Amplitude (top) and phase (bottom) of a mobility excited in the bottom center and measured in the middle for painting landscape.

The measured and reconstructed mobilities for one input-output combination shown in Fig. A.18 indicate the quality of parameter identification for painting landscape. Both the high level approximations in the lower frequency range and the large errors in the higher frequency range are apparent. The identified modal damping ratios ζ_r and the first eight mode shapes from the painting landscape are presented in Figs. A.19 and A.20, respectively. The mode shapes are drawn using the same proportionally reduced dimensions of painting landscape, so they are different from other paintings.

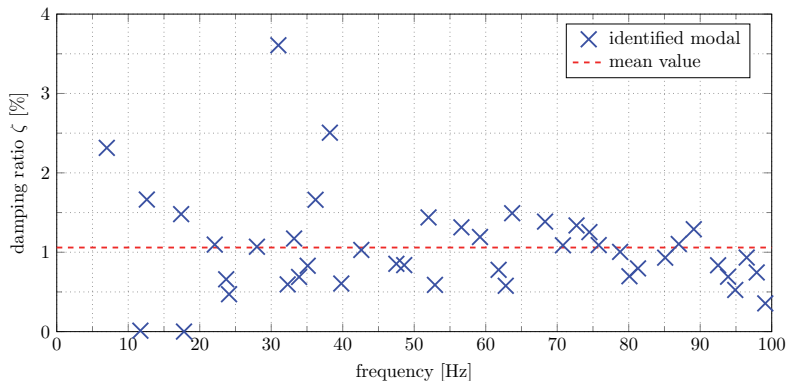


Figure A.19: Identified modal damping ratios for painting landscape and their mean value.

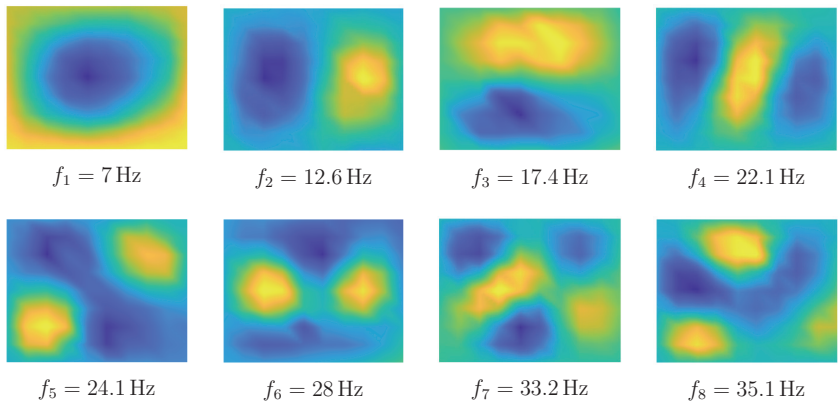


Figure A.20: The first eight identified eigenmodes obtained from the experimental modal analysis for painting landscape.

Abbreviations, Symbols, and Notation

In the following, all important and reoccurring abbreviations and symbols are given to provide an overview of the notation used throughout the thesis. In general, vectors and matrices are printed in bold math font, whereas scalar quantities are displayed in normal math font. Sets are usually written in calligraphic math font. Quantities only appearing within one section are usually only introduced and defined therein.

Abbreviations

| | | | |
|-------|---|-------|--|
| CMIF | complex mode indicator function | ICP | integrated circuit piezoelectric |
| DOF | degree of freedom | LDV | laser Doppler vibrometer |
| EFRF | enhanced frequency response function | LMS | least mean square |
| FE | finite element | MDOF | multi degree of freedom |
| FEM | finite element method | MIMO | multiple-input and multiple-output |
| FIR | finite impulse response | NOFRF | nonlinear output frequency response function |
| FRF | frequency response function | MSE | mean square error |
| FxLMS | filtered- x least mean square | SDOF | single degree of freedom |
| GFRF | generalized frequency response function | SVD | singular value decomposition |

Latin Minuscules

| | | | |
|-----|---|-----|-------------------------------------|
| a | translation acceleration | t | time |
| c | pathway transfer function | u | input samples, left singular vector |
| d | desired signal | v | velocity |
| e | error signal | w | right singular vector |
| f | frequency | x | filter weight coefficients |
| f | vector of external forces, filtered reference signal vector | x | position or displacement |
| r | position vector | x | reference signal |
| | | y | output samples |

Latin Majuscules

| | | | |
|--------------------|---|--------------|--|
| rA | modal constant | M | mass matrix |
| A | Fourier transform of acceleration | O | coordinate origin |
| C | damping matrix | T | sample time, temperature |
| F | Fourier transform of force | U | Fourier transform of input |
| G | nonlinear output frequency response function | U | left singular vectors |
| H | transfer function, relative humidity | V | Fourier transform of velocity |
| H | transfer function matrix | V | right singular vectors |
| K | stiffness matrix | X | Fourier transform of displace- ment |
| L_i, \tilde{L}_i | excitation intensity | \mathbf{X} | reference signal vectors |

Greek Minuscules

| | | | |
|-----------|--------------------------|----------|-------------------------------|
| α | acceleration | ω | angular frequency |
| α | angular acceleration | ζ | modal damping ratio |
| β | mobility | ξ | mean square error |
| λ | eigenvalue | μ | convergence coefficient |
| ϕ | eigenvector or eigenmode | ψ | components of numerical model |
| ρ | density | σ | standard deviation |

Greek Majuscules

| | | | |
|----------|-------------------------------|----------|--------------------|
| Σ | singular value matrix | Θ | accelerance matrix |
| Ξ | sum of the mean square errors | Ψ | numerical model |

Sets

| | | | |
|--------------|---------------------|--------------|------------------------|
| \mathbb{R} | Set of real numbers | \mathbb{C} | Set of complex numbers |
|--------------|---------------------|--------------|------------------------|

Bibliography

- [AkhtarAbeKawamata06] Akhtar, M.T.; Abe, M.; Kawamata, M.: A New Variable Step Size LMS Algorithm-Based Method for Improved Online Secondary Path Modeling in Active Noise Control Systems. *IEEE Transactions on Audio, Speech, and Language Processing*, Vol. 14, No. 2, pp. 720–726, 2006.
- [AllemangBrown98] Allemang, R.J.; Brown, D.L.: A Unified Matrix Polynomial Approach to Modal Identification. *Journal of Sound and Vibration*, Vol. 211, No. 3, pp. 301–322, 1998.
- [AllemangBrown06] Allemang, R.J.; Brown, D.L.: A Complete Review of the Complex Mode Indicator Function (CMIF) With Applications. In *Proceedings of ISMA International Conference on Noise and Vibration Engineering*, Katholieke Universiteit Leuven, Belgium, pp. 3209–3246, 2006.
- [AllemangBrown22] Allemang, R.J.; Brown, D.L.: In Experimental Modal Analysis Methods: *Handbook of Experimental Structural Dynamics*, pp. 533–613. Springer, 2022.
- [ASTMInternational17] ASTM International: Standard Practices for Cycle Counting in Fatigue Analysis. Standard, West Conshohocken, PA, 2017.
- [AubryPostleRenner99] Aubry, E.; Postle, R.; Renner, M.: Vibrating Properties of Textile Surfaces. *Textile Research Journal*, Vol. 69, No. 5, pp. 335–338, 1999.
- [BäschlinEtAl11] Bäschlin, N.; Läuchli, M.; Fankhauser, T.; Palmbach, C.; Hoess, A.: Backing Boards and Glazing on Paintings: Their Damping Capacity in Relation to Shock Impact and Vibration. In *ICOM-CC 16th Triennial Conference*, Lisbon, Criterio, Lisbon, S 1, p. 11, 2011.
- [BäschlinEtAl15] Bäschlin, N.; Läuchli, M.; Palmbach, C.; Hoess, A.; Ryser, M.; Fankhauser, T.; Sautter, K.: Transport fragiler Gemälde—Forschungsergebnisse und Anwendungsbeispiele. Der Teufel steckt im Detail—Zur Praxisanwendung der Forschungsergebnisse Transport fragiler Gemälde. *Zeitschrift für Kunsttechnologie und Konservierung*, Vol. 29, No. 2, pp. 211–222, 2015.

- [BaymaZhuLang18] Bayma, R.S.; Zhu, Y.; Lang, Z.: The Analysis of Nonlinear Systems in the Frequency Domain Using Nonlinear Output Frequency Response Functions. *Automatica*, Vol. 94, pp. 452–457, 2018.
- [Bershad86] Bershad, N.: Analysis of the Normalized LMS Algorithm With Gaussian Inputs. *IEEE Transactions on Acoustics, Speech, and Signal Processing*, Vol. 34, No. 4, pp. 793–806, 1986.
- [Billings13] Billings, S.A.: Nonlinear System Identification: NARMAX Methods in the Time, Frequency, and Spatio-temporal Domains. West Sussex: John Wiley & Sons, 2013.
- [Bjarnason95] Bjarnason, E.: Analysis of the Filtered-x LMS Algorithm. *IEEE Transactions on Speech and Audio Processing*, Vol. 3, No. 6, pp. 504–514, 1995.
- [Braun13] Braun, N.: Transport von Gemälden – Grundlegende Aspekte und Vibrationsmessungen während eines Kunsttransports. Bachelorarbeit, Technische Universität München, 2013.
- [Burgess81] Burgess, J.C.: Active Adaptive Sound Control in a Duct: A Computer Simulation. *The Journal of the Acoustical Society of America*, Vol. 70, No. 3, pp. 715–726, 1981.
- [Caldicott91] Caldicott, P.J.: Vibration and Shock in Transit Situations: A Practical Evaluation Using Random Vibration Techniques. *Art in Transit: Studies in the Transport of Paintings*, pp. SE1–SE8, 1991.
- [CerkanowiczEtAl17] Cerkanowicz, D.; Henry, J.C.; Kaplan, J.T.; Walwik, M.A.: Protecting Art and Increasing Awareness of Transportation Risks. Interactive Qualifying Project for the Degree of Bachelor of Science, Worcester, Massachusetts: Worcester Polytechnic Institute, 2017.
- [ChanZerguineCowan03] Chan, M.K.; Zerguine, A.; Cowan, C.F.N.: An Optimised Normalised LMF Algorithm for Sub-Gaussian Noise. In *IEEE International Conference on Acoustics, Speech, and Signal Processing*, Vol. 6, pp. VI–377, IEEE, 2003.
- [ChiribogaArroyo13] Chiriboga Arroyo, P.G.: Finite Element Modeling of Vibrations in Canvas Paintings. Doctoral thesis, Delft University of Technology, Delft, 2013.
- [DePoloEtAl21] DePolo, G.; Walton, M.; Keune, K.; Shull, K.R.: After the Paint Has Dried: A Review of Testing Techniques for Studying the Mechanical Properties of Artists’ Paint. *Heritage Science*, Vol. 9, No. 1, pp. 1–24, 2021.
- [Diniz97] Diniz, P.S.R.: Adaptive Filtering, Vol. 4. Switzerland: Springer, 1997.

- [DraperSmith98] Draper, N.R.; Smith, H.: Applied Regression Analysis, Vol. 326. New York: John Wiley & Sons, 1998.
- [ElliottNelson85] Elliott, S.J.; Nelson, P.A.: Algorithm for Multichannel LMS Adaptive Filtering. *Electronics Letters*, Vol. 21, No. 21, pp. 979–981, 1985.
- [ElliottStothersNelson87] Elliott, S.; Stothers, I.; Nelson, P.: A Multiple Error LMS Algorithm and Its Application to the Active Control of Sound and Vibration. *IEEE Transactions on Acoustics, Speech, and Signal Processing*, Vol. 35, No. 10, pp. 1423–1434, 1987.
- [Ewins09] Ewins, D.J.: Modal Testing: Theory, Practice and Application. Baldock: Research Studies Press, 2nd Edn., 2009.
- [GaoEtAl22] Gao, Y.; Ziegler, P.; Heinemann, C.; Hartlieb, E.; Eberhard, P.: Experimental Research on the Influence of Modal Nonlinearities of Paintings Under Mechanical Loads. *Archive of Applied Mechanics*, Vol. 92, No. 9, pp. 2679–2694, 2022.
- [GaoEtAl23a] Gao, Y.; Ziegler, P.; Hartlieb, E.; Heinemann, C.; Eberhard, P.: Reproduction of Transport-Induced Vibration of Paintings Based on a Multi-Channel FxLMS Controller. *Acta Mechanica*, Vol. 234, No. 11, pp. 5369–5384, 2023.
- [GaoEtAl23b] Gao, Y.; Ziegler, P.; Heinemann, C.; Hartlieb, E.; Eberhard, P.: Experimental Research on the Vibration Characteristics of Canvas and Primed Canvas of Paintings. *Archive of Mechanical Engineering*, Vol. 70, 2023.
- [GaoZieglerEberhard23] Gao, Y.; Ziegler, P.; Eberhard, P.: Reproduction of Transport-Induced Vibration of Paintings Through Multi-Channel Active Vibration Control. In Carletti, E. (Ed.): *Proceedings of the 29th International Congress on Sound and Vibration*, pp. 1–8, IIAV, Prag, Tschechien: IIAV CZECH s.r.o., 2023.
- [George59] George, D.A.: Continuous Nonlinear Systems. Cambridge: Massachusetts Institute of Technology. Research Laboratory of Electronics, 1959.
- [GiakoumisNikolaidisPitas05] Giakoumis, I.; Nikolaidis, N.; Pitas, I.: Digital Image Processing Techniques for the Detection and Removal of Cracks in Digitized Paintings. *IEEE Transactions on Image Processing*, Vol. 15, No. 1, pp. 178–188, 2005.
- [Gmach10] Gmach, A.: Erschütternde Umstände - Schwingungsbelastung von Kunst- und Bauwerken. Diplomarbeit, Technische Universität München, München, 2010.
- [Green91] Green, T.: Vibration Control: Paintings on Canvas Supports. *Art in Transit: Studies in the Transport of Paintings*, pp. 59–67, 1991.

- [HaganEtAl09] Hagan, E.W.S.; Charalambides, M.N.; Young, C.T.; Learner, T.J.S.; Hackney, S.: Tensile Properties of Latex Paint Films With TiO₂ Pigment. Mechanics of Time-Dependent Materials, Vol. 13, pp. 149–161, 2009.
- [HansenEtAl12] Hansen, C.; Snyder, S.; Qiu, X.; Brooks, L.; Moreau, D.: Active Control of Noise and Vibration. New York: CRC press, 2012.
- [Hartlieb21] Hartlieb, E.: Wie schwingt ein Gewebe? – Einfluss verschiedener Parameter auf die Schwingungseigenschaften von Gemälden auf textilen Trägern. Masterarbeit MSC-336, Staatliche Akademie der bildenden Künste Stuttgart und Institut für Technische und Numerische Mechanik, Universität Stuttgart, 2021.
- [HeinemannEtAl19] Heinemann, C.; Ziegler, P.; Hein, N.; Krekel, C.; Eberhard, P.: Objektiviertes Gemäldetransportmonitoring unter Berücksichtigung mechanischer Einflussfaktoren. Zeitschrift für Kunsttechnologie und Konservierung, Vol. 1, No. 33, pp. 178–198, 2019.
- [HeinKrekel10] Hein, N.; Krekel, C.: 3d-Weißlicht-Streifenprojektionsscanner zur Untersuchung von Transportschäden an Skulpturen. Zeitschrift für Kunsttechnologie und Konservierung; ZKK, Vol. 24, No. 1, pp. p–146, 2010.
- [IbrahimMikulcik77] Ibrahim, S.R.; Mikulcik, E.C.: A Method for the Direct Identification of Vibration Parameters From the Free Response. The Shock and Vibration Inform. Ctr. Shock and Vibration Bull. Part. 4: Sep. 1977, 1977.
- [KambaEtAl08] Kamba, N.; Wada, H.; Tsukada, M.; Takagi, Y.; Imakita, K.: Measurement and Analysis of the Global Transport Environment for Packing Cases for Artifacts. Studies in Conservation, Vol. 53, No. sup1, pp. 60–63, 2008.
- [Kracht11] Kracht, K.: Die Untersuchung des Schwingungsverhaltens von Ölgemälden in Abhängigkeit der Alterung. Doctoral thesis, Technische Universität, Berlin, 2011.
- [KrachtKletschkowski17] Kracht, K.; Kletschkowski, T.: From Art to Engineering: A Technical Review on the Problem of Vibrating Canvas Part I: Excitation and Efforts of Vibration Reduction. Facta Universitatis, Series: Mechanical Engineering, Vol. 15, No. 1, pp. 163–182, 2017.
- [KrekelHein14] Krekel, C.; Hein, N.: Kunsttransport: Gibt es eine Grenze zwischen Schaden und beschleunigter Alterung? In Proceedings of ICOM International Council of Museums, Köln, Vol. 4, pp. 12–17, 2014.
- [KrekelHeinemann20] Krekel, C.; Heinemann, C.: Wenn Kunstwerke auf Reisen gehen: Mikroschäden mithilfe hochauflösender 3D-Modelle finden und dokumentieren. Das Magazin der Deutschen Forschungsgemeinschaft, Vol. 4, pp. 127–128, 2020.

- [Kreyszig09] Kreyszig, E.: Advanced Engineering Mathematics 10th Edition. New York: John Wiley & Sons, 2009.
- [KuoMorgan95] Kuo, S.M.; Morgan, D.R.: Active Noise Control Systems: Algorithms and DSP Implementations. New York: John Wiley&Sons, 1995.
- [Lalanne14] Lalanne, C.: Mechanical Vibration and Shock Analysis, Fatigue Damage, Vol. 4. Hoboken: John Wiley & Sons, 2014.
- [Lamb54] Lamb, L.: Preparation for Painting: The Purpose and Materials of the Artist. London: Oxford University Press, pp. 118–119, 1954.
- [LangBillings96] Lang, Z.Q.; Billings, S.A.: Output Frequency Characteristics of Nonlinear Systems. International Journal of Control, Vol. 64, No. 6, pp. 1049–1067, 1996.
- [LangBillings05] Lang, Z.Q.; Billings, S.A.: Energy Transfer Properties of Non-linear Systems in the Frequency Domain. International Journal of Control, Vol. 78, No. 5, pp. 345–362, 2005.
- [LasykEtAl08] Lasyk, L.; Lukomski, M.; Bratasz, L.; Kozlowsk: Vibration as a Hazard During the Transportation of Canvas Paintings. Studies in Conservation, Vol. 53, No. sup1, pp. 64–68, 2008.
- [LäuchliEtAl14] Läuchli, M.; Bäschlin, N.; Hoess, A.; Fankhauser, T.; Palmbach, C.; Ryser, M.: Packing Systems for Paintings: Damping Capacity in Relation to Transport-Induced Shock and Vibration. In Presentation at ICOM-CC 17th Triennial Conference, Melbourne, Vol. 15, p. 19, 2014.
- [MaiaEtAl97] Maia, N.; Silva, J.; He, J.; Lieven, N.; Lin, R.; Skingle, G.; To, W.; Urgeira, A.: Theoretical and Experimental Modal Analysis. Baldock: Research Studies Presss, 1997.
- [MaoEtAl18] Mao, H.; Tang, W.; Huang, Y.; Yuan, D.; Huang, Z.; Li, X.; Zheng, W.; Ma, S.: The Construction and Comparison of Damage Detection Index Based on the Nonlinear Output Frequency Response Function and Experimental Analysis. Journal of Sound and Vibration, Vol. 427, pp. 82–94, 2018.
- [Marcon91a] Marcon, P.J.: Shock, Vibration, and Protective Package Design. Art in Transit: Studies in the Transport of Paintings, pp. 107–120, 1991.
- [Marcon91b] Marcon, P.J.: Shock, Vibration, and the Shipping Environment. Art in Transit: Studies in the Transport of Paintings, pp. 121–132, 1991.
- [MayLlorens21] May Llorens, M.: Investigation of Inhomogeneity and Geometric Imprecisions of Fabric and Their Influence on the Dynamics of Paintings. Masterarbeit

- MSC-310, Institut für Technische und Numerische Mechanik, Universität Stuttgart, 2021.
- [Mecklenburg82] Mecklenburg, M.F.: Some Aspects of the Mechanical Behavior of Fabric Supported Paintings. The Mechanics of Art Materials and Its Future in Heritage Science, p. 107, 1982.
- [Mecklenburg91] Mecklenburg, M.F.: Art in Transit: Studies in the Transport of Paintings. In International Conference on the Packing and Transportation of Paintings, London: National Gallery of Art, 1991.
- [MecklenburgTumosa91a] Mecklenburg, M.F.; Tumosa, C.S.: An Introduction into the Mechanical Behavior of Paintings under Rapid Loading Conditions. Art in Transit: Studies in the Transport of Paintings, pp. 137–171, 1991.
- [MecklenburgTumosa91b] Mecklenburg, M.F.; Tumosa, C.S.: Mechanical Behavior of Paintings Subjected to Changes in Temperature and Relative Humidity. Art in Transit: Studies in the Transport of Paintings, pp. 173–216, 1991.
- [Michalski91] Michalski, S.: Paintings: Their Response to Temperature, Relative Humidity, Shock, and Vibration. Art in Transit: Studies in the Transport of Paintings, pp. 223–248, 1991.
- [Michalski13] Michalski, S.: Stuffing Everything We Know About Mechanical Properties into one Collection Simulation. Climate for Collections: Standards and Uncertainties, pp. 349–361, 2013.
- [Morgan80] Morgan, D.: An Analysis of Multiple Correlation Cancellation Loops With a Filter in the Auxiliary Path. IEEE Transactions on Acoustics, Speech, and Signal Processing, Vol. 28, No. 4, pp. 454–467, 1980.
- [NayfehMook08] Nayfeh, A.H.; Mook, D.T.: Nonlinear Oscillations. New York: John Wiley & Sons, 2008.
- [Palmbach07] Palmbach, C.: Messung transportbedingter Schwingungen an textilen Bildträgern. Diplomarbeit, Hochschule der Künste Bern, Bern, 2007.
- [PeiTseng94] Pei, S.C.; Tseng, C.C.: Least Mean P-Power Error Criterion for Adaptive FIR Filter. IEEE Journal on Selected Areas in Communications, Vol. 12, No. 9, pp. 1540–1547, 1994.
- [PengEtAl11] Peng, Z.K.; Lang, Z.Q.; Wolters, C.; Billings, S.A.; Worden, K.: Feasibility Study of Structural Damage Detection Using NARMAX Modelling and Nonlinear Output Frequency Response Function Based Analysis. Mechanical Systems and Signal Processing, Vol. 25, No. 3, pp. 1045–1061, 2011.

- [PinnaGaleottiMazzeo09] Pinna, D.; Galeotti, M.; Mazzeo, R.: Scientific Examination for the Investigation of Paintings. A Handbook for Conservator-Restorers. Firenze: Centro Di, 2009.
- [Polytec12] Polytec: Manual for Polytec Scanning Vibrometer PSV-500. Waldbronn, 2012.
- [Saunders98] Saunders, D.: Monitoring Shock and Vibration During the Transportation of Paintings. National Gallery Technical Bulletin, Vol. 19, pp. 64–73, 1998.
- [Saunders05] Saunders, D.: The Effect of Painting Orientation During Air Transportation. In ICOM Committee for Conservation, 14th Triennial Meeting, pp. 700–707, Hague, 2005.
- [Sautter14] Sautter, K.: Der Einfluss von Stossbelastungen auf das Schwingungsverhalten textiler Bildträger: Ein Beitrag zur Risikoabschätzung von Gemäldetransporten. Masterarbeit, Hochschule der Künste Bern, 2014.
- [SnyderHansen90] Snyder, S.D.; Hansen, C.H.: The Influence of Transducer Transfer Functions and Acoustic Time Delays on the Implementation of the LMS Algorithm in Active Noise Control Systems. Journal of Sound and Vibration, Vol. 141, No. 3, pp. 409–424, 1990.
- [SnyderHansen92] Snyder, S.D.; Hansen, C.H.: Design Considerations for Active Noise Control Systems Implementing the Multiple Input, Multiple Output LMS Algorithm. Journal of Sound and Vibration, Vol. 159, No. 1, pp. 157–174, 1992.
- [TornariTsiranidouBernikola14] Tornari, V.; Tsiranidou, E.; Bernikola, E.: Crack-Growth on Canvas Paintings During Transport Simulation Monitored With Digital Holographic Speckle Interferometry. Advances in Research, Vol. 2, No. 12, pp. 967–986, 2014.
- [TsiranidouEtAl11] Tsiranidou, E.; Bernikola, E.; Tornari, V.; Fankhauser, T.; Läuchli, M.; Palmbach, C.; Bäschnlin, N.: Holographic Monitoring of Transportation Effects on Canvas Paintings. SPIE Newsroom, 2011.
- [TsiranidouEtAl13] Tsiranidou, E.; Bernikola, E.; Tornari, V.; Fankhauser, T.; Läuchli, M.; Bäschnlin, N.; Palmbach, C.: Studying Transportation Effects on Canvas Paintings by Full Field Digital Holographic Techniques, 2013.
- [TveitGonenErduran22] Tveit, E.S.; Gonen, S.; Erduran, E.: Mechanical Loads on Munch's Porous Paintings Caused by Handing During In-House Transport. International Journal of Conservation Science, Vol. 13, pp. 1643–1652, 2022.
- [WaentigEtAl15] Waentig, F.; Dropmann, M.; Konold, K.; Spiegel, E.; Wenzel, C.: Leitfaden Präventive Konservierung. Report, ICOM Deutschland eV, 2015.

- [WalachWidrow84] Walach, E.; Widrow, B.: The Least Mean Fourth (LMF) Adaptive Algorithm and Its Family. *IEEE Transactions on Information Theory*, Vol. 30, No. 2, pp. 275–283, 1984.
- [WeiKragtVisser05] Wei, W.; Kragt, W.; Visser, A.: Non-Contact Measurement of Vibrations in Paintings Using Laser Doppler Vibrometry. In 8th International Conference on Non-Destructive Investigations and Microanalysis for the Diagnostics and Conservation of the Cultural and Environmental Heritage, 2005.
- [WidrowEtAl75] Widrow, B.; Glover, J.R.; McCool, J.M.; Kaunitz, J.; Williams, C.S.; Hearn, R.H.; Zeidler, J.R.; Dong, J.R.E.; Goodlin, R.C.: Adaptive Noise Cancelling: Principles and Applications. *Proceedings of the IEEE*, Vol. 63, No. 12, pp. 1692–1716, 1975.
- [YoungAckroyd01] Young, C.; Ackroyd, P.: The Mechanical Behaviour and Environmental Response of Paintings to Three Types of Lining Treatment. *National Gallery Technical Bulletin*, Vol. 22, pp. 85–104, 2001.

